Numerical simulation of suspension transport in bifurcating and wavy channels

M Mallikarjuna Reddy

Numerical simulation of suspension transport in bifurcating and wavy channels

Thesis submitted to the
Indian Institute of Technology Guwahati
for award of the degree

of

Doctor of Philosophy

by

M Mallikarjuna Reddy

Under the guidance of

Prof. Anugrah Singh
&
Dr. Pankaj Tiwari

Department of Chemical Engineering
Indian Institute of Technology Guwahati
Assam - 781039, India
March 2019

CERTIFICATE

This is to certify that the thesis entitled **Numerical simulation of suspension transport in bifurcating and wavy channels**, submitted by **M Mallikarjuna Reddy** (Roll No.136107010) to Indian Institute of Technology Guwahati, in the fulfillment of the requirements for the degree of Doctor of Philosophy in Chemical Engineering is a record of bonafide research work under my supervision. The work embodied in this thesis has not been submitted for any other degree or diploma. In my opinion, the thesis is up to the standard of fulfilling the requirements of the doctoral degree as prescribed by the regulations of this Institute.

Date:

Prof. Anugrah Singh,
Professor
Department of Chemical Engineering,
Indian Institute of Technology Guwahati,
India.

Dr. Pankaj Tiwari,
Associate Professor
Department of Chemical Engineering,
Indian Institute of Technology Guwahati,
India.

DECLARATION

I, M Mallikarjuna Reddy, certify that except where due acknowledgment has been made, this thesis is a presentation of my original research work done under the guidance of my thesis supervisor(s). Wherever contributions of others are involved, every effort is made to indicate this clearly, with due reference to the literature, and acknowledgement of collaborative research and discussions. I hereby confirm that the thesis is free from any plagiarized material and does not infringe any rights of others. I also confirm that if any third party owned material is included in my thesis which required a written permission from the copyright owners, I have obtained all such permissions from respective copyright owners. This work is carried out in the department of Chemical Engineering, Indian Institute of Technology Guwahati, during the period of July 2013 to November 2018.

M Mallikarjuna Reddy

Dedicated to My Beloved Parents

ACKNOWLEDGMENT

It is my great pleasure to thank each and everyone who helped directly or indirectly to complete my research work and made this thesis possible. I owe my deepest gratitude to all of them.

The first and foremost gratitude goes to my supervisors **Prof. Anugrah Singh** and **Dr. Pankaj Tiwari** for their valuable guidance throughout the research work. I thank them for their encouragement, patience towards research and support, which enabled me to develop a better understanding of the subject leading to the present this thesis. I would also like to acknowledge my sincere gratitude to my doctoral committee members, **Prof. Ghosh Pallab**, **Prof. Nanda Kishore** and **Prof. Natesan Srinivasan**, for their advice and suggestions throughout my research work.

My sincere thanks go to the faculty members of Department of Chemical Engineering, IIT Guwahati, for their continuous suggestions and inspirations. I also like to express my thanks to the staff members for making a homely atmosphere.

I am grateful to all my lab members from our group, Dr. Ashish Kumar Thokchom, Dr. S. Yadav, Mr. Bhaskar, Mr. Dharmendra, Mr. Srinivas, Dr. Sudarshan, Mr. Niloy, Mr. Manjunath Reddy, Mr. Delhi Ganesh, Mr. Imran, Mr. Aslam, Mr. Jyothi Krisha, Mr. Shadab, Mr. Ajeeth, Mr. Nasaba, Mr. Vikas, Mr. Rupak, Mr. Najrul, Ms. Salma, and Mr. Vishnu, for their co-operative assistance .

I cannot forget to thank my friends Mr. Narasimha, Mr. G. Bharath, Mr. T. Ramesh, Mr. Prudhviraj, Mr. Satya, Mr. Santosh, Mr. Soma Shekar Goud, Mr. Phani, Mr. Rambhupal, Mr. Hanumanth, Mr. Rajashekhar, Mr. Srinu, Mr. Durga, Mr. Rambabu, Mr. Anudeep, Mr. Ramu, Mr. Pankaj, Mr. Charan, Mr. Mouli, Mr. Gunolla Nagendra Prasad, Mr. Chiranjeevi, Mr. Harish, Mr. Pradeep, Mr. Venu, Mr. Sai Krishna, Mr. Manish, Mr. Mahesh, Mr. Deepak, Mr. Fahad, Mr. Ritesh, and Mr. Soman for the lovely support in making my stay at IIT Guwahati memorable.

After all, I would like to thank all departmental and office staff for helping me in many ways for my research work.

Deep heartedly, I thank my parents and my family members for their encouragement, blessings and motivation at each and every step.

M Mallikarjuna Reddy

Abstract

This thesis deals with the numerical investigation of the shear-induced particle migration of neutrally buoyant suspensions in bifurcating channels and wavy channels via continuum via computational fluid dynamics (CFD) simulations. The CFD simulations based on continuum models such as diffusive flux model (DFM) and suspension balance model (SBM) have an advantage over the computationally intensive particle tracking simulations as they can be generalized for complex geometries. The suspension considered in our simulations was non-colloidal, and non-Brownian rigid particles in a stokes regime ($Re \ll 1$).

Numerical simulations of monodispersed suspension in a 3D oblique bifurcating channel were performed to study the concentration and velocity profiles before and after bifurcation. Both DFM and SBM were considered in the simulations and compared quantitatively. The effect of bifurcation angle on the velocity, particle concentration, and partitioning of bulk flow and particles in the downstream branches has been carried out. The suspension fluid velocity profiles showed a marked difference over pure carrier fluid velocity profiles and greatly depends on the orientation of the geometry (bifurcation angle). After the bifurcation, the velocity and concentration profiles become asymmetric and degree of asymmetry depends on the bifurcation angle. As the bifurcation angle increases, the dividing streamline shifts towards the side branch and suspension shows slightly different behavior over pure carrier fluid. The partitioning of the particles does not follow the fluid partitioning. The findings of DFM and SBM were very similar.

We have studied the effect of carrier fluid rheology on the shear-induced particle migration through 3D asymmetric T-shaped bifurcating channels. The carrier fluid was considered to be non-Newtonian inelastic fluid. Diffusive flux model of shear-induced migration in conjugation with the power-law and Bird-Carreau constitutive model for the carrier fluid was used in the simulations. The velocity and particle concentration profiles in non-Newtonian suspending fluid showed marked differences compared to that in the Newtonian carrier. Enhanced migration was observed in the case of shear-thinning fluid while low for shear thickening. The symmetric velocity and concentration profiles in the inlet branch become asymmetric in the daughter branches and the degree of asymmetry strongly depends on the carrier fluid rheology. The results showed that the particle partitioning between daughter branches do not follow the fluid partitioning and

the degree of separation depends on the relative volumetric flow rate of bulk suspension in the daughter branches. Higher separation efficiency was achieved for suspension in shear-thinning fluid and relatively lower in Newtonian and shear-thickening fluids.

Numerical simulations of bidisperse suspension flowing through symmetric T-shape bifurcating channels in converging as well as diverging flow conditions were performed. The difference in the migration flux of two species leads to size segregation, and this causes alteration of velocity and concentration profiles in the downstream locations of confluence or bifurcation. The velocity and concentration profiles for bidispersed suspension are compared with that of monodispersed case. The effect of particle size ratio and concentration of individual species on the size segregation is investigated. Depending upon the particle size ratio and species concentration, one or both species enriched the channel center. For a suspension comprised of an equal concentration of both species, larger particles always enriched the channel center. On the other hand, the position of concentration peak for smaller particles strongly depends on the size ratio. The segregation behavior in the parent as well as daughter branches of the bifurcating channels were observed to be influenced by the particle size ratios.

The numerical simulations applied to investigate the effects of concentrated suspension flow in a wavy passage shows that the solid particles migrate from regions of high shear-rate to low shear-rate with low velocities and this phenomenon is strongly influenced by particle concentration.

Keywords: Suspension; Shear-induced particle migration; Bifurcation; Diffusive flux model; Suspension balance model; Non-Newtonian fluid; Wavy channel.

Contents

Certificate i

Declaration iii

Dedication v

Acknowledgment vii

Abstract ix

Contents xi

List of Figures xv

List of Tables xxv

List of Symbols and Abbreviations xxvii

1 Introduction and literature review 1

- 1.1 Introduction 1
- 1.2 Shear-induced particle migration 6
  - 1.2.1 Shear-induced particle migration in general geometries 7
  - 1.2.2 Shear-induced particle migration in bifurcating channels 12
- 1.3 Organization of the thesis 15

2 Shear-induced particle migration modeling 17

- 2.1 Monodisperse suspension 17
  - 2.1.1 Overview 17
  - 2.1.2 Constitutive modelling 19
  - 2.1.3 Diffusive flux model 20

2.1.4 Suspension balance model . . . 25
2.2 Bidisperse suspension . . . 28
2.2.1 Overview . . . 28
2.2.2 Model I (Shauly et al., 1997) . . . 29
2.2.3 Model II (Vollebregt et al., 2012) . . . 30
2.2.4 Model III (Kanehl and Stark, 2015) . . . 34
2.2.5 Species conservation equation . . . 36
2.2.6 Suspension viscosity . . . 36

3 Numerical implementation and validation of the models 39
3.1 Overview . . . 39
3.2 Monodisperse suspension . . . 40
3.2.1 Model governing equations . . . 40
3.2.2 Validation of the DFM . . . 42
3.2.3 Validation of the SBM . . . 45
3.3 Bidisperse suspension . . . 46
3.3.1 Validation of the model I (Shauly et al., 1997) . . . 46
3.3.2 Validation of the model II (Vollebregt et al., 2012) . . . 48
3.3.3 Validation of the model III (Kanehl and Stark, 2015) . . . 48

4 Suspension flow through a 3D oblique bifurcating channel 51
4.1 Overview . . . 51
4.2 Problem description . . . 52
4.3 Results and discussion . . . 56
4.3.1 Velocity field . . . 56
4.3.2 Concentration field . . . 65
4.3.3 Flow and particle partitioning . . . 69
4.4 Closure . . . 71

5 Effect of carrier fluid rheology on shear-induced particle migration 73
5.1 Overview . . . 73
5.2 Constitutive modelling . . . 75
5.3 Model validation . . . 76
5.4 Problem description . . . 77
5.5 Results and discussion . . . 79
5.5.1 Velocity field . . . 79
5.5.2 Concentration field . . . 85

5.5.3 Flow and particle partitioning . . . 93
5.6 Closure . . . 101

6 Shear-induced particle migration and size segregation in bidisperse suspension 103
6.1 Overview . . . 103
6.2 Problem description . . . 104
6.3 Results and discussion . . . 105
6.3.1 Flow of bidisperse suspension in a straight channel . . . 105
6.3.2 Flow of bidisperse suspension in a diverging channel . . . 112
6.3.3 Flow of bidisperse suspension in a converging channel . . . 120
6.4 Closure . . . 127

7 Concentrated suspension flow in wavy channels 129
7.1 Problem description . . . 129
7.2 Results and discussion . . . 130
7.2.1 Type-1 wavy channel . . . 130
7.2.2 Type-2 wavy channel . . . 138
7.3 Closure . . . 140

8 Conclusions and prospectives. 141
8.1 Conclusions . . . 141
8.2 Perspectives . . . 144

Appendices 147

A Implementation of general transport equation in OpenFOAM® 149

B Implementation of the SIMPLE algorithm in OpenFOAM® 151

C Schemes used in OpenFOAM® for the different simulation cases 155
C.1 The schemes used in OpenFOAM® in this work for different simulation cases . . . 155
C.2 Solvers settings used in OpenFOAM® in this work for different simulation cases . . . 156
C.3 References . . . 158

D Code implementation procedure inside the transientSimpleFoam 159

E Mesh generation in OpenFOAM® **161**

F The 2D frame-invariant modified suspension balance model **165**

F.1 Frame-invariant suspension kinematics 165

F.1.1 Kinematic ratio 166

F.1.2 Compression-tension coordinates and transition matrix 167

F.1.3 Anisotropic Particle Stress($\sum^{p'}$) in the SBM 167

References **173**

List of Figures

1.1 Classification of suspensions. 2

2.1 Schematic diagrams of the irreversible two-body collisions with (a) constant viscosity and (b) spatially varying viscosity (Phillips et al., 1992). . 22

2.2 Schematic diagrams of the interaction between two particles in a curved geometry. 24

3.1 Imposed boundary conditions. 41

3.2 Comparison of the particle concentration profile obtained from DFM simulations with the experimental data in a channel flow for (a) $\phi = 0.3$, and (b) $\phi = 0.4$. 43

3.3 Comparison of the particle concentration profile obtained from DFM simulations with the experimental data in a pipe flow for (a) $\phi = 0.2$, and (b) $\phi = 0.3$. 44

3.4 Comparison of the particle concentration profile obtained from SBM simulations with the experimental data in a channel flow for (a) $\phi = 0.3$, and (b) $\phi = 0.4$. 45

3.5 Comparison of the particle concentration profile obtained from SBM simulations with the experimental data in a pipe flow for (a) $\phi = 0.2$, and (b) $\phi = 0.3$. 45

3.6 Comparison of simulation results with experimental data of Semwogerere and Weeks (2008) for bidisperse suspension flow in a straight channel by using model I. 47

3.7 Comparison of simulation results with experimental data of Semwogerere and Weeks (2008) for bidisperse suspension flow in a straight channel by using model II. 47

3.8 Comparison of simulation results with experimental data of Semwogerere and Weeks (2008) for bidisperse suspension flow in a straight channel by using model III. 48

4.1 The schematic diagram of the computational geometry and locations where the concentration and the velocity profiles were analyzed. 52
4.2 The comparison of velocity contour planes of Newtonian (a) with that of suspension in the flow direction (x-y plane) for various bifurcation angles by using SBM (b), and DFM (c). 54
4.3 The comparison of flow stream fields of Newtonian (a) with that of suspension in the flow direction ($x-y$ plane) for various bifurcation angles by using SBM (b), and DFM (c). 55
4.4 The cross-sectional contours of velocity magnitude for Newtonian fluid and suspension at various locations in the parent branch (a), main branch (b), and side branch (c). The bifurcation angle θ was 0^0. 57
4.5 The cross-sectional contours of shear-rate for Newtonian fluid and suspension at various locations in the parent branch (a), main branch (b), and side branch (c). The bifurcation angle θ was 0^0. 58
4.6 Comparison of the Newtonian fluid velocity profiles with suspension at different locations in the parent branch along (a) lateral direction, and (b) span-wise direction. 60
4.7 Comparison of the Newtonian fluid velocity profiles with suspension at bifurcation point (location 3) for various bifurcation angles along (a) lateral direction, and (b) span-wise direction. 60
4.8 Comparison of the velocity profiles at various locations in the main branch (a), and side branch (b) along lateral direction. The bifurcation angle θ was 0^0 61
4.9 Comparison of the velocity profiles at various locations in the main branch (a), and side branch (b) along span-wise direction. The bifurcation angle θ was 0^0 61
4.10 Comparison of the velocity profiles at various locations in the main branch (a), and side branch (b) along lateral direction. The bifurcation angle θ was 30^0 62
4.11 Comparison of the velocity profiles at various locations in the main branch (a), and side branch (b) along lateral direction. The bifurcation angle θ was 45^0 62

4.12 The particle concentration contour planes by using SBM and DFM in the flow direction ($x - y$ plane) for various bifurcation angles. The particle concentration was 30%. 63
4.13 The cross-sectional contours of particle concentration at various locations in the parent branch (a), main branch (b), and side branch (c). The bifurcation angle θ was 0^0. 64
4.14 Comparison of the concentration profiles at different locations in the parent branch along lateral (a), and span-wise (b) direction. 66
4.15 Comparison of the concentration profiles at bifurcation point (location 3) for various bifurcation angles along (a) lateral direction, and (b) span-wise direction. 66
4.16 Comparison of the concentration profiles at various locations in the main branch (a), and side branch (b) along lateral direction. The bifurcation angle θ was 0^0. 67
4.17 Comparison of the concentration profiles at various locations in the main branch (a), and side branch (b) along span-wise direction. The bifurcation angle θ was 0^0. 68
4.18 Comparison of the concentration profiles at various locations in the main branch (a), and side branch (b) along lateral direction. The bifurcation angle θ was 30^0. 68
4.19 Comparison of the concentration profiles at various locations in the main branch (a), and side branch (b) along lateral direction. The bifurcation angle θ was 45^0. 69

5.1 Comparison of the particle concentration profile obtained from our numerical simulations with the experimental data in a pipe flow for (a) $n = 1$, and (b) $n = 0.385$. 77
5.2 Schematic diagram of the computational geometry. 78
5.3 Fully-developed cross-sectional velocity contours for carrier fluid and suspension in the straight channel. 80
5.4 Fully-developed cross-sectional shear-rate contours for carrier fluid and suspension in the straight channel. 80
5.5 (a) Comparison of the fully-developed 2D analytical solution (pure fluid) with the 2D numerical solution, (b) Mid-plane velocity profiles for pure fluid and suspension in a 3D straight channel. 81

5.6 The front view ($x - y$ plane) velocity contour planes for (a) pure fluid, and (b) suspension in the bifurcating channel at mid-plane ($z = H$) for three different n values. The depth ratio (H/B) of the daughter branches was 1. 81

5.7 Comparison of mid-plane velocity profiles for the pure fluid and suspension at bifurcation point (location I_1) in the (a) lateral direction, and (b) span-wise direction for various n values ($n = 0.5$, 1, and 1.5). The depth ratio (H/B) of the daughter branches was 1. 82

5.8 Comparison of mid-plane velocity profiles for the pure fluid and suspension along the lateral direction at (a) location M_1, (b) location S_1, (c) location M_2, and (d) location S_2 for various n values. The depth ratio (H/B) of the daughter branches was 1. 82

5.9 Comparison of mid-plane velocity profiles for the pure fluid and suspension along the span-wise direction at (a) location M_1, (b) location S_1, (c) location M_2, and (d) location S_2 for various n values. The depth ratio (H/B) of the daughter branches was 1. 83

5.10 Fully-developed cross-sectional particle concentration contours in the straight channel for (a) $n = 0.5$, (b) $n = 1$, and (c) $n = 1.5$. 86

5.11 Fully-developed mid-plane (along $L - M$) concentration profiles (a), and centerline concentration profiles in the straight channel (b) for various n values. 86

5.12 Development of particle concentration profiles (a), shear-rate and velocity profiles (b) for Newtonian suspension flowing through the straight channel. The corresponding profiles for shear-thinning suspension ($n = 0.5$) are shown in (c) and (d) respectively. 87

5.13 The front view ($x - y$ plane) particle concentration contour planes in the bifurcating channel for (a) $H/B = 1$, (b) $H/B = 1.5$, and (c) $H/B = 2$ at mid-plane ($z = H$) three different n values. 88

5.14 Comparison of mid-plane concentration profiles at location I_1 in the (a) lateral direction, and (b) span-wise direction for various n values ($n = 0.5$, 1, and 1.5). The value of (H/B) was 1. 89

5.15 Comparison of mid-plane concentration profiles along lateral direction at different locations in the main branch (a) and side branch (b) for various carrier fluids. The value of H/B was 1. 89

5.16 Comparison of mid-plane concentration profiles along span-wise direction at different locations in the main branch (a) and side branch (b) for various carrier fluids. The value of H/B was 1. 90

5.17 Comparison of mid-plane concentration profiles along lateral direction at different locations in the main branch (a) and side branch (b) for various carrier fluids. The value of H/B was 1.5. 90

5.18 Comparison of mid-plane concentration profiles along lateral direction at different locations in the main branch (a) and side branch (b) for various carrier fluids. The value of H/B was 2. 91

5.19 Comparison of mid-plane concentration profiles in the lateral direction for power-law and Bird-Carreau model: (a) fully-developed profile in the straight channel (b) profiles in the inlet section of bifurcating channel at the location I_1, (c) profiles at different locations in the main branch, and (d) profiles at different locations in the side branch. The flow rate in the main and side branch was equal ($H/B = 1$), and the flow behavior index (n) was 0.5. 92

5.20 Fully-developed cross-sectional kinematic viscosity contours for (a) carrier fluid, and (b) suspension in the straight channel. 94

5.21 The front view ($x - y$ plane) kinematic viscosity contour planes in the bifurcating channel for (a) $H/B = 1$, (b) $H/B = 1.5$, and (c) $H/B = 2$ at mid-plane ($z = H$) for a range of n values for carrier fluid. 95

5.22 The front view ($x - y$ plane) kinematic viscosity contour planes in the bifurcating channel for (a) $H/B = 1$, (b) $H/B = 1.5$, and (c) $H/B = 2$ at mid-plane ($z = H$) for a range of n values for suspension. The particle concentration was 30%. 96

5.23 The cross-sectional shear-rate contour planes at the entrance of main branch and side branch in the bifurcating channel for (a) $H/B = 1.5$, and (b) $H/B = 2$ for different carrier fluids. The particle concentration was 30%. 98

5.24 The variation of fractionation index with the ratio of the width of the main and daughter branches (H/B) for shear-thinning, shear-thickening and Newtonian carriers. 100

6.1 Geometrical configuration of the two-dimensional bifurcation channels used in the simulations. (a) diverging flow, and (b) converging flow. . . . 104

6.2 (a) Fully-developed concentration profiles and (b) evolution of profiles of monodisperse suspension along the length of the channel in the gradient direction for particle sizes $a = 10$ μm and 30 μm. 106

6.3 Fully-developed concentration contour planes ϕ_i of bidisperse suspension in the straight channel for $a_L/a_S =$ (a) 1.5 and (b) 3. Other parameters were $\overline{\phi}_S = 0.25$ and $\overline{\phi}_L = 0.25$. 107

6.4 Fully-developed concentration profiles ϕ_i of bidisperse suspension in the straight channel for $a_L/a_S =$ (a) 1.5 and (b) 3. Other parameters were $\overline{\phi}_S = 0.25$ and $\overline{\phi}_L = 0.25$. 107

6.5 Evolution of concentration profiles ϕ_i of bidisperse suspension in the straight channel for $a_L/a_S =$ (a) 1.5 and (b) 3. Other parameters were $\overline{\phi}_S = 0.25$ and $\overline{\phi}_L = 0.25$. 108

6.6 Fully-developed concentration profiles ϕ_S of bidisperse suspension for various $\bar{\phi}_L$. The mean concentration of the smaller particles was kept constant ($\bar{\phi}_S = 0.25$). (a) $a_L/a_S = 1.5$, (b) $a_L/a_S = 2$, (c) $a_L/a_S = 2.5$ and (d) $a_L/a_S = 3$. 109

6.7 Fully-developed concentration profiles ϕ_L of bidisperse suspension for various $\bar{\phi}_S$. The mean concentration of smaller particles was kept constant ($\bar{\phi}_L = 0.25$). (a) $a_L/a_S = 1.5$, (b) $a_L/a_S = 2$, (c) $a_L/a_S = 2.5$ and (d) $a_L/a_S = 3$. 110

6.8 Particle concentration contour plane of monodisperse suspension in the diverging bifurcating channel. The average inlet concentration was ($\overline{\phi}$) 0.25 and the particle size (a) was 10 μm. 113

6.9 Comparison of the concentration profiles (a) at location D_0 with and without bifurcation and (b) at various locations in the outlet branch for monodisperse suspension in the converging bifurcating channel. The average inlet concentration was ($\overline{\phi}$) 0.25 and the particle size (a) was 10 μm. 113

6.10 The particle concentration contour planes of (a) smaller particles, (b) larger particles and (c) overall concentration of bidisperse suspension in the diverging bifurcating channel. The particle sizes were $a_S = 20$ μm and $a_L = 30$ μm. 115

6.11 Particle concentration contour planes of (a) smaller particles, (b) larger particles and (c) overall concentration of bidisperse suspension in the diverging bifurcating channel. The particle sizes were $a_S = 10$ μm and a_L $= 30$ μm. 116

6.12 Comparison of the concentration profiles of (a) smaller particles, (b) larger particles and (c) overall concentration of bidisperse suspension at different locations in the diverging bifurcating channel. The particle sizes were a_S = 20 μm and a_L = 30 μm. 117

6.13 Comparison of the concentration profiles of (a) smaller particles, (b) larger particles and (c) overall concentration of bidisperse suspension at different locations in the diverging bifurcating channel. The particle sizes were a_S = 10 μm and a_L = 30 μm. 118

6.14 Particle concentration contour plane of monodisperse suspension in the converging bifurcating channel. The average inlet concentration was ($\bar{\phi}$) 0.25 and the particle size (a) was 10 μm. 120

6.15 Comparison of the concentration profiles (a) at location C_0 with the fully-developed concentration profile in the straight channel and (b) at various locations in the outlet branch for monodisperse suspension in the converging bifurcating channel. The average inlet concentration was ($\bar{\phi}$) 0.25 and the particle size (a) was 10 μm. 121

6.16 The particle concentration contour planes of (a) smaller particles, (b) larger particles and (c) overall concentration of bidisperse suspension in the converging bifurcating channel. The particle sizes were a_S = 20 μm and a_L = 30 μm. 123

6.17 Particle concentration contour planes of (a) smaller particles, (b) larger particles and (c) overall concentration of bidisperse suspension in the converging bifurcating channel. The particle sizes were a_S = 10 μm and a_L = 30 μm. 124

6.18 Comparison of the concentration profiles of (a) smaller particles, (b) larger particles and (c) overall concentration of bidisperse suspension at different locations in the converging bifurcating channel. The particle sizes were a_S = 20 μm and a_L = 30 μm. 125

6.19 Comparison of the concentration profiles of (a) smaller particles, (b) larger particles and (c) overall concentration of bidisperse suspension at different locations in the converging bifurcating channel. The particle sizes were a_S = 10 μm and a_L = 30 μm. 126

7.1 Schematic diagram of the computational geometry of (a) type-1, and (2) type-2 wavy channel. 130

7.2 Schematic representation of the details of a single wavy section and locations at which the velocity and concentration profiles have been measured. (a) Type-1, and (b) type-2 wavy channel. 131
7.3 Velocity contour planes for (a) $\phi_{avg} = 0$, (b) $\phi_{avg} = 0.2$, (c) $\phi_{avg} = 0.3$, (d) $\phi_{avg} = 0.4$, and (e) $\phi_{avg} = 0.5$ in the type-1 wavy channel. 131
7.4 Shear-rate contour planes for (a) $\phi_{avg} = 0$, (b) $\phi_{avg} = 0.2$, (c) $\phi_{avg} = 0.3$, (d) $\phi_{avg} = 0.4$, and (e) $\phi_{avg} = 0.5$ in the type-1 wavy channel. 132
7.5 Comparison of cross-sectional velocity profiles of (a) pure fluid, and (b) suspension ($\phi_{avg} = 0.5$) flow at different locations in the type-1 wavy channel. 132
7.6 Comparison of cross-sectional shear-rate profiles of (a) pure fluid, and (b) suspension ($\phi_{avg} = 0.5$) flow at different locations in the type-1 wavy channel. 133
7.7 Particle concentration contour planes for (a) $\phi_{avg} = 0.2$, (b) $\phi_{avg} = 0.3$, (c) $\phi_{avg} = 0.4$, and (d) $\phi_{avg} = 0.5$ in the type-1 wavy channel. 133
7.8 Particle concentration profiles at different locations in the type-1 wavy channel obtained from DFM and SBM for $\phi_{avg} = 0.2$. At (a) location L_1, (b) location L_2, (c) location L_3, (d) location L_4, and (e) location L_5. . . . 134
7.9 Particle concentration profiles at different locations in the type-1 wavy channel obtained from DFM and SBM for $\phi_{avg} = 0.3$. At (a) location L_1, (b) location L_2, (c) location L_3, (d) location L_4, and (e) location L_5. . . . 134
7.10 Particle concentration profiles at different locations in the type-1 wavy channel obtained from DFM and SBM for $\phi_{avg} = 0.4$. At (a) location L_1, (b) location L_2, (c) location L_3, (d) location L_4, and (e) location L_5. . . . 135
7.11 Particle concentration profiles at different locations in the type-1 wavy channel obtained from DFM and SBM for $\phi_{avg} = 0.5$. At (a) location L_1, (b) location L_2, (c) location L_3, (d) location L_4, and (e) location L_5. . . . 135
7.12 Velocity contour planes for (a) $\phi_{avg} = 0$, (b) $\phi_{avg} = 0.2$, (c) $\phi_{avg} = 0.3$, (d) $\phi_{avg} = 0.4$, and (e) $\phi_{avg} = 0.5$ in the type-2 wavy channel. 137
7.13 Shear-rate contour planes for (a) $\phi_{avg} = 0$, (b) $\phi_{avg} = 0.2$, (c) $\phi_{avg} = 0.3$, (d) $\phi_{avg} = 0.4$, and (e) $\phi_{avg} = 0.5$ in the type-2 wavy channel. 137
7.14 Particle concentration contour planes for (a) $\phi_{avg} = 0.2$, (b) $\phi_{avg} = 0.3$, (c) $\phi_{avg} = 0.4$, and (d) $\phi_{avg} = 0.5$ in the type-2 wavy channel. 138
7.15 Particle concentration profiles at different locations in the type-1 wavy channel obtained from DFM and SBM for $\phi_{avg} = 0.3$. At (a) location L_1, (b) location L_2, (c) location L_3, (d) location L_4, and (e) location L_5. . . . 139

7.16 Particle concentration profiles at different locations in the type-2 wavy channel obtained from DFM and SBM for $\phi_{avg} = 0.5$. At (a) location L_1, (b) location L_2, (c) location L_3, (d) location L_4, and (e) location L_5. . . . 139

E.1 A single block. 162

F.1 Variation of C, B_t, and B_c with the kinematic ratio $\hat{\rho}_k$. 168

List of Tables

1.1 Forces on the particles present in suspension flow. 3

3.1 Geometry details and simulation parameters for the validation of monodispersed models in the rectangular conduit. 43
3.2 Geometry details and simulation parameters for the validation of monodispersed models in the pipe flow. 43
3.3 Geometry details and simulation parameters for the validation of bidispersed models in the channel flow. 46

4.1 Geometry details and simulation parameters. 53
4.2 The Fraction of the pure fluid (without particles), and bulk suspension partitioned between the daughter branches. 70
4.3 The Fraction of the particles partitioned between the daughter branches. . 70

5.1 Geometry details and simulation parameters. 78
5.2 The Fraction of pure fluid (without particles), bulk suspension and particles partitioned between the daughter branches. 94

6.1 Geometry details and simulation parameters. 105

List of Symbols and Abbreviations

List of Symbols

a	Particle radius
b	Batchelor's value
Re_p	Particle Reynolds number
Pe	Péclet number
H	Half-width of the channel
$\boldsymbol{U}$	Suspension mean velocity
a_s	Non-local factor
$\boldsymbol{E}$	Rate of strain tensor
B	Half-depth of the channel
L	Length of the channel
K_c	Diffusion coefficient in concentration
K_η	Diffusion coefficient in viscosity
P	Pressure
$\mathbf{Q}$	Parametric symmetric tensor
$\boldsymbol{N_t}$	Total diffusive flux
$\boldsymbol{N_\eta}$	Flux due to spatially varying viscosity
$\boldsymbol{N_c}$	Flux due to spatially varying interaction frequency

$\boldsymbol{N_b}$	Flux due to Brownian motion
$\boldsymbol{N_r}$	Flux due to curvature of streamlines
$\boldsymbol{N_t^i}$	Flux of species i
k	Boltzmann's constant
C	Crowding parameter
$f(\phi)$	Sedimentation hindrance function
t	Time
T	Absolute temperature

Greek symbol

ϕ	Particle volume fraction
$\eta(\phi)$	Suspension viscosity
η_b	Viscosity of the carrier fluid
ρ	Density of the carrier fluid
ρ_p	Density of the particles
α	Fitting parameter
$\boldsymbol{\Sigma}$	total stress tensor
$\boldsymbol{\Sigma}^f$	fluid phase stress tensor
$\boldsymbol{\Sigma}^p$	particle phase stress tensor
τ	deviatoric stress tensor
$\dot{\gamma}$	local shear-rate
∇	gradient operator
η_N	normal stress viscosity
η_p	particle shear viscosity
ϕ_m	maximum packing fraction

List of Abbreviations

SIPM	Shear-induced particle migration
DFM	Diffusive flux model
SBM	Suspension balance model
MPCD	Multi-particle collision dynamics
OpenFOAM	Open field operation and manipulation
CFD	Computational fluid dynamics
SIMPLE	Semi implicit pressure linked equations
NMR	Nuclear magnetic resonance imaging technique
RBCs	Red blood cells
LDA	Laser-Doppler anemometry

Chapter 1

Introduction and literature review

1.1 Introduction

Suspension refers to the dispersion of solid particles in liquid media. Familiar examples include biological fluids such as milk and blood; industrial daily-life products such as paints, cosmetics, food, alloys, and detergents; natural ones such as muds. Suspension flows are also involved in many industrial applications include: manufacture of paper and fiber composites, oils and tailing transportation, mining and mineral ore transportation, food processing, metal injection molds, powder injection molding (PIM), ceramic and heavy oil production. There are many situations arising in nature which involve the suspension flow such as sediment transport in alluvial flows and saturated soils including oceanic and coastal flows. Nearly every chemical processing industry involves the transport or handling of some type of suspensions. For example pipeline transport is utilized in a variety of ways in the processing of oil sands from the initial transport of oil sands ore to the disposal of the concentrated tailings mixtures and in pharmaceutical industries these suspensions are used to improve the stability of the drug by reducing the fraction of drug in solution and to modify the release date of the drug. Therefore suspension studies are more important and useful to know the properties like velocity, density, viscosity and distribution of the particles etc. In the flow of particulate suspensions, the suspending fluid mediates the interactions between the particles. The hydrodynamic interactions within the suspension strongly depend on the behavior of suspending fluid as well as on the shape and size of the suspended particles. Based on the shape and size of the suspended particles, the suspensions can be classified as follows:

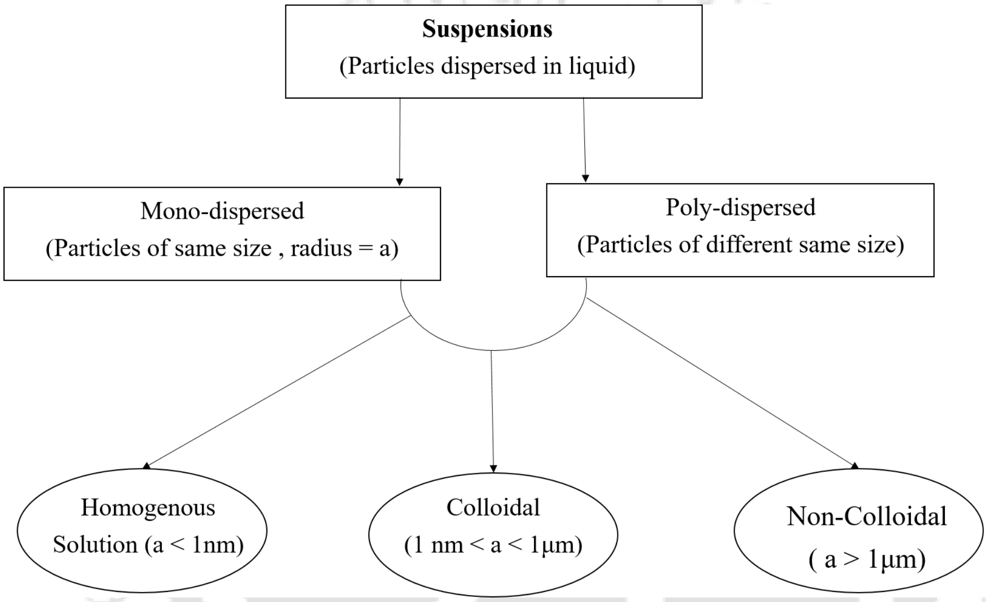

Figure 1.1: Classification of suspensions.

The state of the suspension mainly depends on the distribution of the particle volume fraction (ϕ) which is defined as the percentage of the particles by volume in the liquid:

$$\phi = \frac{4}{3}\pi a^3 n, \tag{1.1}$$

where a is the particle radius, and n is the particle number density. Usually the suspension is said to be dilute if $\phi \leq 0.05$ and concentrated or dense if $\phi \geq 0.05$.

The micro-structure of the particles inside the suspension greatly depends on the physical forces and how they manifest themselves in a given flow field. Forces of different origins exist and act on the particles inside the suspension. These forces can be divided

Table 1.1: Forces on the particles present in suspension flow.

S.N.	Force	Mathematical form	Parameters
1.	Brownian	kT/a	k: Boltzmann's constant T: Absolute Temperature [K]
2.	Electrostatic	$\xi\xi_0\zeta^2$	ξ: dielectric constant of the fluid ξ_0: permittivity of free space [F.m^{-1}] ζ^2: electrostatic potential of the particles [V]
3.	Hydrodynamic Viscous	$\eta a^2\dot{\gamma}$	η: medium viscosity [Pa . s] $\dot{\gamma}$:shear rate [s^{-1}]
4.	Gravitational	$a^3\Delta\rho g$	$\Delta\rho$: particle fluid density differences [kg.m^{-3}] g : gravitational constant [m.s^{-2}]
5.	Inertial	$\rho_f a^4\dot{\gamma}^2$	ρ: fluid density [kg.m^{-3}]

into two categories: hydrodynamic, and non-hydrodynamic forces (Phillips et al., 1992). The hydrodynamic forces present themselves only in an imposed flow field and include inertial and viscous forces between the particles transmitted through the fluid. The non-hydrodynamic forces are present at all times and include Brownian effects, surface effects, electro-viscous effects, Van der Waals interactions between the particles, and external field effects such as gravity or imposed electric and magnetic fields. The relative magnitude of these two kinds of forces will decide the equilibrium position of the particles. The following Table 1.1 provides some insight into the different forces that are acting on the particles inside the suspension. To quantify these characteristics we introduced two non-dimensional numbers: the particle Reynolds number (Re_p) and the Péclet number (Pe).

1. The particle Reynolds number is defined as the ratio between inertial and viscous

forces given by:

$$Re_p = \frac{4}{3}\frac{\rho_p}{\eta_0}\frac{a^3}{H^2}U_{max}, \tag{1.2}$$

where ρ_p is the particle density, η_0 is the suspending fluid viscosity, H is the half width of the channel, and U_{max} is the maximum suspension velocity. At very low Reynolds number ($Re_p \ll 1$), the inertial effects can be neglected.

2. The Péclet number is defined as the ratio between hydrodynamic and Brownian forces given by:

$$Pe = \frac{6\pi\eta_0 a^3\dot{\gamma}}{kT}, \tag{1.3}$$

where $\dot{\gamma}$ is the local shear-rate, k is the Boltzmann constant, and T is the absolute temperature. At very high Péclet number ($Pe \approx \mathrm{O}(10^6)$), the Brownian effects can be neglected.

There has been a significant effort in the literature to characterize the viscosity of different types of suspension, both from the theoretical point of view and from the experimental focusing on dilute, semi-dilute and concentrated systems. Assuming the absence of interactions between the suspended particles in a dilute suspension of spherical particles in a Newtonian fluid, Einstein (1906) predicted the bulk viscosity of the entire suspension. He showed that the effective suspension viscosity linearly increases with the spheres volume fraction and derived the following formula:

$$\eta = \eta_0(1 + 2.5\phi). \tag{1.4}$$

Later, Batchelor and Green (1972) extended the previous work of Einstein (1906) to a higher limit ($\phi \leq 0.15$) providing a new suspension viscosity law such that:

$$\eta = \eta_0(1 + 2.5\phi + b\phi^2), \tag{1.5}$$

where the term in ϕ^2 accounts for hydrodynamic interactions between the particle pairs that arise at higher volume fractions. The values of b depend on the flow type and range varies from 4.375 to 14.1. By taking into account the balance between Brownian diffusion and hydrodynamic interaction Batchelor (1977) has given $b = 6.2$.

Ball and Richmond (1980) started from the assumptions that in a concentrated suspension the effect of all the particles are additive and proposed the following correlation:

$$\eta = \eta_0(1 - C)^{-\frac{5}{2}\phi_m}, \tag{1.6}$$

where C accounts for the so-called "crowding" effect. Ball and Richmond's expression is effectively identical to that of Krieger and Dougherty (1959). Krieger and Dougherty's theory also states that, in the general case, the $\frac{5}{2}$ factor should be replaced by the intrinsic viscosity $[\eta]$. The value of $\frac{5}{2}$ is the intrinsic viscosity for an ideal dilute suspension of spherical particles.

The Krieger-Dougherty correlation is as follows:

$$\eta = \eta_0 \left(1 - \frac{\phi}{\phi_m}\right)^{-[\eta]\phi_m}, \tag{1.7}$$

where ϕ_m denotes the maximum packing fraction. At extremely high concentration the particles in the suspension jam up, giving continuous three-dimensional contact throughout the suspensions, thus making flow impossible, i.e. the viscosity tends to infinity. The particular phase volume at which this happens is called the maximum packing fraction ϕ_m. The value of this parameter depends on various factors that influence the arrangement of the particles. Even for a monodispersed hard spheres suspension, the value of ϕ_m range from approximately 0.5 to 0.75 (Krieger and Dougherty, 1959). Here we mention the other models for the suspension viscosity presented in literature:

Maron and Pierce (1956):

$$\eta = \eta_0 \left(1 - \frac{\phi}{\phi_m}\right)^{-2}, \tag{1.8}$$

Leighton and Acrivos (1986):

$$\eta = \eta_0 \left(1 + \frac{1.5\phi}{1 - \frac{\phi}{\phi_m}}\right)^2, \tag{1.9}$$

Morris and Boulay (1999):

$$\eta = \eta_0 + 2.5\eta_0\phi \left(1 - \frac{\phi}{\phi_m}\right)^{-1} + 0.1\eta_0 \left(\frac{\phi}{\phi_m}\right)^2 \left(1 - \frac{\phi}{\phi_m}\right)^{-2}, \tag{1.10}$$

and Zarraga et al. (2000):

$$\eta = \eta_0 \frac{e^{-2.34\phi}}{\left(1 - \frac{\phi}{\phi_m}\right)^3}. \tag{1.11}$$

Even at very low Reynolds number under flow conditions, these particulate suspensions exhibit many interesting phenomena such as segregation, pattern formation, sedimentation, shear-induced particle migration (de-mixing of the particles into non-homogeneous distribution) etc. Over the past three decades, the phenomenon of *shear-induced particle migration* attracted a great deal of attention in order to explain the phenomenon of de-mixing of the particles in the suspension flows. This phenomenon is of practical importance in many areas, including the design and manufacture of composites and ceramic materials and the safe production of solid rocket fuels. The systematic improvement of production methods in each of these areas will depend greatly upon gaining an understanding of the distribution of the particles in a given flow field.

1.2 Shear-induced particle migration

It is defined as the phenomenon in which the particles in a homogeneous suspension migrate from the regions of higher shear to the regions of lower shear-rate in a non-homogeneous shear flows. Numerous techniques (NMR, PIV, PTV etc.) observed experimentally this phenomenon in different flow geometries. The list of publications is extensive and it is impossible to review all these publications in this chapter. Only a brief survey that covers studies of shear-induced migration in general geometries and in bifurcating channels is presented in the sections 1.2.1 and 1.2.2.

1.2.1 Shear-induced particle migration in general geometries

As mentioned in the previous sections, many researchers have conducted investigations on viscosity of the suspension. Much of the experimental and analytical work has been performed in Couette devices in order to determine the self-diffusion and the corresponding diffusion coefficients which can be used to model the suspension flow. As mentioned before, Einstein (1906) gave the formula for effective viscosity in very dilute suspension and his formula was considered as the foundation of many studies later on. For long time it was a commonly accepted view that suspensions should behave as Newtonian fluids for all values of the particle concentration up to the maximum packing fraction. Many years after the work of Einstein, Batchelor and Green (1972) derived the rigorous extension of Einstein's formula to order of ϕ^2 for suspensions of mono-disperse solid spheres. Eckstein et al. (1977) developed a scaling argument for the diffusion coefficient by reducing the dimensionless arguments governing particle-particle interactions. They determined that self-diffusion coefficient was proportional to square of the particle radius and the local shear-rate. The coefficient was found to be nearly linear with concentration up to 20%, and constant beyond that. While measuring the viscosity of concentrated suspensions of neutrally buoyant spheres in Newtonian fluids using the Couette viscometer, Gadala-Maria and Acrivos (1980) observed that the effective viscosity of concentrated suspension decreased slowly with prolonged shear until it reached equilibrium value. They could not find a reasonable explanation for this phenomenon. Leighton and Acrivos (1987a,b) repeated the experiments done by Gadala-Maria and Acrivos (1980), and suggested that the apparent decrease in viscosity results from the migration of particles out of the sample being sheared in the gap between the bob and the cup of the Couette device and into the reservoir containing the stagnant part of the suspension. They proposed a mechanism which explained the existence of particle migration in the direction normal to the shearing direction and also predicted the rate of migration. They proposed that the mechanism of particle migration is basically particle diffusion in response to gradients in shear-rate and in particle concentration acting through irreversible interactions between particles. As explained earlier the gradients in shear-rate and concentration directly affect the frequency and dynamics of collisions between particles. Many studies investigated shear-induced particle migration using experimental and theoretical analysis after the work of Leighton and Acrivos (1987a,b). There have been several experimental evidences to support the phenomenon of shear-induced particle migration exhibited by concentrated suspensions. All of these experiments were performed in simple flow geometries on model suspensions of non-colloidal, monodisperse spheres suspended in viscous Newtonian liquids. The shearing flow geometries discussed below include pressure- driven flow in a circular pipe, pressure-driven flow in a rectangular channel, narrow-gap annular Couette flow, and wide-gap annular Couette flow.

The first quantitative experiments involving pressure-driven flow of concentrated suspensions through tubes at low Reynolds number were performed by Karnis et al. (1966) using hand-analysed cinematography. The velocity profiles suggest that particles had drifted into a non-uniform configuration in response to inhomogeneous shear-rate or velocity gradient in the flow. Specifically particles moved away from the tube wall where local shear rate was high to regions near the tube center where the local shear-rate was low. However, in their experiments, they did not observe any particle migration. They suspected that this blunted velocity profiles are due to wall effects. Later, Leighton and Acrivos (1987b) provided the evidence supporting the idea of particle migration and mechanism for shear-induced migration. Ultra sound-Doppler anemometry was used by Kowalewski (1980) to measure the velocity profile for concentrated suspensions in tube flows. It was found that the blunting of velocity profiles depends upon the particle concentration and particle size. Although the ultrasonic experimental method is very useful, it cannot distinguish between particle and fluid velocities. The measured velocity profile is presumably a mass or volume averaged value. Clearly no particle concentration data is possible via this technique. To give good information about particle concentration profiles, Sinton and Chow (1991) used Nuclear magnetic resonance (NMR) imaging to study the solid-fluid suspension flow in the tube, since it could distinguish between the fluid and solid phases, even in optically opaque suspensions. NMR also provides simultaneous velocity profiles. They found that the velocity profile of suspension was different from the parabolic velocity distribution. The velocity distribution appeared to be blunted with slower than expected velocities towards the center of the pipe for the 42% and 50% volume fraction suspension, while the velocity distribution of suspension of 22% volume fraction exhibited excellent agreement with the parabolic shape. This blunted velocity profile was consistent with the prediction of Leighton and Acrivos (1987b). Like Karnis et al. (1966), Sinton and Chow (1991) also did not find any measurable non-uniformity in particle concentration. Altobelli et al. (1991) measured velocity and concentration profiles of suspensions of spheres flowing in a horizontal pipe using magnetic resonance imaging. They observed that velocity profiles of the suspension ($\phi = 0.39$) were blunted and shifted slightly upward. With change in concentration or velocity, both the fluid velocity and concentration profiles become more axisymmetric. Later, Hampton et al. (1997), measured the velocity and concentration profiles of particles for pressure-driven flow in circular pipes by NMR imaging. In their experiments they observed the non-uniform concentration profiles and simultaneous blunted velocity profiles, for bulk particle volume fractions ranging from 0.1 to 0.50 and also compared with existing shear-induced migration models.

While most of experimental studies on shear-induced migration used the NMR imaging technique, Koh et al. (1994) used laser Doppler anemometry (LDA) to study the pressure-driven flow in a rectangular channel. To avoid the problem of optical turbidity, the refractive indexes of the solid and liquid phases were closely matched. This method was chosen such that by counting the number of Doppler signals in a period of time, the local volume fraction was also measured. These measurements showed the existence of blunted velocity profiles that were independent of suspension flow rate but bluntness increases with increase in particle concentration. The maximum particle concentration was observed near the center. Averbakh et al. (1997) also employed Laser-Doppler anemometry to measure velocity profiles in a rectangular duct to detect velocity fluctuations in the viscous flow of the concentrated suspension induced by the particle presence. Lyon and Leal (1998a) used modified laser-Doppler velocimetry (LDV) method to measure fully-developed particle velocity and concentration profiles, as well as the mean square amplitudes of velocity fluctuations, for concentrated suspension flowing through rectangular channel and confirmed that velocity profiles are blunted; the bluntness increases with increase in particle concentration. They have performed experiments with suspensions up to particle concentrations of 50% and also compared the profiles with the predictions of diffusive flux and suspension balance models.

Shear-induced migration is also studied extensively in curvilinear and eccentric flows. Abbott et al. (1991) used NMR imaging to observe the evolution of radial concentration and velocity profiles of initially well mixed concentrated suspensions of spheres in viscous Newtonian liquids undergoing flow between rotating concentric cylinders (wide gap, annular Couette flow). In Couette flow, particles migrate from the high shear-rate region near the inner rotating cylinder to the low shear-rate region at the outer wall. They also reported that the particle fraction near the outer cylinder at steady state reached a value near 0.6, close to 0.63, the maximum random packing fraction for mono-disperse spheres.

Abbott et al. (1991) also measured the suspension velocity profile and found that the flow in the densely packed region near the outer, stationary cylinder is almost stagnant. Near the center, the particle concentration decreased by at least 30%. Chow et al.

(1994b) performed NMR experiments to measure the evolution of suspension concentration profiles in Couette and parallel-plate geometries. In their study, neutrally buoyant suspensions of nearly mono-disperse, non-Brownian spherical particles at a volume fraction of 0.5 in a Newtonian fluid were used. For Couette flow, the experimental results were in good agreement with Leighton and Acrivos (1987a). However, they found that there was no significant migration of particles across the entire domain of the parallel-plate geometries but some decrease in the apparent viscosity was observed. Chapman (1990) conducted experiments on suspension flow in cone-plate geometry where an outward migration of particles was observed. Chow et al. (1994b) observed that the particles were found to migrate radially outward, away from the apex of the cone in the cone-and-plate geometry. Phan-Thien (1995) observed the particle migration in a concentrated suspension undergoing flow between rotating eccentric cylinders by conducting experiments and numerical simulations. They used the NMR imaging technique to measure the time evolution of concentration and velocity. They also compared the numerical results with the experimental data and found that there was acceptable agreement. Subia et al. (1998) used NMR technique to determine the particle concentration profiles of initially well-mixed suspensions as they separate when subjected to slow flow between counter-rotating eccentric cylinders and in piston-driven flow in a pipe. They have observed good qualitative and quantitative agreement of the numerical predictions with the experimental measurements.

Most of the above mentioned studies have focused extensively on unidirectional and steady flow in simple one and two dimensional geometries such as cylindrical Couette cell parallel-plate geometry, cone-and-plate geometry, rectangular channels and the circular pipes. While flow in complex geometries such as bifurcations are not adequately addressed despite the fact that most of the industrial process involves flows of suspension through 3D geometries. Flow of particles through constrictions and diversion are also of fundamental importance (Chen, 2013). In the next section we describe the migration in bifurcation channels and previous works done so far in the literature.

1.2.2 Shear-induced particle migration in bifurcating channels

Transport of suspension through the bifurcation channels (where a channel or pipe divides into multiple branches) is often encountered in biological systems such as the laminar flow of blood through branched arteries and veins, micro-vascular physiology (Pries et al., 1989). These bifurcation channels are also used in micro-devices for particle separation or mixing (Roberts and Olbricht, 2006). The shear-induced migration phenomenon through the bifurcating channels could be important in many of the above applications. For example, in the biomedical application, the design of artificial valves would require a proper understanding of the distribution of the particles in the bifurcation channels. (Aarts et al., 1988) proposed a method known as "plasma skimming" which is used to separate red blood cells from whole blood by flowing blood through a network of well-designed bifurcations. Balogh and Bagchi (2018) and Yen and Fung (1978) have studied plasma skimming with flexible disks. The plasma skimming technique can be used as an alternative where the conventional techniques are ineffective (Faivre et al., 2006; Jaggi et al., 2007; Leonard et al., 2004). Pries et al. (1989), Krogh (1921), and Enden and Popel (1994) observed that the distribution of red blood cells into branches of bifurcation (Y and T-shaped bifurcation) differs from the distribution of the bulk flow.

Many studies have shown the shear-thinning behavior of blood in Y-shaped bifurcation channels numerically and experimentally for low Reynolds number flows. Balan and Balan (2010) and Kanaris et al. (2012) suggested that the non-Newtonian fluid shows a flattened axial velocity profile due to its shear-thinning behavior. In addition, the red blood cell motions in various bifurcation geometries (like Yand T-shaped channels) has been the area of research in the recent past with a variety of particles, including rigid spheres (Lagoela et al., 2009) and flexible cells (Barber et al., 2008). They observed that

RBCs significantly deviated from streamlines at bifurcation because of cell migration and obstruction effects. Wang and Xing (2010) studied the motion of erythrocyte (Red blood cell) suspensions numerically through axisymmetric, pressure driven channels. They observed that the profile of the capillary flow was markedly blunted in comparison to the parabolic profiles of pure plasma flow. Li et al. (2012) investigated the motion of red blood cells (RBCs) in a Y shaped bifurcating micro-fluidic channels using dissipative particle dynamics of healthy and unhealthy blood at low Reynolds number and their results predicted that RBC flux in bifurcation channel depends on the deformability of RBCs and the feed hematocrit level of blood. Ishikawa et al. (2011) have investigated experimentally the behavior of RBC cells and adhesion of cancer cells in symmetric bifurcations and confluences at low Reynolds number. They revealed that there is a strong asymmetry in the trajectories of RBC cells and cancer cells at the bifurcation and confluences, although the trajectories of tracer particles in pure water were almost symmetric. Subsequent to this Leble et al. (2011) had investigated experimentally the red blood cell motions in a micro-channel with a diverging and converging bifurcation. They observed asymmetry in velocity profiles of RBCs. Fridjonsson et al. (2011) studied the dynamics and flow partitioning of colloidal particles in the Y-shaped bifurcation channel formed with circular segments experimentally and numerically. They observed that the Newtonian fluids exhibited parabolic profile whereas, the Power-law fluids exhibited blunted profiles. Gijsen et al. (1999) investigated the influence of non-Newtonian properties of blood on the velocity distribution in carotid bifurcation experimentally and numerically. They found that the axial velocity profile of the non-Newtonian fluid was blunted. The non-Newtonian fluid had low velocity gradients at the divider wall and high velocity gradients at the non-divider wall. Anastasiou et al. (2012) studied the Newtonian and non-Newtonian properties of pulsatile blood flow in micro-channels using micro particle image velocimetry (μPIV). They measured velocity distribution and wall shear-stress during the flow of blood. In a recent review article, Kumar and Graham (2012) have discussed the margination of leukocytes, RBCs, and platelets and presented a modified shear-induced migration model for the segregation behavior in binary suspension of rigid and deformable particles. Audet and Olbricht (1987) observed that in small vessels, circular particles having the diameters comparable to the vessel diameter could experience significant drift across background fluid streamlines. Ditchfield and Olbricht (1996) performed flow experiments (at low Reynolds number) with the suspension of spherical particles through symmetric Y-shaped and asymmetric T-shaped bifurcations. They have observed that the hydrodynamic interactions between the particles have a strong influence on the flux of the particles through the bifurcation. For a small value of the particle volume fraction, these interactions could be very important. Roberts and Olbricht (2003) analyzed the motion of freely suspended particles in low Reynolds number flows. Their study was mainly focused on Y-shape, T-shape and oblique bifurcation channels formed by circular tubes for a range of particle volume fractions up to 0.06. The inference from the results was that there was a difference in the partitioning of the particles between the bifurcation and those of the suspending fluid. From the above inference, they suggested a method to design a practical micro-fluidic device which has multiple bifurcations to separate particles. Roberts and Olbricht (2006) considered Y-shaped and oblique bifurcations with branches of square or rectangular cross-section for their experimental study. Their observations were similar to that of Roberts and Olbricht (2003) but found that the magnitude of difference depends on the aspect ratio of the cross-section of the channel and also on the bifurcation geometry. They reported a greater volumetric flow rate for the particles entering the downstream branch. Schmid-Schcönbein et al. (1980), Perkkiö (1983), and Barber et al. (2008) have proposed mathematical models to understand the flow and particle partitioning and computed the cell distribution at bifurcations. Most of these studies dealt with dilute concentrations and situations where the size of the particles was almost comparable with the channel width. The flow physics of concentrated suspensions of small particles relative to channel width is less studied numerically and experimentally despite their wide application. Xi and Shapley (2008) have performed NMR experiments on the flow of concentrated suspensions through asymmetric T-junction bifurcation channel of rectangular cross-section. They observed that the particles are almost equally partitioned in downstream branches even though the flow partitioning is unequal. Later, Ahmed and Singh (2011) performed numerical simulations based on the diffusive flux model and obtained good agreement with the experimental work of Xi and Shapley (2008). Recently, Reddy and Singh (2014) have carried out numerical simulations of suspension flow through two-dimensional oblique bifurcating channels and reported that flow partitioning and particle partitioning do not seem to be the same because of redistribution of particles in the daughter branches. In a significant work, Zrehen and Ramachandran (2013) observed the existence of secondary currents in pressure driven flow at Reynolds number flow of the concentrated suspension of non-colloidal particles through a conduit of a square cross-section. The secondary currents in the 3D channel with non-axisymmetric cross-section may influence the particle distribution. The above mentioned studies have motivated us to perform detailed studies on the distribution of particles and its relation to the velocity profile considering utilization of this knowledge in several industrial and biological processes where particle migration is an important issue. In this work, we have studied the flow physics of the concentrated mono and bidispersed suspensions via computational fluid dynamics (CFD) simulations. The CFD simulations based on continuum models such as diffusive flux and suspension balance has an advantage over the computationally intensive particle tracking simulations as they can be generalized for complex geometries.

1.3 Organization of the thesis

The thesis consists of eight chapters. The introduction and motivation for the work, including the literature review is presented in chapter 1. In chapter 2, we describe continuum models which describe the shear-induced migration for monodispersed and bidispersed suspension. Chapter 3 describes the numerical implementation of the models in OpenFOAM® and their validation with the available experimental data. In chapter 4, the flow physics of monodispersed suspension through a 3D oblique bifurcating channel is presented. Chapter 5 deals with the effect of carrier fluid rheology on the shear-induced particle migration in a 3D asymmetric T-shaped bifurcating channel. In chapter 6, the flow physics of the bidispersed suspension through a 2D symmetric T-shaped bifurcating channel. Chapter 7 deals with the flow of concentrated suspension flow in wavy channels. Ultimately, in chapter 8 conclusions of the present work and future perspectives are discussed.

Chapter 2

Shear-induced particle migration modeling

2.1 Monodisperse suspension

2.1.1 Overview

Subsequent to the experimental observations on the shear-induced particle migration there have been significant theoretical approaches to describe the de-mixing mechanism of the suspension. Direct numerical simulations such as Brownian dynamics simulation (Fan et al., 2000) and Stokesian dynamic simulation (Brady and Bossis, 1988; Brady and Morris, 1997; Sierou and Brady, 2002) have been successfully explained the different phenomena exhibited by the suspension in many challenging problems. However, high computational demand restricts the particle number of the $O(10^3)$. On the other hand, the macroscopic approaches have been popular since they are relatively simple and demand less computational resources. Basically, there exist two continuum models which successfully explains the flow physics of the shear-induced particle migration in concentrated suspensions. The first model, named as "diffusive flux model (DFM)", explains the migration resulting from hydrodynamic diffusion of particles in the inhomogeneous shear flows. The diffusive flux model originally proposed by Phillips et al. (1992) based on the scaling arguments of Leighton and Acrivos (1987a,b). This model has been successful in explaining the flow behavior in simple geometries such as channel and pipe flows but failed to match with experimental findings of torsional flows such as cone-and-plate and parallel-plate geometries (Chow et al., 1994b; Subia et al., 1998). Later, the diffusive flux model has been modified to bridge the gap between experiments and predictions (Fang et al., 2002; Krishnan et al., 1996). The original diffusive flux model when employed to predict the particle concentration in torsional parallel-plate and truncated cone-and-plate flows predict inward migration and no migration of particles respectively when the empirical parameters that are adopted by fitting with experimental results of Couette geometry. However, the experimental findings predict that there is no significant radial migration of particles in parallel-plate (Chapman, 1990; Chow et al., 1994b), whereas radially outward migration in truncated cone-and-plate geometry (Chow et al., 1994a). To rectify this drawback Krishnan et al. (1996) added one more additional flux that induced by the curvature of the shear flow or local radius of the streamline. Later, Fang et al. (2002) developed a flow-aligned tensor model and this led to the effective use of the model for the random geometries. The second model, named as “suspension balance model (SBM)”, was proposed by Nott and Brady (1994). This model is based on the conservation of mass and momentum for the suspension phase as well as the particle phase. The particle velocity fluctuations are introduced with a non-local description of suspension temperature. Morris and Boulay (1999) illustrated the importance of anisotropy and normal stress difference effects in suspension balance model for predictions of migration in curvilinear flows. Fang and Phan-Thien (1999) proposed a modification in the suspension balance model that can fit in convection-diffusion equation for unstructured finite volume implementation. Miller and Morris (2006) proposed a non-local shear-stress term in the suspension balance model which depends on the particle radius, characteristic length of geometry and maximum velocity in a pressure driven flow. They also introduced the concept of the non-local shear-rate which is added to the local shear-rate to get rid of the unphysical cusp in concentration profile at the center of the channel. The suspension balance model was extended by Dbouk et al. (2013) to two-dimensional flows through the frame-invariant formulations to account for local kinematics of the suspension including buoyancy effects and applied to the resuspension and mixing of monodispersed suspension in a horizontal Couette cell.

2.1.2 Constitutive modelling

In the continuum models, the suspension considered as a continuum medium and its behavior is governed by the continuity and the momentum equations, respectively as:

$$\frac{\partial \rho}{\partial t} + \nabla.(\rho \boldsymbol{U}) = 0, \tag{2.1}$$

$$\frac{\partial (\rho \boldsymbol{U})}{\partial t} + \nabla.(\rho \boldsymbol{U}\,\boldsymbol{U}) = \nabla.\boldsymbol{\Sigma} + \rho \boldsymbol{g}. \tag{2.2}$$

For neutrally buoyant incompressible monodispersed suspensions of hard spheres in a stokes regime ($Re \ll 1$), the above continuity and momentum equations transformed to:

$$\nabla.\boldsymbol{U} = 0, \tag{2.3}$$

and

$$\nabla.\boldsymbol{\Sigma} = 0, \tag{2.4}$$

respectively, where $\boldsymbol{U}$ is the suspension mean velocity, and $\boldsymbol{\Sigma}$ is the total stress tensor.

Moreover, the continuum models solve additional equation known as particles conservation equation and can be written as:

$$\frac{\partial \phi}{\partial t} + \boldsymbol{U}.\nabla\phi = -\nabla.\boldsymbol{N_t}, \tag{2.5}$$

where ϕ is the particle volume fraction and $\boldsymbol{N_t}$ is the particle migration flux that accounts for different migration mechanisms such as sedimentation, Brownian motion, shear-induced, curvature-induced, or viscosity gradient-induced migrations. Eq. 2.5 is solved in parallel with Eqs. 2.3 and 2.4 to track the evolution of particle concentration ϕ and of the flow field. In the next section we describe briefly the different models that express $\boldsymbol{N_t}$ as the migration flux. The detailed study of these models can be found in the papers of Phillips et al. (1992), Krishnan et al. (1996), Kim et al. (2008), Nott and Brady (1994), and Morris and Boulay (1999).

2.1.3 Diffusive flux model

In this model, the constitutive description for the suspension is divided into two parts. First, an expression for the stress tensor is written for the suspension and modelled as a generalized Newtonian fluid with the viscosity that depends on the local volume fraction of the solids. Second, the distribution of solids is obtained from the solution of the diffusion equation that describes the motion of the particles in a flow field.

2.1.3.1 Stress tensor

The total stress tensor $\boldsymbol{\Sigma}$ in the Eq. 2.3 can be written as:

$$\boldsymbol{\Sigma} = -P\boldsymbol{I} + \boldsymbol{\tau}, \tag{2.6}$$

where P is the pressure and $\boldsymbol{\tau}$ is the deviatoric stress tensor. For the suspension, the deviatoric stress tensor $\boldsymbol{\tau}$ can be written as:

$$\boldsymbol{\tau} = 2\eta(\phi)\boldsymbol{E}, \tag{2.7}$$

where $\boldsymbol{E}$ is the bulk rate of strain tensor and expressed as:

$$\boldsymbol{E} = \frac{1}{2}\left(\nabla\boldsymbol{U} + \nabla\boldsymbol{U}^t\right). \tag{2.8}$$

The suspension viscosity $\eta(\phi)$ in Eq. 2.7 is calculated based on the Kriegers' correlation (Eq. 1.7).

2.1.3.2 Original diffusive flux model (Phillips et al., 1992)

The DFM of Phillips et al. (1992) is based on the scaling arguments of Leighton and Acrivos (1987a,b) for particle migration flux ($\boldsymbol{N_t}$) resulting from spatially varying viscosity ($\boldsymbol{N_\eta}$), interaction frequency ($\boldsymbol{N_c}$), and Brownian diffusion ($\boldsymbol{N_b}$).

Effect of spatially varying interaction frequency

Fig. 2.1 shows a schematic diagram of irreversible two-body collisions. Fig. 2.1(a) shows that a collision (close interaction) can occur when two particles in adjacent shearing surfaces move past one another. Such collision can cause a particle to be irreversibly moved from its original streamline. A particle experiences a higher frequency of collisions from one direction than from opposing direction and will migrate normal to the shearing surface in the direction of lower collision frequency. When there is a velocity gradient in shear flow, irreversible two body collisions can occur due to spatially varying frequency of interactions. The number of collisions experienced by a test particle will scale as $\dot{\gamma}\phi$, where, $\dot{\gamma} := \sqrt{2\boldsymbol{E}:\boldsymbol{E}}$ is the local shear-rate. The variation in the collision frequency over a distance of $\mathrm{O}(a)$ is then given by $a\nabla(\dot{\gamma}\phi)$. Leighton and Acrivos (1987a,b) assumed that the particle migration velocity is linearly proportional to the variation in the collision frequency and that each of these two-body interactions gives rise to a displacement of O(a) leads to an expression for the flux ($\boldsymbol{N_c}$) given as:

$$\boldsymbol{N_c} = -K_c a^2 \phi \nabla(\dot{\gamma}\phi) = a^2 \left(\phi^2 \nabla\dot{\gamma} + \phi\dot{\gamma}\nabla\phi\right), \tag{2.9}$$

where K_c is a proportionality constant of order unity that can be determined from the experimental data.

The first term on the right side of Eq. 2.9 implies that even if there is no gradient in the particle volume fraction, migration will result if the particles on one side of a test particle are moving past it more rapidly than on the other side. Because this variation gives a higher number of inter-particle interactions on the side with a higher $\dot{\gamma}$. Therefore, a high shear-rate or high concentration of particles results in a larger frequency of collisions. The second term on the right side of Eq. 2.9 states that a gradient in particle volume fraction will cause a spatial variation in the frequency of interactions. The flux due to the variation in shear-rate and that due to a concentration gradient generally oppose one another.

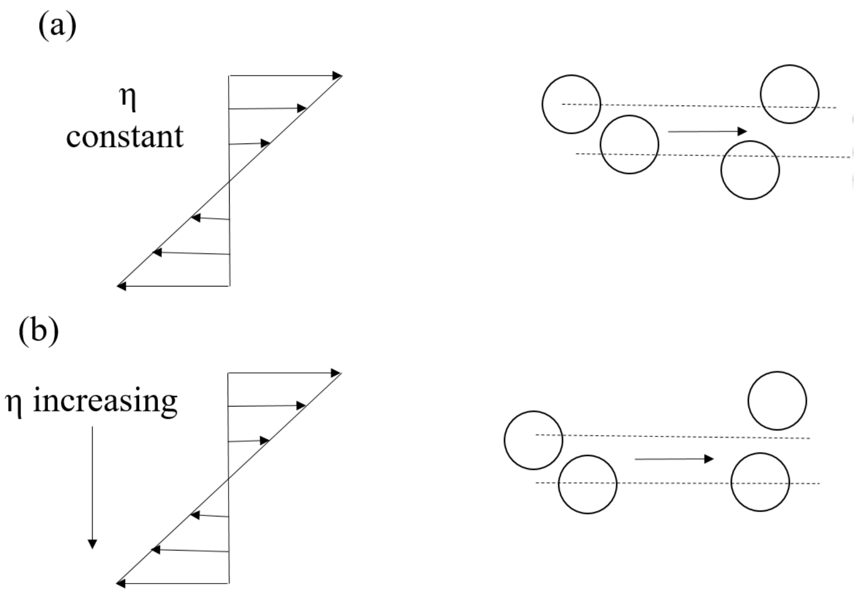

Figure 2.1: Schematic diagrams of the irreversible two-body collisions with (a) constant viscosity and (b) spatially varying viscosity (Phillips et al., 1992).

Effect of spatially varying viscosity

The spatially varying viscosity $\eta(\phi)$ caused by the existence of gradients in particle concentration as shown in Fig. 2.1(b) can also affect the interaction between two particles. A gradient in viscosity results in the resistance to motion on one side of the particle to be higher than on the other side. This results in particle being displaced in the direction of decreasing viscosity as shown in Fig. 2.1(b). The magnitude of this displacement was given quantitatively by Leighton and Acrivos (1987b). They assumed the magnitude of this displacement was proportional to $(\frac{a}{\eta})\nabla\eta$, multiplied by the particle radius. For a small gradient in concentration, the variation in viscosity is linear in the concentration gradient. The above expression, multiplied by the rate of interactions $\dot{\gamma}\phi$, gives the corresponding drift velocity. Finally, multiplying by ϕ and using Eq. 1.7 to express the gradient of viscosity in terms of $\nabla\phi$ gives the flux.

$$\boldsymbol{N_\eta} = -K_\eta a^2 \dot{\gamma}\phi^2 \frac{\nabla\eta}{\eta} = -K_\eta \dot{\gamma}\phi^2 (\frac{a^2}{\eta}) \frac{d\eta}{d\phi} \nabla\phi, \tag{2.10}$$

where K_η is a proportionality constant of order unity that can be determined from the experimental data.

Brownian diffusion

The flux of particle migration due to the Brownian motion can be expressed as:

$$\boldsymbol{N_b} = -D_b \nabla\phi, \tag{2.11}$$

where D_b is the Brownian diffusion coefficient and is given by:

$$D_b = \frac{k_b T}{6\pi\eta a}, \tag{2.12}$$

where k_b is the Boltzmann constant ($= 1.38 \times 10^{-23}$ J/K), and T is the temperature. For the particles with very high Péclet number the Brownian diffusive flux can be neglected.

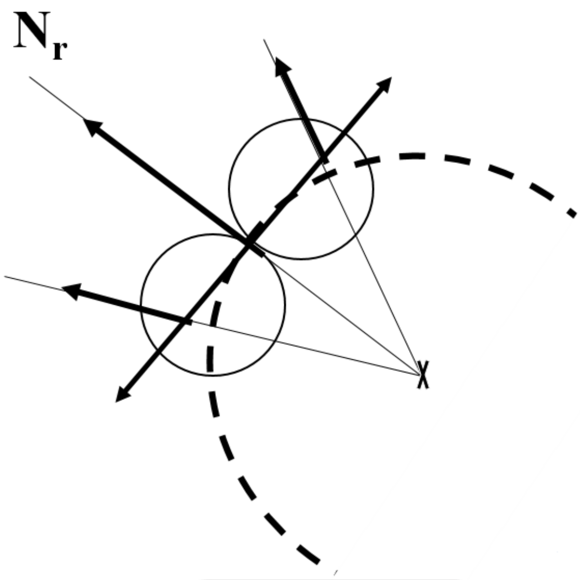

Figure 2.2: Schematic diagrams of the interaction between two particles in a curved geometry.

.

2.1.3.3 Modified diffusive flux model (Krishnan et al., 1996)

Krishnan et al. (1996) proposed that particles, interacting in a shear field with curved streamlines with non-uniform curvature, migrate towards regions with lower streamline curvature. In the parallel plate device, this effect would have resulted in an outward particle flux which, apparently, was sufficient to balance the expected inward migration due to shear-rate gradients (see Fig. 2.2). Krishnan et al. (1996) defined this additional curvature-induced flux as:

$$\boldsymbol{N_r} = K_r \boldsymbol{n} \kappa a^2 \dot{\gamma} \phi, \tag{2.13}$$

where $\boldsymbol{n}$ is the unit normal vector in the radially outward direction in curved streamline shear flows, κ is the curvature of the streamline, and K_r is an experimentally fitted parameter that must be re-adjusted with the other two previous parameters K_c, and K_η. Finally, the total migration flux in the modified Phillips model had the form:

$$\boldsymbol{N_t} = \boldsymbol{N_c} + \boldsymbol{N_\eta} + \boldsymbol{N_b} + \boldsymbol{N_r}. \tag{2.14}$$

2.1.4 Suspension balance model

Its physical concept is that an inhomogeneous stress that exists due to the particle phase inside the suspension during flow, would be responsible for the migration phenomenon of the particles in order to balance that inhomogeneity. The migration flux ($\boldsymbol{N_t}$) in Eq. 2.5 is defined as:

$$\boldsymbol{N_t} = \frac{2a^2}{9\eta_0} f(\phi)[\nabla.\boldsymbol{\Sigma}^p], \tag{2.15}$$

where $f(\phi)$ is the sedimentation hindrance function that represents the mobility of the particle phase and $\boldsymbol{\Sigma}^p$ is the particle stress tensor that depends on both the concentration of particles ϕ and the shear-rate $\dot{\gamma}$. The migration flux ($\boldsymbol{N_t}$) in this model is directly proportional to the divergence of the particle stress tensor $\boldsymbol{\Sigma}^p$. It can be seen as a result of concentration gradients in the suspension or shear-rate gradients which induce gradients in the particle stress. In other words, since $\boldsymbol{\Sigma}^p = f(\phi, \dot{\gamma})$, if $\dot{\gamma} \neq constant$ or if $\phi \neq constant$ then a particle flux appears.

2.1.4.1 Mass and momentum conservation equations

In the suspension balance model, the mixture of two phases (the particles and the fluid) is considered as a bulk suspension (continuous medium) that of course obeys the laws of conservation of mass and momentum. This approach was first developed by Nott and Brady (1994) assuming that the particle phase can be taken as a continuum. The mass conservation equation of the particle phase is given by:

$$\frac{\partial \phi}{\partial t} + \nabla.(\boldsymbol{U}^p \phi) = 0, \tag{2.16}$$

where $\boldsymbol{U}^p$ is the local velocity of the particle phase.

The particle momentum conservation at very small Reynolds number ($Re \longrightarrow 0$) and at no external force is given by:

$$\nabla.\boldsymbol{\Sigma}^p + n < \boldsymbol{F}^H >_p = \mathbf{0}, \tag{2.17}$$

where $<>_p$ is the average on the particle phase, $n := \frac{3\phi}{4\pi a^3}$ is the number density of the particles, and $\boldsymbol{F}^H$ is the hydrodynamic drag force on the particle given by:

$$\mathbf{F}^H \cong -6\pi\eta_0 a f^{-1}(\phi)(\boldsymbol{U}^p - \boldsymbol{U}), \tag{2.18}$$

where $f^{-1}(\phi)$ is the mean resistance since $f(\phi)$ is the sedimantion hindrance function that represents the mobility of the particle phase. Richardson and Zaki (1997), and Davis and Acrivos (1985) provided the form of $f(\phi)$ as:

$$f(\phi) = (1 - \frac{\phi}{\phi_m})(1-\phi)^{\alpha-1}, \tag{2.19}$$

where, $\alpha \in [2, 4]$ is a fitting parameter depending on the particles type.

The migration flux in this modelling is defined as:

$$\boldsymbol{N_t} = \phi(\boldsymbol{U}^p - \boldsymbol{U}) \tag{2.20}$$

By substituting Eq. 2.18 in Eq. 2.17 such that:

$$\boldsymbol{N_t} = \phi(\boldsymbol{U}^p - \boldsymbol{U}) = \frac{2a_2}{9\eta_0} f(\phi)[\nabla.\boldsymbol{\Sigma}^p]. \tag{2.21}$$

The general final form of the particle mass conservation equation in becomes:

$$\frac{\partial \phi}{\partial t} + \boldsymbol{U}.\nabla\phi = -\nabla.[\frac{2a_2}{9\eta_0} f(\phi)[\nabla.\boldsymbol{\Sigma}^p]]. \tag{2.22}$$

Thus, the knowledge of $\mathbf{\Sigma}^p$ and its variation in ϕ allows predicting the particles migration whatever the geometry is.

2.1.4.2 Stress tensor

In this model the total stress $\mathbf{\Sigma}$ is decomposed into the fluid phase stress $\mathbf{\Sigma}^f$, and the particle phase stress $\mathbf{\Sigma}^p$ such that:

$$\mathbf{\Sigma} = \mathbf{\Sigma}^f + \mathbf{\Sigma}^p. \tag{2.23}$$

The fluid phase stress $\mathbf{\Sigma}^f$ is defined as:

$$\mathbf{\Sigma}^f = -P\mathbf{I} + 2\eta_0 \boldsymbol{E}. \tag{2.24}$$

Morris and Boulay (1999) suggested the constitutive law for the particle phase stress for shear flows as:

$$\mathbf{\Sigma}^p = -\mathbf{\Sigma}^p_{nn} + 2\eta_0\eta_p(\phi)\boldsymbol{E}, \tag{2.25}$$

where $\mathbf{\Sigma}^p_{nn} := \eta_0\eta_N(\phi)\dot{\gamma}\boldsymbol{Q}$ is the particle normal stress diagonal tensor, $(2\eta_0\eta_p(\phi)\boldsymbol{E})$ is the particle shear-stress tensor, $\eta_p(\phi) = (\eta_s(\phi) - 1)$ is the shear viscosity of the particle phase dimensionlessed by the viscosity of the suspending liquid η_0, and $\eta_N(\phi)$ is the normal stress viscosity depending on ϕ. In their original paper, Morris and Boulay (1999) proposed the following expression for $\eta_N(\phi)$:

$$\eta_N(\phi) = K_N \left(\frac{\phi}{\phi_m}\right)^2 \left(1 - \frac{\phi}{\phi_m}\right)^{-2}, \tag{2.26}$$

where K_N is a fitting parameter that was set to 0.75 to match the experimental data of Phillips et al. (1992).

$\boldsymbol{Q}$ is a parametric symmetric tensor of the form:

$$\boldsymbol{Q} = \begin{bmatrix} 1 & 0 & 0 \\ 0 & \lambda_2 & 0 \\ 0 & 0 & \lambda_3 \end{bmatrix}, \tag{2.27}$$

that physically captures the anisotropy of the normal stress of the particle phase. Here, the principal directions of the tensor $\boldsymbol{Q}$ in Eq. 2.27 are those of a viscometric shear flow with 1, 2, 3 denoting flow, velocity gradient, and vorticity directions, respectively. $\lambda_2 = 0.8$, and $\lambda_3 = 0.5$ provide reasonably good agreement with concentrated suspension rheology (Zarraga et al., 2000) and with observed migration in viscometric flows (Chow et al., 1994b; Phillips et al., 1992).

2.2 Bidisperse suspension

2.2.1 Overview

In addition to the experimental studies on bidisperse suspension, theoretical studies have also been proposed to study the margination phenomenon in bidisperse suspension. Shauly et al. (1997) generalized the model of Phillips et al. (1992) for the bidisperse suspensions. They used a simplified coupling between different particle species and included curvature in the flow geometry but neglected the thermal diffusion and observed size segregation of particles in the Couette device, where the larger particles migrate towards the outer walls and the smaller particles accumulating at the inner walls. Later, Vollebregt et al. (2012) used a multi-fluid approach and introduced an effective temperature for the particles normal stress, which depends on the shear-rate. Recently, Kanehl and Stark (2015) extended the Phillips et al. (1992) model to the bidisperse suspensions using a more realistic expression for the collective diffusion tensor. Kanehl and Stark (2015) were also carried out particle based mesoscale simulations called multi-particle collision dynamics (MPCD) and found that using a single fit parameter for the intrinsic diffusivity, the phenomenological model accurately reproduces the MPCD simulation results.

2.2.2 Model I (Shauly et al., 1997)

According to Shauly et al. (1997), the diffusive flux of particles of species i ($\boldsymbol{N_{t,i}}$) with size a_i, is expressed as the sum of three fluxes due to gradients in interaction frequency ($\boldsymbol{N_{c,i}}$), effective viscosity ($\boldsymbol{N_{c,i}}$), and streamline curvature ($\boldsymbol{N_{r,i}}$).

$$\boldsymbol{N_{t,i}} = \boldsymbol{N_{c,i}} + \boldsymbol{N_{\eta,i}} + \boldsymbol{N_{r,i}}. \tag{2.28}$$

The frequency of interactions of particles of species i is $\dot{\gamma}\phi_i$. Since the variation in interaction frequency over a distance of $\mathrm{O}(a_i)$ scales as $a_i\nabla(\dot{\gamma}\phi_i)$, the flux resulting from the variation of interaction frequency of species i with particles of any species j can be expressed by $a_i a_j \phi_j \nabla(\dot{\gamma}\phi_i)$. Particles of species i interact with all particles in the flow, therefore, the total flux of species i due to varying collision frequency for a bidisperse suspension is given by:

$$\boldsymbol{N_{c,i}} = -K_c a_i \sum_{j=1}^{2} a_j \phi_j \nabla(\dot{\gamma}\phi_i). \tag{2.29}$$

When considering the flux related to the varying viscosity field, the relevant length scale associated with the variation in viscosity and with particle displacement is the typical size of an interacting aggregate which can be approximated by the average particle size in the suspension, given by:

$$\bar{a} = \frac{\sum_{j=1}^{2} a_j \phi_j}{\phi}, \tag{2.30}$$

where $\phi = \sum_{j=1}^{2} \phi_j$. Following the arguments of Phillips et al. (1992) (see Section 2.1.3.2) this flux is given as:

$$\boldsymbol{N_\eta, i} = -K_\eta \bar{a}^2 \dot{\gamma} \phi \phi_i \frac{\nabla \eta}{\eta} = -K_\eta \dot{\gamma} \phi \phi_i (\frac{\bar{a}^2}{\eta}) \frac{d\eta}{d\phi_i} \nabla \phi_i. \tag{2.31}$$

Following Krishnan et al. (1996), the flux of species i induced by the streamline curvature can be written as:

$$\boldsymbol{N_r, i} = -K_r \dot{\gamma} a_i \phi \phi_i \left(\frac{a_i}{\bar{a}} \right) \nabla ln \Re. \tag{2.32}$$

The coefficients K_c, K_η, and K_r in Eqs. 2.29, 2.31, and 2.32 are assumed to be the same as for the monodisperse suspension, i.e., they are considered independent of the size of the particular species.

2.2.3 Model II (Vollebregt et al., 2012)

Vollebregt et al. (2012) derived a mixture model for the particle migration in a bidisperse flowing suspension from a multi-fluid approach. The multi-fluid model assumes the liquid phase and both dispersed phases are inter-penetrating phases. The model uses the assumptions of equipartitioning of stresses and of kinetic energy over the particle phases, resulting in a single effective temperature. Vollebregt et al. (2012) demonstrated that the driving force for particle migration can be expressed in terms of non-equilibrium osmotic pressure and chemical potential. A detailed study of the model can be found in the paper by Vollebregt et al. (2012).

2.2.3.1 Governing equations

The continuity and momentum equations for the fluid phase and particle phase are given by:

$$\frac{\partial}{\partial t}(1 - \phi) + \nabla \cdot (1 - \phi) \boldsymbol{U}^f = 0, \tag{2.33}$$

$$0 = \nabla \cdot \boldsymbol{\sigma}_f - \sum_{i=1}^{2} \boldsymbol{F}^i + (1 - \phi) \rho_f \boldsymbol{g}, \tag{2.34}$$

and

$$\frac{\partial}{\partial t}\phi_i + \nabla \cdot \phi_i \boldsymbol{U}^i = 0, \tag{2.35}$$

$$0 = \nabla \cdot \boldsymbol{\sigma}_i + \boldsymbol{F}^i + \phi_i \rho_i \boldsymbol{g}, \tag{2.36}$$

respectively, where $\boldsymbol{U}^f$ is the velocity of the fluid phase, $\boldsymbol{U}^i$ is the velocity of the particle phase i, $\boldsymbol{\sigma}_f$ is the fluid stress, $\boldsymbol{\sigma}_i$ is the particle stress of the particle phase i, $\boldsymbol{F}^i$ is the momentum exchange between the fluid phase and the particle phase i, ρ_f is the density of the fluid, and ρ_i is the density of the particle phase i. Particle-fluid interactions are incorporated in the momentum exchange between the particle and the fluid, $\boldsymbol{F}^i$, and particle-particle interactions in the particle stresses, $\boldsymbol{\sigma}_i$.

Summation of the individual mass balances (Eqs. 2.33 and 2.35) and momentum balances (Eqs. 2.34 and 2.36) give the mixture continuity:

$$\frac{\partial \overline{\rho}}{\partial t} + \nabla \cdot \overline{\rho \boldsymbol{U}} = 0 \tag{2.37}$$

and momentum equation:

$$0 = \nabla \cdot \boldsymbol{\sigma}_f + \nabla \cdot (\sum_{i=1}^{2} \sigma_i) + \overline{\rho} \boldsymbol{g}, \tag{2.38}$$

where $\overline{\rho} := (1-\phi)\rho_f + \sum_{i=1}^{2}(\phi_i \rho_i)$ is the average density of the mixture and $\overline{\rho \boldsymbol{U}} := (1-\phi)\rho_f \boldsymbol{U}^f + \sum_{i=1}^{2}(\phi_i \rho_i \boldsymbol{U}^i)$ is the momentum of the mixture.

Momentum exchange consists of the buoyancy force and the drag force and given as (Vollebregt et al., 2012):

$$\boldsymbol{F}^i = \phi_i \nabla \cdot \boldsymbol{\sigma}_f + \phi_i (\overline{\rho} - \rho_i) \boldsymbol{g} + \boldsymbol{F}^{i,*}, \tag{2.39}$$

where $\boldsymbol{F}^{i,*}$ is the momentum exchange due to the drag force between the particle phase i and the fluid. The drag force is linear with the slip velocity $\boldsymbol{w}_i (:= \boldsymbol{U}^i - \boldsymbol{U}^f)$ and given by:

$$\boldsymbol{F}^{i,*} = \zeta_i(\boldsymbol{U}^i - \boldsymbol{U}^f) = \zeta_i \boldsymbol{w}_i, \tag{2.40}$$

where $\zeta_i := \frac{2\eta(\phi)}{9a_i^2}\phi_i$ is the drag coefficient for the particle phase i.

The fluid and particle phase mass balances (Eqs. 2.33 and 2.35) can be written in terms of the average mixture velocity ($\overline{\boldsymbol{U}}$), and the slip velocities ($\boldsymbol{w}_i$). The mixture velocity and slip velocities are given by:

$$\overline{\boldsymbol{U}} = (1-\phi)\boldsymbol{U^f} + \sum_{i=1}^{2}(\phi_i \boldsymbol{U}^i), \tag{2.41}$$

and

$$\boldsymbol{w}_i = \boldsymbol{U}^i - \boldsymbol{U}^f \tag{2.42}$$

respectively.

With Eqs. 2.41 and 2.42, the particle phase velocities can be written as, with $i \neq j$:

$$\boldsymbol{U^i} = \overline{\boldsymbol{U}} + (1-\phi_i)\boldsymbol{w}_i - \phi_j \boldsymbol{w}_j. \tag{2.43}$$

Substitution of Eq. 2.43 in Eq. 2.35 leads to $i \neq j$:

$$\frac{\partial \phi_i}{\partial t} + \nabla.\phi_i \overline{\boldsymbol{U}} = -\nabla.\left(\phi_i(1-\phi_i)\boldsymbol{w}_i - \phi_i\phi_j \boldsymbol{w}_j\right). \tag{2.44}$$

The fluid stress tensor is decomposed in a contribution due to pressure, P, and the viscous forces, $\mathbf{\Sigma^f}$:

$$\boldsymbol{\sigma}_i = -P\mathbf{I} + \mathbf{\Sigma^f} \tag{2.45}$$

In general the Gibbs-Duhem relation applies to stress and chemical potentials μ_i (Vollebregt et al., 2012):

$$\sum_{i=1}^{2}\nabla.\boldsymbol{\sigma_i} = \nabla.\boldsymbol{\sigma_{total}} = \nabla.\mathbf{\Pi} = \sum_{i=1}^{2}\phi_i\nabla.\mu_i, \tag{2.46}$$

where $\mathbf{\Pi}$ is the osmotic pressure of the suspension.

With use of the formulation of the momentum exchange (Eq. 2.39), the decomposition of the fluid tensor (2.45) and the division of the stress (2.46), Vollebregt et al. (2012) derived the particle evolution equation for the particle species i in terms of chemical potentials μ_i and given by:

$$\frac{\partial \phi_i}{\partial t} + \nabla.\phi_i \overline{\boldsymbol{U}} = \nabla(M_{ii}\nabla\mu_i - M_{ij}\nabla\mu_j), \tag{2.47}$$

where M denotes mobilities of the particles and are given by, with $i \neq j$:

$$M_{ii} = \frac{\phi_i^2(1-\phi_i)^2}{\zeta_i} + \frac{\phi_i^2\phi_j^2}{\zeta_j} \tag{2.48}$$

$$M_{ij} = \phi_i\phi_j\left(\frac{\phi_i(1-\phi_i)}{\zeta_i} + \frac{\phi_j(1-\phi_j)}{\zeta_j}\right) \tag{2.49}$$

By applying the given procedure on the Boublik-Manssori-Carnahan-Straling-Leland equation of state, Vollebregt et al. (2012) derived the chemical potential of the particle species i to be:

$$\mu_i = \left(\frac{3d_i^2\langle d^2\rangle^2}{\langle d^3\rangle^2} - \frac{2d_i^3\langle d^2\rangle^3}{\langle d^3\rangle^3} - 1\right)\ln(1-\phi)+ \tag{2.50}$$

$$\left(\frac{\pi d_i^3 n}{6} + \frac{3d_i}{\langle d^3\rangle}\phi\left(\langle d^2\rangle + d_i\langle d\rangle - \frac{d_i^2\langle d\rangle\langle d^2\rangle}{\langle d^3\rangle}\right)\right)\frac{1}{1-\phi}+ \tag{2.51}$$

$$\left(\frac{3\langle d\rangle\langle d^2\rangle}{\langle d^3\rangle}\frac{\pi d_i^3 n}{6} + \phi\left(3d_i^2 - \frac{3d_i^2\langle d^2\rangle^2}{\langle d^3\rangle^2} - \frac{2d_i^3\langle d^2\rangle^3}{\langle d^3\rangle^3}\right)\right)\frac{1}{(1-\phi)^2}+ \tag{2.52}$$

$$\phi(3-\phi)\frac{\langle d^2\rangle^3}{\langle d^3\rangle^2}\frac{\pi d_i^3 n}{6}\frac{1}{(1-\phi)^3} \tag{2.53}$$

where $\langle d^n\rangle := \sum_i^2 \frac{n_i}{n_s}$ is the n-th moment of the particle diameters, n_i is the total number of particles of the particle species i, and $d_i := 2a_i$ is the diameter of the particle species

i.

2.2.4 Model III (Kanehl and Stark, 2015)

Kanehl and Stark (2015) extended the work of Phillips et al. (1992) model to bidisperse suspension. The model introduces drift or migration currents due to a gradient in the particle collision frequency as well as a spatially varying viscosity and it also includes collective diffusion. A detailed study of the model can be found in the paper Kanehl and Stark (2015). According to this model, the expression for the particle migration flux ($\boldsymbol{N_{t,i}}$) of particle type i can be written as:

$$\boldsymbol{N_{t,i}} = \sum_{j=1}^{2} \left(-\phi_i A_{ij} \left(K_c \nabla(\phi_i \dot{\gamma}) + K_\eta \phi_j \dot{\gamma} \frac{\nabla \eta}{\eta} \right) - D_b^{ij} \nabla \phi_j \right), \tag{2.54}$$

where A_{ij} is the coupling matrix which contains the geometrical factors, and D_b^{ij} is the collective diffusion matrix which couples a non-uniform particle concentration of type j (i.e ϕ_j) to a particle migration flux of type i.

The coupling matrix (A_{ij}) can be given as:

$$A_{ij} = \frac{(a_i + a_j)^2}{2} \frac{\left(1 + \frac{a_i}{a_j}\right)^d}{1 + \left(\frac{a_i}{a_j}\right)^d}, \tag{2.55}$$

where d is the dimension of the domain.

The diagonal elements of the collective diffusive tensor can be given as:

$$D_b^{ii} = K_d D_0^i S^{-1}, \tag{2.56}$$

where K_d is the fitting parameter, D_0^i is the single particle diffusivity, and S is the static structure factor. Kanehl and Stark (2015) found out $K_d/K_c = 0.61$ and $K_d/K_c = 7.46$ for 2D and 3D respectively by comparing the model with particle based mesoscale simulation method called multi-particle collision dynamics (MPCD).

The single particle diffusivity (D_0^i) is same as that of the monodisperse case. Only the radius is replaced by the respective quantity and reads as:

$$D_0^i = \frac{k_b T}{6\pi\eta a_i}. \tag{2.57}$$

The static structure factor in 2D was approximated by Boublík (1975) and given as:

$$S(\phi) = \frac{(1-\phi^2)}{1-\phi(1-\gamma)}, \tag{2.58}$$

with

$$\gamma = \frac{\left(\sum_{j=1}^{2} c_j a_j\right)^2}{\sum_{j=1}^{2} c_j a_j^2}, \tag{2.59}$$

where $c_j := \phi_i / V_{sph}$ is the particle density, and V_{sph} is the volume of a sphere in 3D or the area of a disk in 2D flows.

The static structure factor in 3D was approximated by Ashcroft and Langreth (1967) and given as:

$$S(\phi) = \frac{(1-\phi^4)}{(1+2\phi)^2-\Delta}, \tag{2.60}$$

with

$$\Delta = \frac{3x(1-x)\phi(1-\alpha)^2}{x+(1-x)\alpha^3}\left((2+\phi)(1+\alpha)+\frac{3\phi\alpha}{x+(1-x)\alpha^3}((1-x)\alpha^2+x)\right), \tag{2.61}$$

where, $\alpha = a_i/a_j$, and $x = c_i/\sum_{j=1}^{2} c_j$.

The non-diagonal elements of the collective diffusive tensor can be given as Kanehl and Stark (2015):

$$D_b^{ij} = D_b^{ii}\frac{\phi_i}{(1-\phi_j)^2}. \tag{2.62}$$

2.2.5 Species conservation equation

The dynamic changes in concentration are obtained from the particle conservation equations:

$$\frac{\partial \phi_i}{\partial t} + \boldsymbol{U}.\nabla \phi_i = -\nabla.\boldsymbol{N_{t,i}}, \tag{2.63}$$

and

$$\frac{\partial \phi}{\partial t} + \boldsymbol{U}.\nabla \phi = -\nabla.\boldsymbol{N_t}, \tag{2.64}$$

for species i and for the total concentration respectively. Here, the total flux is given as:

$$\boldsymbol{N_t} = \sum_{j=1}^{2} \boldsymbol{N_{t,i}} \tag{2.65}$$

2.2.6 Suspension viscosity

The application of the Eqs. 2.63, and 2.64 to specific flows requires the use of an expression for the effective viscosity (Kanehl and Stark, 2015). For monodisperse suspension, the effective viscosity is calculated by the use of Eq. 1.7:

$$\eta(\phi) = \eta_0 \left(1 - \frac{\phi}{\phi_m}\right)^{-2.5\phi_m}, \tag{2.66}$$

The maximum packing concentration for a monodisperse suspension assumed $\phi_m = 0.68$ (Phillips et al., 1992). Kanehl and Stark (2015) extended the Eq. 2.66 to describe the effective viscosity of a bidisperse suspension by following the approach suggested by Probstein et al. (1994). According to their study, the maximum packing concentration (ϕ_m) for bidisperse suspension is not a constant but, rather, it is calculated as a function of individual species concentrations and reads:

$$\phi_{m,bi} = \phi_m \left[1 + \frac{3}{2} |b|^{\frac{3}{2}} \left(\frac{\phi_i}{\phi}\right)^{\frac{3}{2}} \left(\frac{\phi_j}{\phi}\right)\right], \tag{2.67}$$

with

$$b = \frac{a_i - a_j}{a_i + a_j}. \tag{2.68}$$

Chapter 3

Numerical implementation and validation of the models

3.1 Overview

In this manuscript, we utilize the OpenFOAM® environment which uses the finite volume method (FVM) to solve the system of partial differential equations (PDEs). The OpenFOAM® (Open Source Field Operation and Manipulation) CFD Toolbox is a free, open source CFD code produced by the “OpenCFD Ltd.”. OpenFOAM® can solve systems of partial differential equations ascribed on any 3D unstructured mesh of polyhedral cells. The fluid flow solvers are developed within a robust, implicit, pressure-velocity, iterative solution framework. It has a large user base across most areas of engineering and science, from both commercial and academic organizations. OpenFOAM® has an extensive range of features to solve anything from complex fluid flows involving chemical reactions, turbulence and heat transfer, to solid dynamics and electromagnetism.

3.2 Monodisperse suspension

3.2.1 Model governing equations

The shear-induced migration models described previously in chapter 2 for the incompressible Stokes flow of monodispersed neutrally buoyant non-Brownian suspensions of hard spheres, can be summerized by the following system of three coupled equations:

$$\nabla.\boldsymbol{U} = 0, \tag{3.1}$$

$$\nabla.\boldsymbol{\Sigma} = 0, \tag{3.2}$$

$$\frac{\partial \phi}{\partial t} + \boldsymbol{U}.\nabla\phi = -\nabla.\boldsymbol{N_t}, \tag{3.3}$$

where $\boldsymbol{U}$ is the suspension mean velocity field vector, $\boldsymbol{\Sigma}$ is the suspension stress tensor, and $\boldsymbol{N_t}$ is the shear-induced migration flux of particles relative to the mean motion of the suspension that were all defined precisely in chapter 2.

The shear-induced migration models encounter difficulties in the regions where the local shear-rate approaches to zero. For example, in the pressure-driven flows, the shear-rate at the channel center is zero. Since the shear-induced diffusivity is linearly proportional to the local shear-rate, at the center the model predicts maximum particle volume fraction which is not observed in the experiments. This leads to numerical instability and convergence problem as $\phi \longrightarrow \phi_m$. To overcome this difficulty a small non-local shear-rate $\dot{\gamma}_{nl}$ proposed by Miller and Morris (2006), which is a function of particle size and width of the channel, is added to the local shear-rate $\dot{\gamma}$. The non-local shear-rate ($\dot{\gamma}_{nl}$) is given by:

$$\dot{\gamma}_{nl} = a_s(\epsilon)\frac{U_{max}}{H}, \tag{3.4}$$

where, $a_s(\epsilon)$ is equal to 0, ϵ, or ϵ^2 and $\epsilon = \frac{a}{H}$.

The system of Eqns. 3.1, 3.2, and 3.3 is implemented by modifying "transientSimple-

Foam" solver in the OpenFOAM® to a new solver which represents DFM and SBM. The actual code that solves the scalar transport equation in OpenFOAM® is represented in Appendix A. The SIMPLE scheme was employed for the pressure-velocity coupling and its brief description was given in Appendix B. The solver settings and schemes used in the present steady are shown in Appendix C. The brief description of the code implementation procedure inside the transientSimpleFoam solver is shown in Appendix D:

The imposed boundary conditions for the suspension flow through channel to be used in the system of Eqs. 3.1, 3.2, and 3.3 are represented in Fig. 3.1:

1. At the inlet, the uniform inlet velocity $\boldsymbol{U_{avg}}$ and the uniform particle concentration ϕ_{bulk} is applied.

2. At the outlet, fully-developed flow condition has been applied. (i.e. surface normal gradients are zero: $\nabla\phi.\boldsymbol{n} = 0$, where $\boldsymbol{n}$ is the surface normal vector)

3. At the walls, no-slip boundary condition for the velocity field and no flux boundary condition for the concentration have been applied.

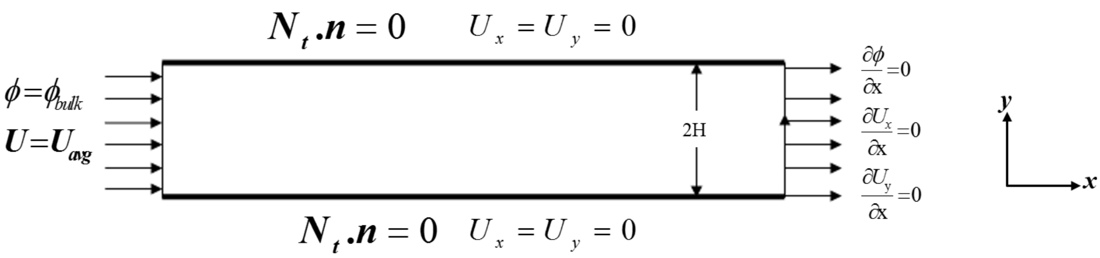

Figure 3.1: Imposed boundary conditions.

The success of any numerical simulation depends on how close it resembles the analytical solution, as well as experimental observations. This is usually done by comparing with previous simulation or experimental data available in the literature. In the present work we have first conducted numerical simulations for suspension in both rectangular and circular cross-sectional channels and the results are compared with available experimental data. The flow rate and other simulation parameters are considered same as that of experiments. The length required for the fully-developed flow was calculated by using the correlation proposed by Nott and Brady (1994),

$$\left[\frac{L}{H}\right]_{ss} \geqslant \frac{1}{12d(\phi)}\left[\frac{H}{a}\right]^2, \tag{3.5}$$

where, L is the length required for steady state, H is the half width of the channel and the function $d(\phi)$ accounts for the effect of particle concentration on shear-induced coefficient of diffusion.

$$d(\phi) = \frac{1}{3}\phi^2\left(1+\frac{1}{2}e^{8.8\phi}\right). \tag{3.6}$$

The validation of the monodispersed models have been carried out with the experimental data of the suspension flow in the 2D rectangular (Lyon and Leal, 1998a) and circular cross-section conduit (Hampton et al., 1997). Lyon and Leal (1998a) measured the distribution of the particles in the 2D rectangular conduit by using laser Doppler velocimetry (LDV) method. on the other hand, Hampton et al. (1997) measured the particle distribution in the pipe flow by using NMR imaging technique. The computational domain of the channel is meshed using already installed "blockMesh" utility in OpenFOAM® and its brief description is explained in Appendix E. The minimum length of the channel for the fully-developed flow is calculated based on the Nott and Brady (1994) formula (Eq. 3.5). The geometry and simulation parameters used for the validation of the models in the 2D rectangular conduit and pipe flow are shown in Table. 3.1 and Table. 3.2 respectively.

3.2.2 Validation of the DFM

The flow of suspensions in the rectangular conduits is simulated and compared with the experimental data of Lyon and Leal (1998a). Fig. 3.2 shows the comparison of DFM

Table 3.1: Geometry details and simulation parameters for the validation of monodispersed models in the rectangular conduit.

S.No	Parameter	Symbol[Unit]	Value
1	Particle radius	a [μm]	50
2	Ratio of channel width to particle radius	H/a [m]	18
3	Fluid viscosity	η_0 [Pa.s]	0.48
4	Fluid density	ρ [kg.m^{-3}]	1190

Table 3.2: Geometry details and simulation parameters for the validation of monodispersed models in the pipe flow.

S.No	Parameter	Symbol[Unit]	Value
1	Particle radius	a [μm]	325
2	Ratio of channel width to particle radius	H/a [m]	16
3	Fluid viscosity	η_0 [Pa.s]	2.1
4	Fluid density	ρ [kg.m^{-3}]	1180.7

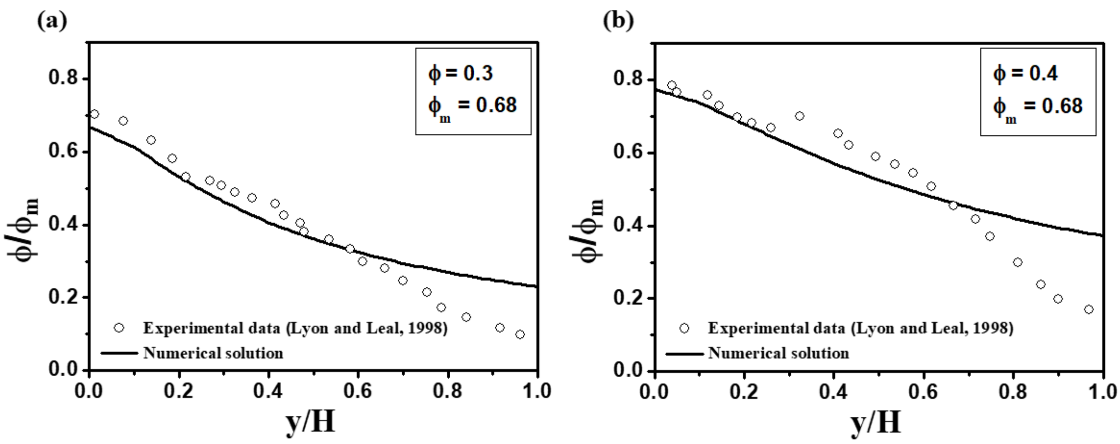

Figure 3.2: Comparison of the particle concentration profile obtained from DFM simulations with the experimental data in a channel flow for (a) $\phi = 0.3$, and (b) $\phi = 0.4$.

results with the experimental data of Lyon and Leal (1998a) for bulk particle volume fraction (ϕ) of 0.3 and 0.4. The simulation parameters for the validation in rectangular conduit are shown in Table. 3.1. Similarly, the flow of suspensions in the pipes is simulated and compared with the experimental data of Hampton et al. (1997) for bulk particle volume fraction (ϕ) of 0.2 and 0.3 in Fig. 3.3. The simulation parameters for

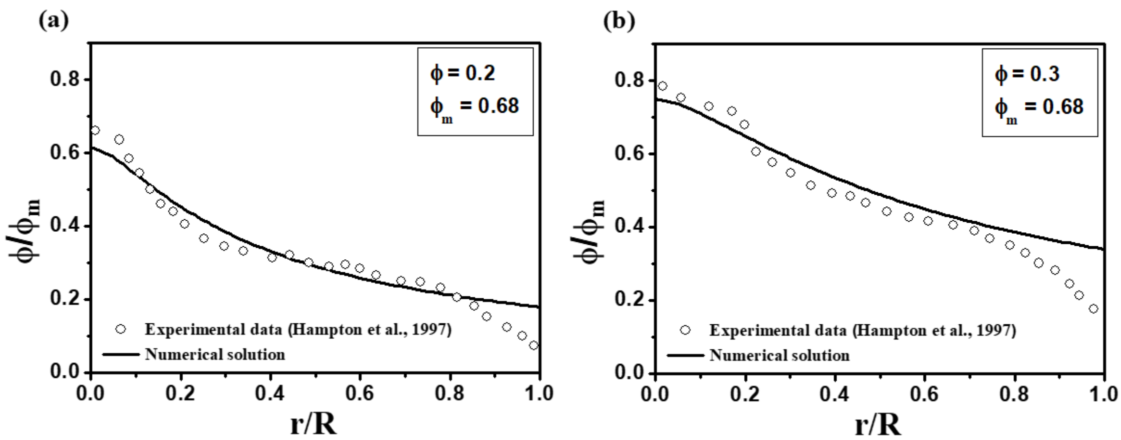

Figure 3.3: Comparison of the particle concentration profile obtained from DFM simulations with the experimental data in a pipe flow for (a) $\phi = 0.2$, and (b) $\phi = 0.3$.

the validation in circular cross-section conduit are shown in Table. 3.2. In this work, the diffusive constants in the DFM were taken as constant ($K_c = 0.41$ and $K_\eta = 0.62$) (Phillips et al., 1992). The shear-induced migration causes the particles to migrate from the high shear-rate wall regions to the low shear-rate channel center. Therefore, the particle concentration at the centerline is high compared to the concentration at the walls. Except at the channels walls, the numerical results are in good agreement with the experimental data. Most of the experiments on shear-induced particle migration have reported difficulty in collecting the reliable data in the wall region. It is also noted that the bulk area averaged concentration determined from the simulation shows about 3-4% deviation resulting from numerical errors, whereas the experimental values exhibit much larger errors (8%). We also observe these facts in the work of Lyon and Leal (1998a) that have also compared their experimental data with the DFM and SBM predictions. They have attributed this to error in finding the correct particle concentration near the channel walls. Allende and Kalyon (2000) have evaluated effect of wall slip on particle migration models and observed that the introduction of wall slip decreases the deviation of the wall concentration from the initial concentration. However, the correct assessment of the various parameters influencing the particle migration becomes difficult due to the fact that the migration itself introduces source of error in rheological characterization of concentrated suspensions.

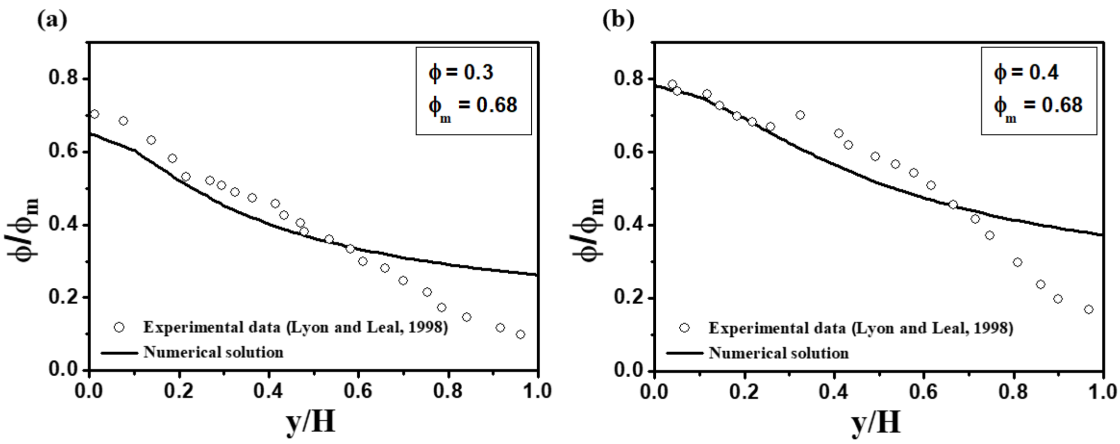

Figure 3.4: Comparison of the particle concentration profile obtained from SBM simulations with the experimental data in a channel flow for (a) $\phi = 0.3$, and (b) $\phi = 0.4$.

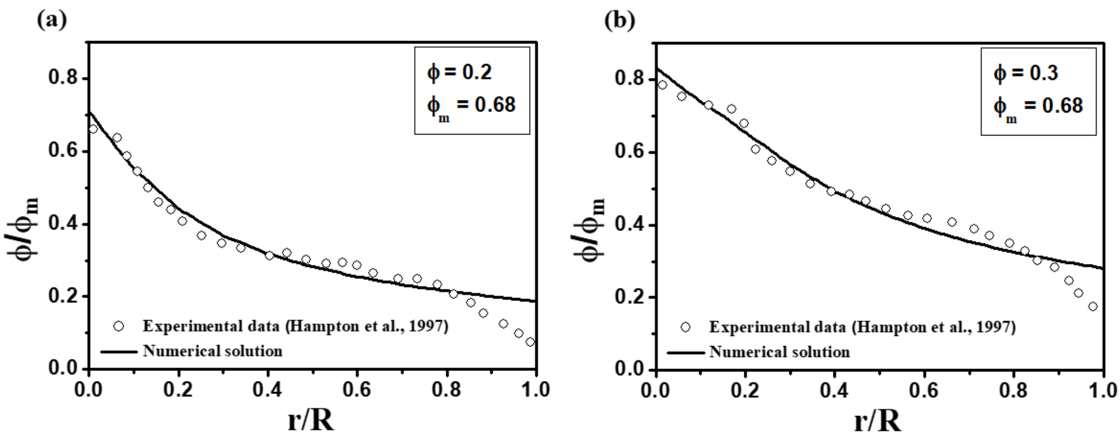

Figure 3.5: Comparison of the particle concentration profile obtained from SBM simulations with the experimental data in a pipe flow for (a) $\phi = 0.2$, and (b) $\phi = 0.3$.

3.2.3 Validation of the SBM

The comparison of the SBM simulation results with the experimental data is shown in Figs. 3.4 and 3.5 for the suspension flow in the rectangular conduit and pipe respectively. In the present work, we have used the suspension balance model which was extended by

Dbouk et al. (2013) followed by the previous efforts of Miller and Morris (2009) to the two-dimensional flows through the frame-invariant formulations to the non-viscometric flows to account for local kinematics of the suspension (see Appendix F). Good closeness is observed between our numerical results and the experimental data. In the rectilinear flows, both DFM and SBM predict similar behavior of the particle migration.

Table 3.3: Geometry details and simulation parameters for the validation of bidispersed models in the channel flow.

S.No	Parameter	Symbol[Unit]	Value
1	Smaller particle radius	a_S [μm]	0.7
2	Larger particle radius	a_L [μm]	1.5
3	Width of the channel	$2H$ [μm]	50
4	Smaller particle concentration	$\overline{\phi}_S$	0.1
5	Larger particle concentration	$\overline{\phi}_L$	0.1

3.3 Bidisperse suspension

The bidispersed models have been validated with the experimental work of Semwogerere and Weeks (2008) for a bidisperse suspension in the straight channel with a half-width (H) of 25 μm. At the entrance of the channel, the average concentration of the two species was equal ($\overline{\phi}_S = \overline{\phi}_L = 0.1$) with $a_S = 0.7$ μm and $a_L = 1.5$ μm. The subscripts S, and L denote the smaller particles and the larger particles respectively and $\overline{\phi}_i$ denotes the average inlet concentration of the species i. The geometry and simulation parameters used for the validation of the models are shown in Table. 3.3.

3.3.1 Validation of the model I (Shauly et al., 1997)

Fig. 3.6 shows the comparison between simulation results and data from the experiments of Semwogerere and Weeks (2008) for a bidisperse suspension by using Shauly et al. (1997) model. The model captures the migration of bigger particles but not able to capture the size segregation. The model predicts the enrichment of the smaller particles

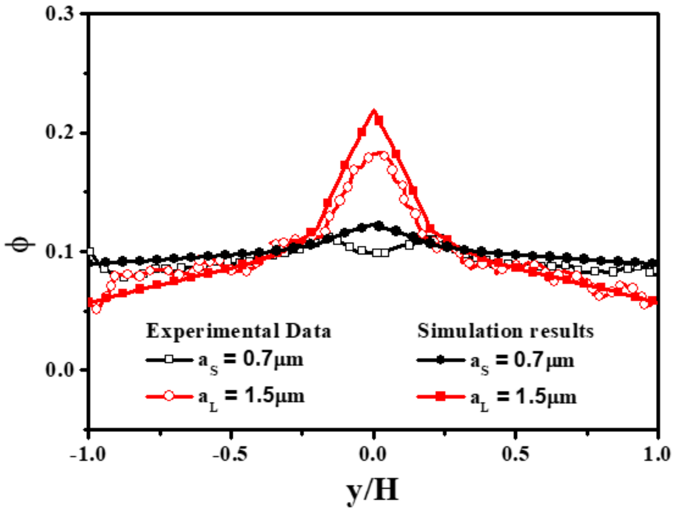

Figure 3.6: Comparison of simulation results with experimental data of Semwogerere and Weeks (2008) for bidisperse suspension flow in a straight channel by using model I.

at the channel center. But this is not the case in the experimental data of Semwogerere and Weeks (2008). To overcome the drawback, Kanehl and Stark (2015) revisited the model by adding collective diffusion of the particles.

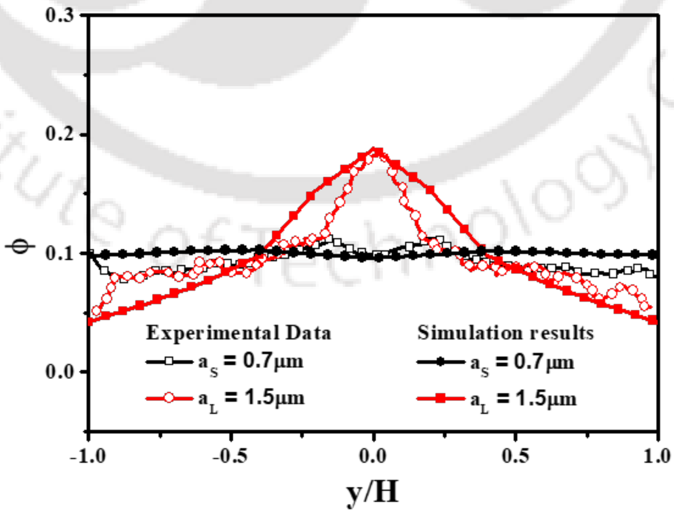

Figure 3.7: Comparison of simulation results with experimental data of Semwogerere and Weeks (2008) for bidisperse suspension flow in a straight channel by using model II.

3.3.2 Validation of the model II (Vollebregt et al., 2012)

Fig. 3.7 shows the comparison between simulation results and data from the experiments of Semwogerere and Weeks (2008) for a bidisperse suspension. The model successfully captures the qualitative behavior of particle migration observed in the experiment.

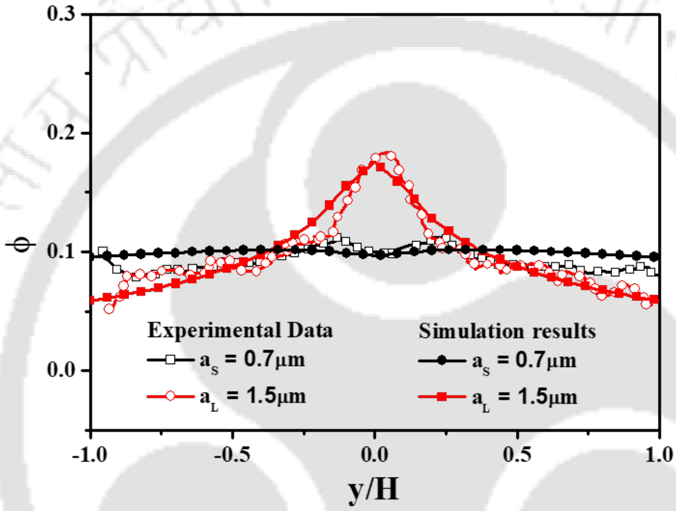

Figure 3.8: Comparison of simulation results with experimental data of Semwogerere and Weeks (2008) for bidisperse suspension flow in a straight channel by using model III.

3.3.3 Validation of the model III (Kanehl and Stark, 2015)

Fig. 3.8 shows a comparison between simulation results and data from the experiments of Semwogerere and Weeks (2008) for a bidisperse suspension. Previous experimental studies of Husband et al. (1994), Lyon and Leal (1998b), and Semwogerere and Weeks (2008) explained that the enrichment of the larger particles at the channel center is due to the particle size scaling of shear-induced migration flux in both Brownian and non-Brownian suspension. According to their study, since the migration flux scales linearly with the square of the particle size, the size segregation of the particles is a result of the faster migration of the larger particles to the channel center than that of the smaller particles in the bidisperse suspension having an equal concentration of the individual species. Kanehl and Stark (2015) reported that the diffusional current close to the wall is neglected. However, at the channel center, thermal collective diffusion dominates and leads to the size segregation of the particles. The model successfully captures the qualitative behavior of particle migration observed in the experiments.

Chapter 4

Suspension flow through a 3D oblique bifurcating channel

4.1 Overview

After validation of the numerical implementation with the experimental data of migration in straight channel we have performed the simulations for the suspension flow in 3D asymmetric oblique bifurcating channel. This type of bifurcation channels are often encountered in industry, nature and human body. The important tasks are to find out the distribution of the velocity and concentration profiles in the daughter branches and the bulk suspension and particle partitioning in the daughter branches for the better understanding of the flow behavior. Both diffusive flux model and suspension balance model were used in the simulations and compared. The suspension considered in this chapter was non-colloidal, mono-dispersed, and non-Brownian rigid particles suspended in Newtonian fluid.

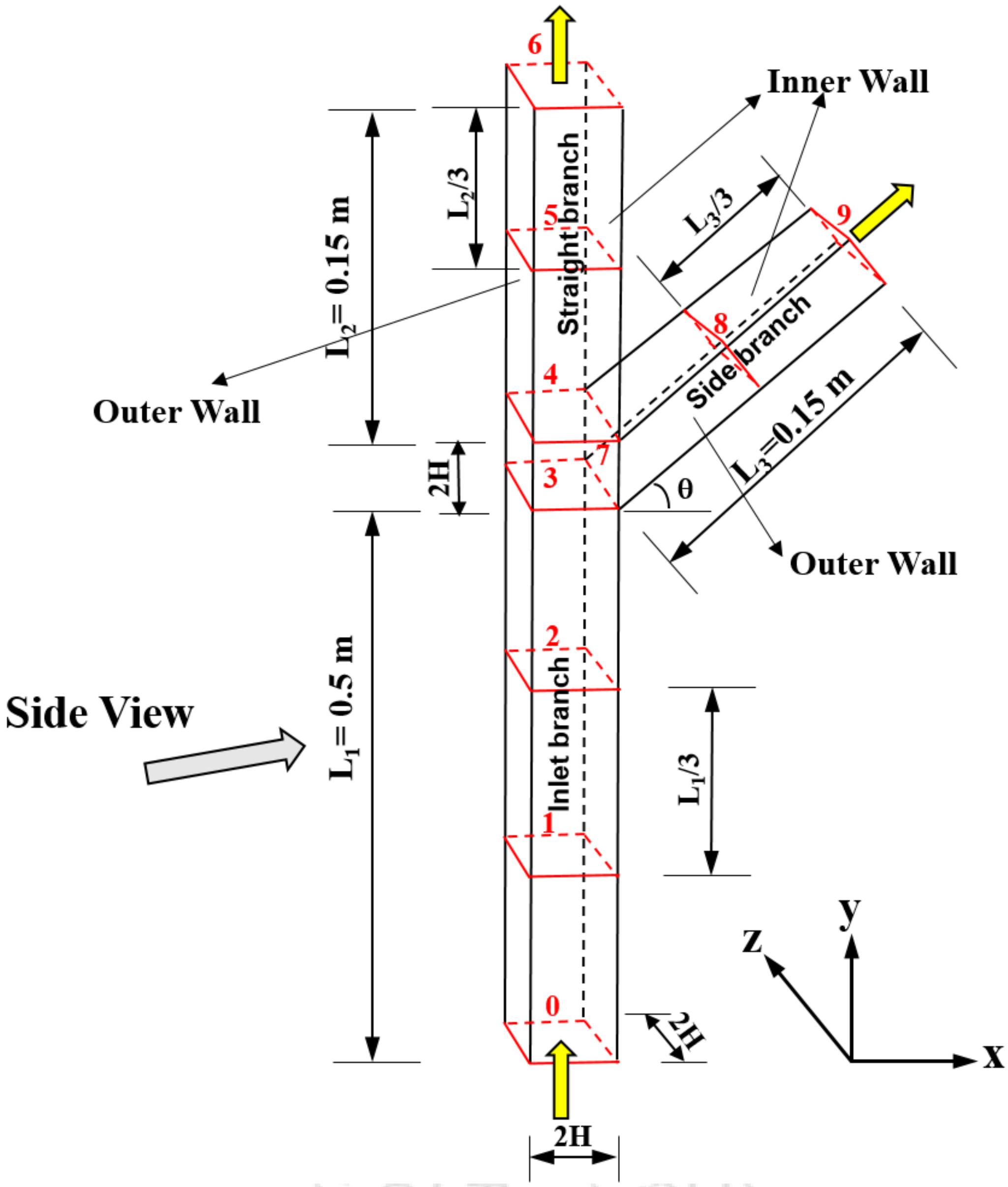

Figure 4.1: The schematic diagram of the computational geometry and locations where the concentration and the velocity profiles were analyzed.

4.2 Problem description

The schematic diagram of the 3D asymmetric oblique bifurcating channel is shown in Fig. 4.1. As shown in the Fig. 4.1, inlet branch also termed as parent branch with equal

Table 4.1: Geometry details and simulation parameters.

S.No	Parameter	Symbol[Unit]	Value
1	Width of the channel	$2H$ [m]	0.0018
2	Bifurcation angle	θ	0^0, 30^0, & 45^0
3	Fluid viscosity	η_0 [Pa.s]	0.48
3	Fluid density	ρ [kg.m^{-3}]	1190
4	Particle radius	a [μm]	50
5	Average inlet velocity	U [m.s^{-1}]	0.0063
6	Average inlet concentration	ϕ	0.3

width and depth ($2H = 0.0018$ m) divides into two daughter branches (one branch follows the inlet branch, termed as main branch and another branch bifurcates with an angle θ with the horizontal, termed as side branch) in such a manner that the two daughter branches having same depth as that of inlet branch ($2H$). However, to study the effect of unequal daughter branch width on the flow and particle distribution, we have considered the side branch in such a way that the width of the side branch ($2B\cos\theta$) varies with bifurcating angle θ, whereas the main branch has the same width ($2H$) as that of parent branch. Asymmetric T-Junction bifurcating channel (for $\theta = 0^0$) is a special case, where the two daughter branches have same width as that of parent branch. The lengths of the parent and daughter branches were 0.5 m and 0.15 m respectively, which were calculated based on the minimum length requirement criteria for fully-developed flow proposed by Nott and Brady (1994). The other simulation parameters are shown in Table 4.1. For the quantitative measure, we have analyzed velocity and concentration fields at different locations in the parent branch (location 0-3), main branch (location 4-6), and side branch (location 7-8) as shown in the Fig. 4.1. In local coordinate system, x denotes lateral/gradient direction, y denotes flow direction, and z denotes span-wise/vorticity direction. We have considered three bifurcating channels corresponding to three different bifurcating angles $\theta = 0^0$, 30^0, and 45^0 and the particle concentration was 30% in all cases. For the comparison purpose, we have also carried out simulations of pure fluid flow in the bifurcating channel.

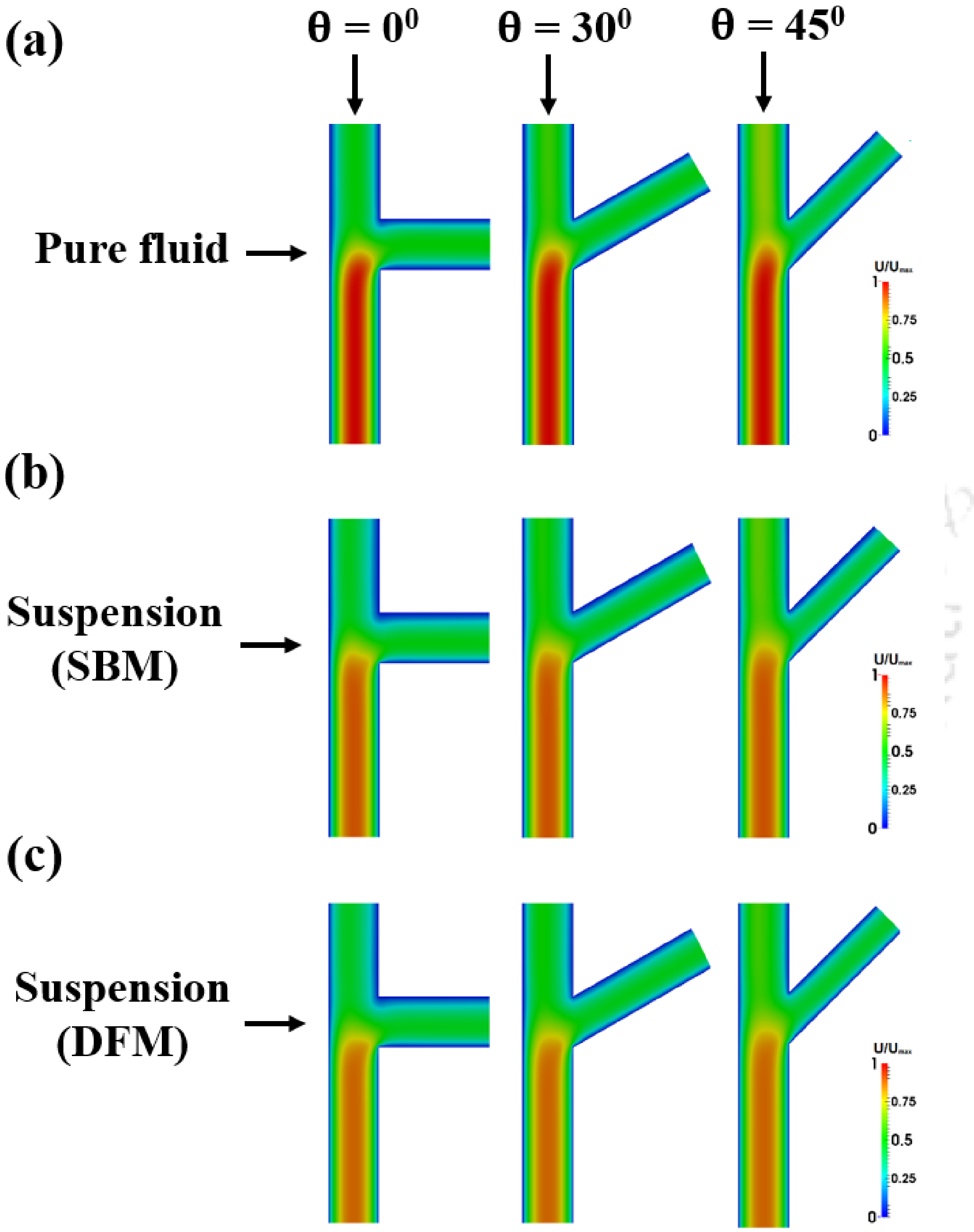

Figure 4.2: The comparison of velocity contour planes of Newtonian (a) with that of suspension in the flow direction (x-y plane) for various bifurcation angles by using SBM (b), and DFM (c).

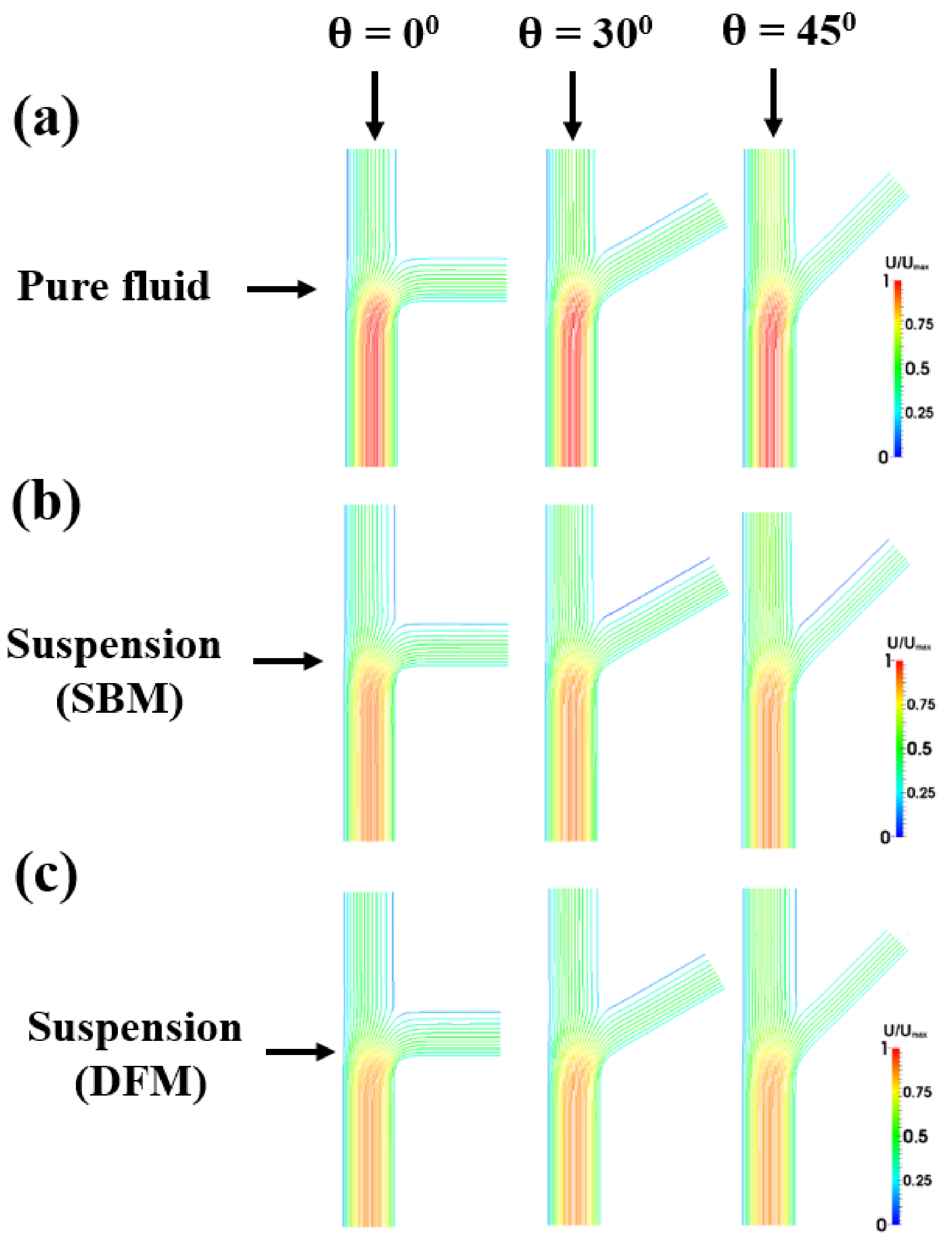

Figure 4.3: The comparison of flow stream fields of Newtonian (a) with that of suspension in the flow direction ($x-y$ plane) for various bifurcation angles by using SBM (b), and DFM (c).

4.3 Results and discussion

4.3.1 Velocity field

The impact of the particle phase on the velocity field usually studied by comparing the suspension velocity field with that of the pure fluid. The magnitude of velocity contours for pure fluid for various bifurcating angles in the flow direction at mid-plane ($z = 0.0009$ m) are shown in Fig. 4.2(a). The corresponding contours for suspension with 30% bulk particle volume fraction by using SBM and DFM are shown in Figs. 4.2(b) and 4.2(c) respectively. These velocity magnitudes were normalized with the fully-developed pure fluid center-line velocity (U_{max}) and for the purpose of clarity, these contours were drawn around the bifurcating junction. Both the models observed that the velocity profile of flowing suspension in the bifurcating channel was blunted, and it was different from that of the pure Newtonian fluid. Another marked difference between the suspension and Newtonian velocity fields is that near the bifurcation stronger deceleration is apparent in the case of suspension compared with the Newtonian fluid. This discrepancy was attributed to the migration of the particles from high shear-rate wall region to the low shear-rate center of the channel (Averbakh et al., 1997; Karnis et al., 1966; Koh et al., 1994). Qualitatively both SBM and DFM shows the same behavior at the junction of bifurcation.

The comparison of the Newtonian fluid streamline patterns (Fig. 4.3a) with that of suspension by using SBM (Fig. 4.3b) and DFM (Fig. 4.3c) around the bifurcation junction corresponding to the Fig. 4.2 is shown in Fig. 4.3. The partitioning of the fluid and particles greatly depends on the position of dividing streamlines. As the bifurcation angle increases the ratio of main branch width to the side branch width increases and thereby the percentage fluid enters into the main branch increases with θ. Thus, the dividing streamline position shifts towards the side branch as bifurcating angle increases. One more interesting observation is that the particle phase present in the fluid tries to

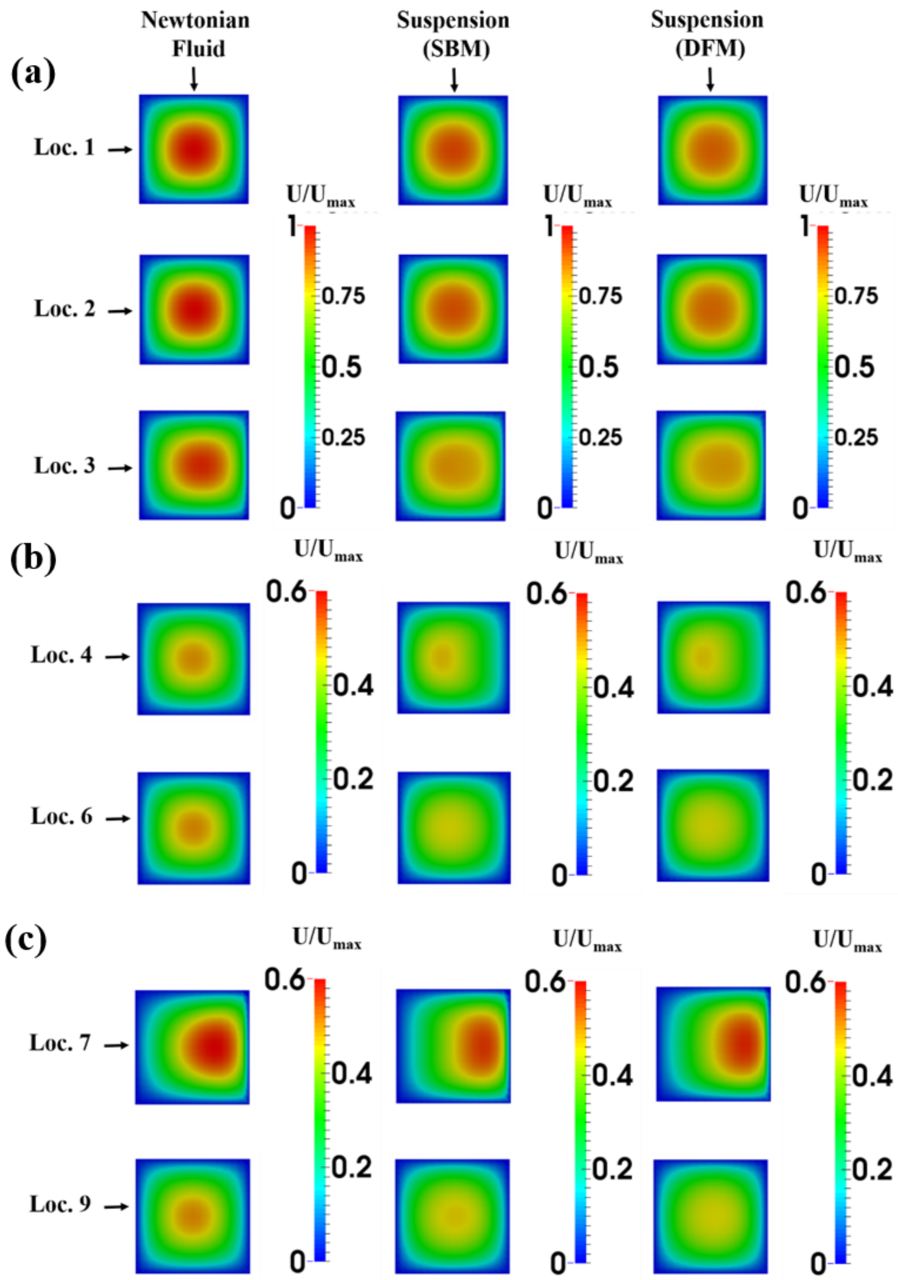

Figure 4.4: The cross-sectional contours of velocity magnitude for Newtonian fluid and suspension at various locations in the parent branch (a), main branch (b), and side branch (c). The bifurcation angle θ was 0^0.

shift the position of the dividing streamlines towards the center-line of the channel.

The cross-sectional velocity contours at various locations in the parent (Fig. 4.4a)

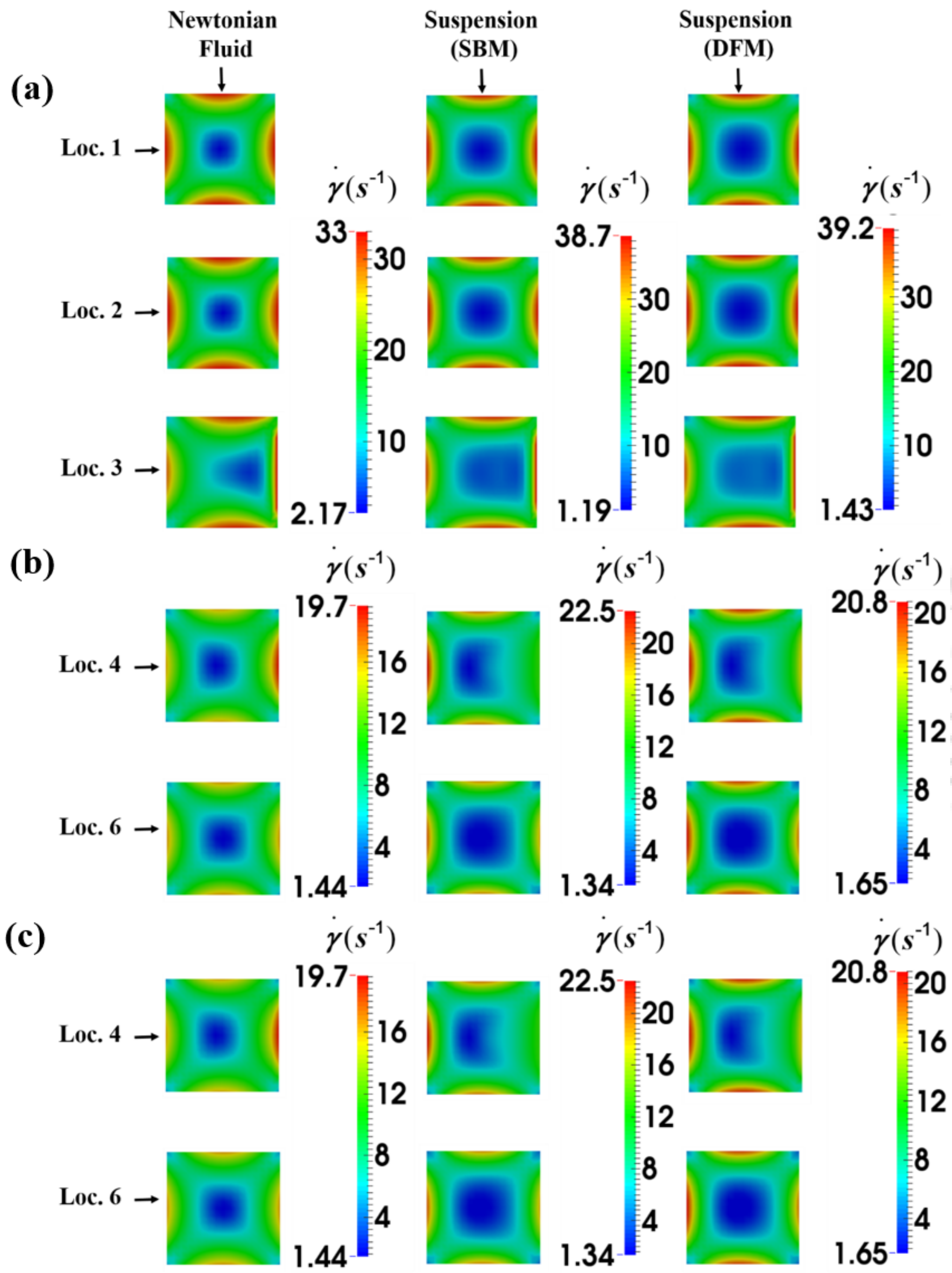

Figure 4.5: The cross-sectional contours of shear-rate for Newtonian fluid and suspension at various locations in the parent branch (a), main branch (b), and side branch (c). The bifurcation angle θ was 0^0.

and daughter (Figs. 4.4b & c) branches for $\theta = 0^0$ are shown in Fig. 4.4. These contours are drawn at different locations in the direction perpendicular to the flow. Since in the case of Newtonian fluid flow, the velocity field would become fully developed within several diameters downstream from the inlet, the contours at location 1 and 2 in the parent branch are almost similar. On the other hand, in the case of suspension, the coupled velocity and concentration profiles develop much more slowly and thus there is a noticeable discrepancy in the contours at location 1 and 2. At bifurcation point (location 3) since the flow diverges into the main and side branch, the maximum velocity does not persist and the flow starts decelerating in the lateral direction towards the side branch. As compared with the Newtonian fluid, the suspension shows greater deceleration and the presence of the particle phase in the suspension is responsible for it. At locations 4 and 8 (which are beginning locations of the main branch and the side branch respectively), the maximum velocity magnitude shifts towards outer walls of the channel and becomes asymmetric. This asymmetry is pronounced more in the case of suspension. As the fluid moves towards the downstream locations of the daughter branches, the flow gets stabilize and the velocity maximum shifts towards channel center-line (see Fig. 4.4). Fig. 4.5 shows the corresponding cross-sectional contours of the local shear-rate at different locations in the parent (Fig. 4.5a) and daughter branches (Figs. 4.5b & c). It is observed that in the parent branch, high shear-rate at the walls region and low at the center core region of the channel. The corner regions of the channel have relatively low shear-rate than the wall edges, but high when compared with that of the center core. After the bifurcation, the shear-rate at the outer walls was greatest but gradually shifts towards the channel center-line as the fluid flows towards the downstream locations of the daughter branches. Moreover, the side branch shows high shear-rate compared with the main branch.

The velocity profiles in the upstream locations (up to location 2) of the parent branch do not feel the effect of bifurcation and same for all the bifurcation angles in the lateral

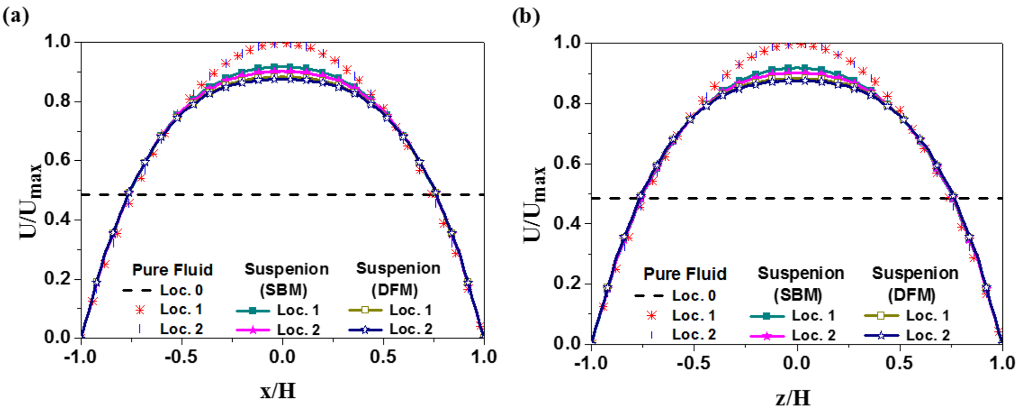

Figure 4.6: Comparison of the Newtonian fluid velocity profiles with suspension at different locations in the parent branch along (a) lateral direction, and (b) span-wise direction.

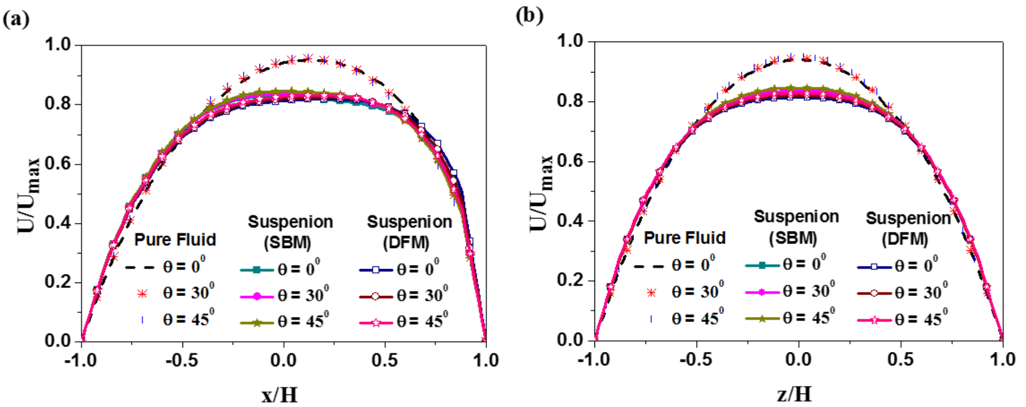

Figure 4.7: Comparison of the Newtonian fluid velocity profiles with suspension at bifurcation point (location 3) for various bifurcation angles along (a) lateral direction, and (b) span-wise direction.

(x) as well as in the span-wise (z) directions and are shown in Fig 4.6. The relative position in the lateral and span-wise direction was normalized with half width (H) of the channel. Since the Newtonian fluid becomes fully-developed so early, the velocity profiles at location 1 and 2 in the parent branch are almost similar. Whereas, in the case of suspension the coupled velocity and concentration profiles develop much more slowly and thus there is a noticeable discrepancy in the profiles at location 1 and 2. The fully-developed velocity profile (profiles at location 2) of suspension shows blunted velocity profile than that of Newtonian fluid parabolic velocity and this is true for both

DFM and SBM. Since the parent branch, we have considered in the present study has 1:1 cross-sectional aspect ratio, the lateral and span-wise velocity profiles show the same behavior.

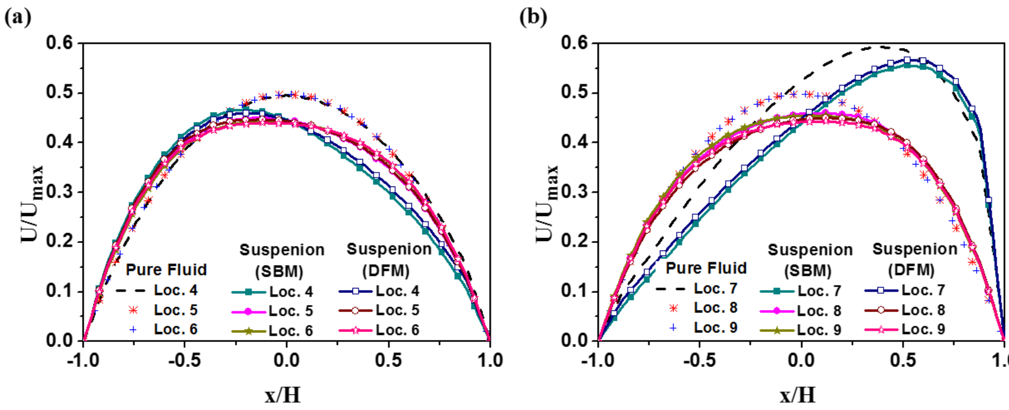

Figure 4.8: Comparison of the velocity profiles at various locations in the main branch (a), and side branch (b) along lateral direction. The bifurcation angle θ was 0^0

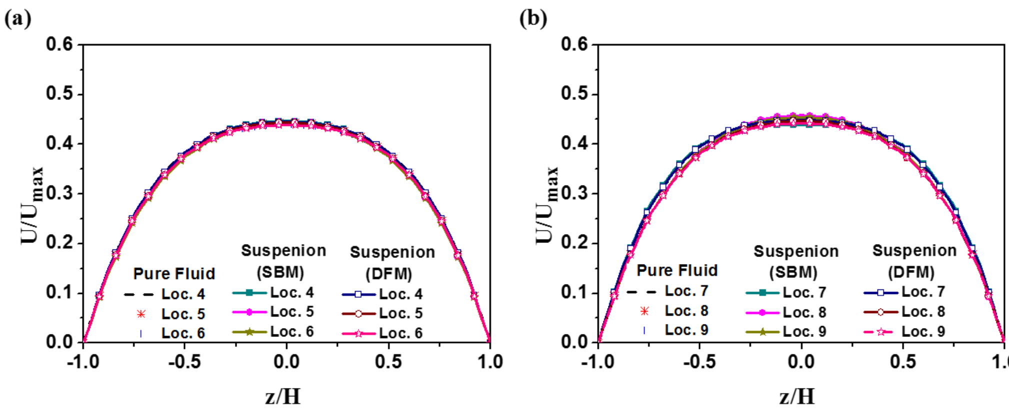

Figure 4.9: Comparison of the velocity profiles at various locations in the main branch (a), and side branch (b) along span-wise direction. The bifurcation angle θ was 0^0

The effect of bifurcation is apparent as soon as the fluid reaches the bifurcation point and this strongly depends on bifurcation angle and particle concentration. Fig. 4.7 shows the comparison of the velocity profiles at the bifurcation point (location 3) for different bifurcation angles in both lateral and span-wise direction. The divergence of the parent branch into the main branch and side branch causes the shift in lateral

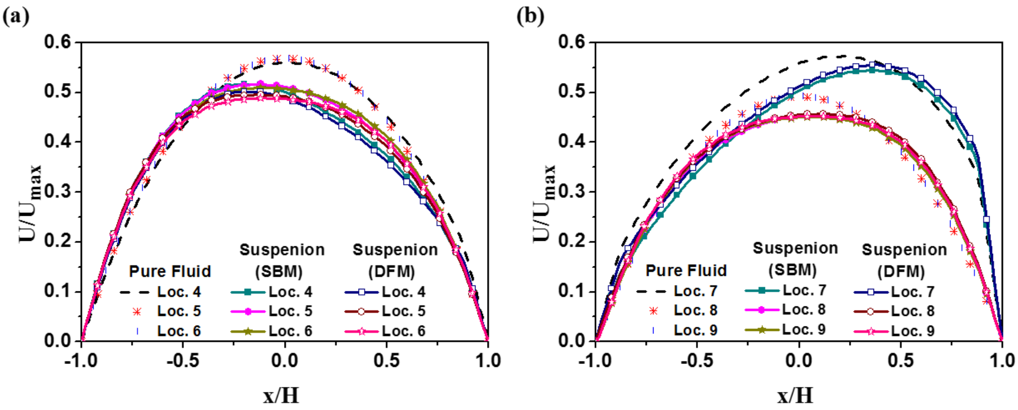

Figure 4.10: Comparison of the velocity profiles at various locations in the main branch (a), and side branch (b) along lateral direction. The bifurcation angle θ was 30^0

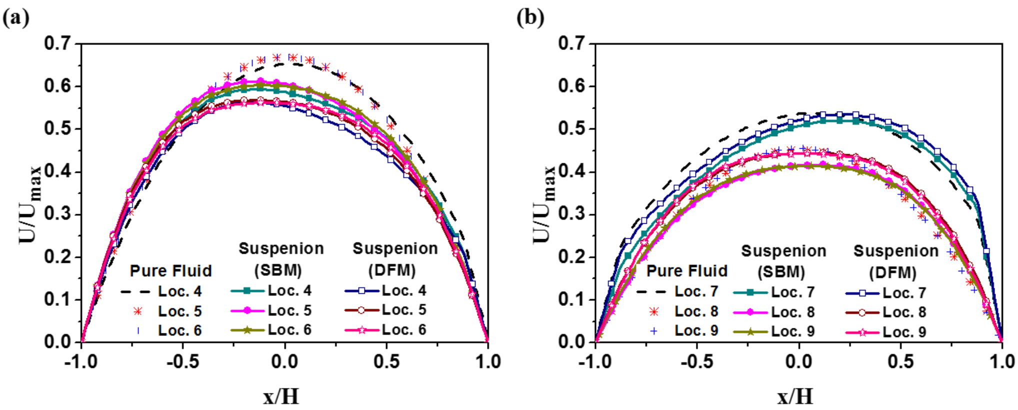

Figure 4.11: Comparison of the velocity profiles at various locations in the main branch (a), and side branch (b) along lateral direction. The bifurcation angle θ was 45^0

velocity profiles toward the side branch and the suspension shows more blunted and shifted velocity profiles than the Newtonian fluid. On the other hand, the profiles along span-wise direction are symmetric and almost has no effect of bifurcation.

The quantitative comparison of the velocity profiles in the daughter branches is shown in Figs. 4.8 and 4.9 along lateral and span-wise directions respectively in the bifurcating channel for $\theta = 0^0$. The corresponding profiles for $\theta = 30^0$ and $\theta = 45^0$ are shown in Figs. 4.10 and 4.11 respectively. Across the lateral direction, the maximum velocity in the two daughter branches skewed towards the outer walls. In all cases of θ, the degree of skewness is greatest for the side branch than the main branch. As the fluid flows towards downstream locations of the daughter branches, the flow gets stabilize and the peak in velocity profile shifts towards the channel center. However, in the span-wise direction (see Fig. 4.9), these profiles show symmetric in nature even after bifurcation and the velocity pattern is clearly carried from the parent branch to the daughter branches with the velocity peak remains at channel center-line. Due to an abrupt 90^0 turn in case of $\theta = 0^0$, the side branch has slightly larger velocity magnitude than the main branch for both suspension as well as Newtonian fluid. As the bifurcation angle increases, the main branch receives relatively high flow rate and the skewness decreases gradually.

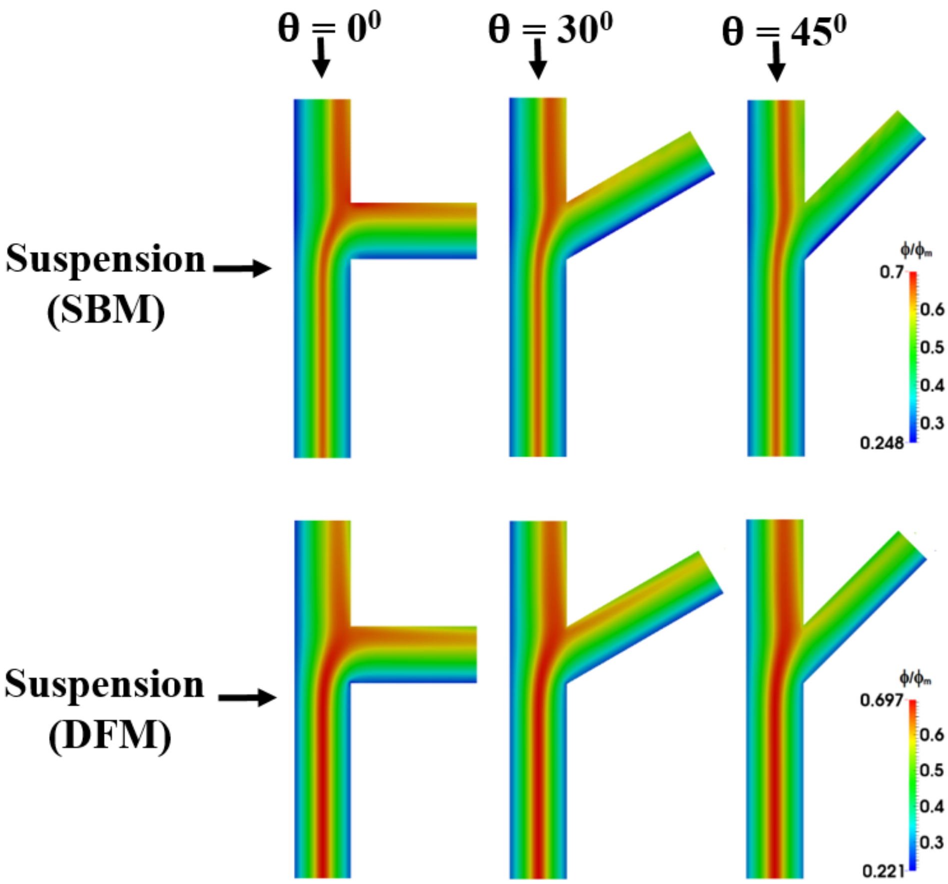

Figure 4.12: The particle concentration contour planes by using SBM and DFM in the flow direction ($x - y$ plane) for various bifurcation angles. The particle concentration was 30%.

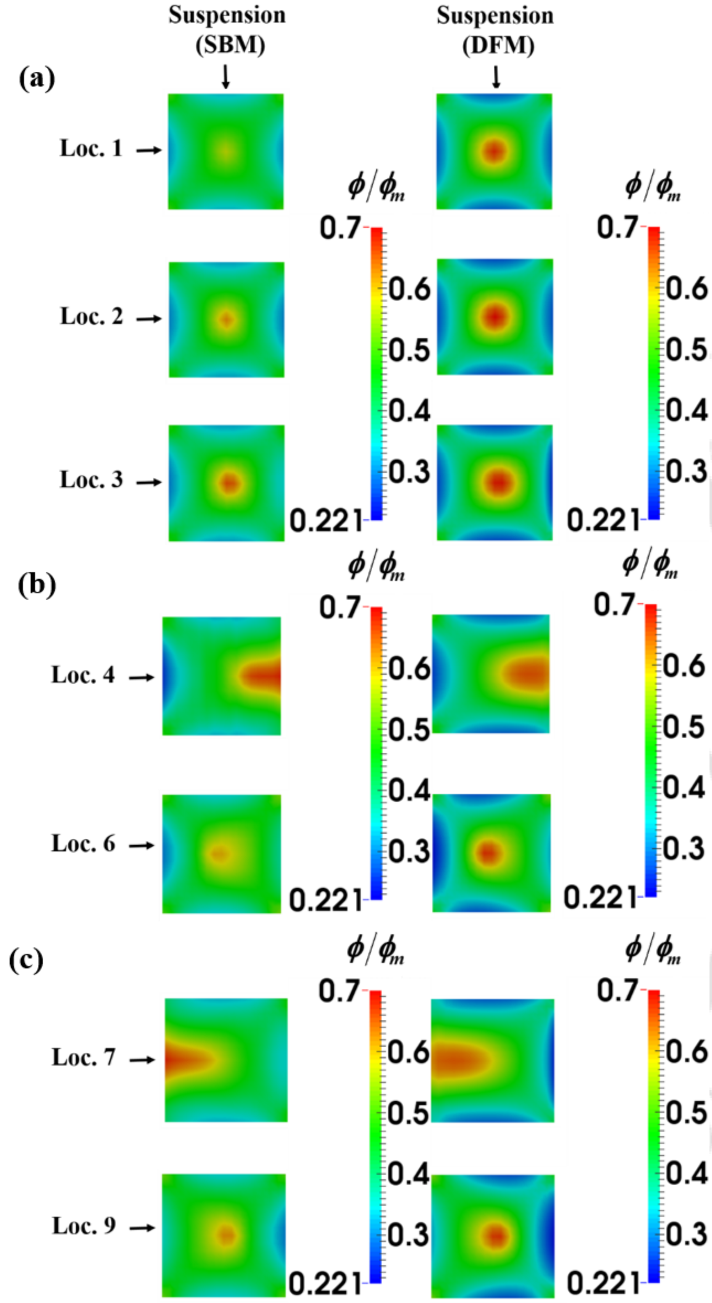

Figure 4.13: The cross-sectional contours of particle concentration at various locations in the parent branch (a), main branch (b), and side branch (c). The bifurcation angle θ was 0^0.

4.3.2 Concentration field

The contour planes of the particle volume fraction by using SBM and DFM around the bifurcation in the flow direction at mid-plane (z = 0.0009 m) for various bifurcation angles are shown in Fig. 4.12 The particle concentration was 30% and other parameters are same as in the Table 4.1. For clarity of the particle partitioning near the bifurcation region, we have not shown the full length view of the channel. The flow of the suspension in the parent branch leads to the migration of the particles towards center of the channel from the walls, forming an inhomogeneous concentration distribution of the particles. The cross-sectional view of concentration contours in the parent (Fig. 4.13a) and daughter (Figs. 4.13b & 4.13c) branches are shown in the Fig. 4.13. The parent branch shows the spatial inhomogeneity of particle volume fraction in both span-wise and lateral directions with maximum particle concentration at channel center-line. The cross-sectional particle concentration profile can be divided into particle-rich plug flow region near the channel center-line and particle-free region nearer the walls. The depletion of the particles at the corner regions is less compared to the middle portions near the walls (wall edges). This is attributed to the low shear-rate at the corners (see Fig. 4.5) than at the wall edges. The symmetric profiles persist in the upstream locations of the parent branch and become asymmetric as the suspension reaches the bifurcation point. At the bifurcation point, smearing of the profiles towards the side branch is observed and the degree of smearing is almost independent of θ unlike the velocity profile. Immediately after leaving the parent branch, the suspension diverges into the main and side branch along the dividing streamlines. The peak in the particle concentration shifted towards the inner walls and it was observed in many experimental as well as numerical simulations (Roberts and Olbricht, 2006; Xi and Shapley, 2008). Their explanation is that the suspension near the inner walls originates from the particle-rich region and for the outer walls it is originate from the particle-free region of the downstream locations of the parent branch. We observe that regions of high particle volume fraction and low velocity magnitude coincide at the upstream locations of the daughter branches. However, this profile does not persist for the full length of the channel in the downstream region. For a time after the suspension leaves the junction of the daughter branches, the layers, velocity and concentration gradients persist. Soon however, the gradients fade out; the boundary layers intermingle and disappear, and the fluid once more moves with a symmetric velocity and concentration. Both DFM and SBM predict the similar qualitative behavior of particle migration.

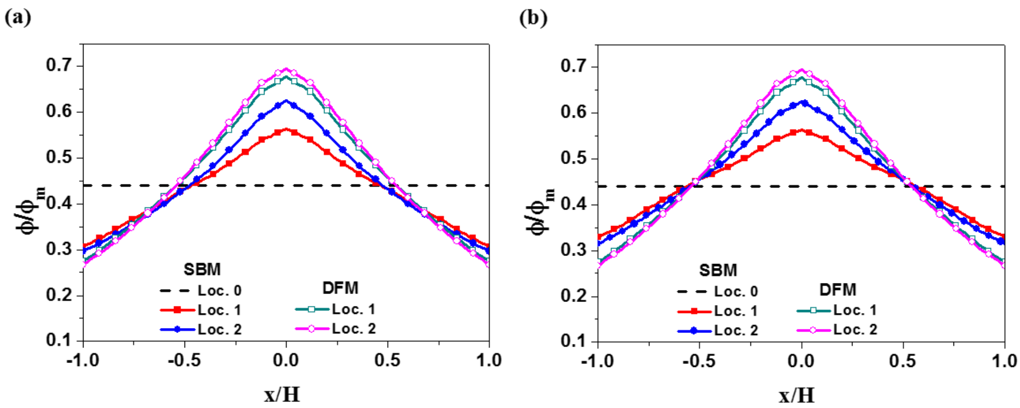

Figure 4.14: Comparison of the concentration profiles at different locations in the parent branch along lateral (a), and span-wise (b) direction.

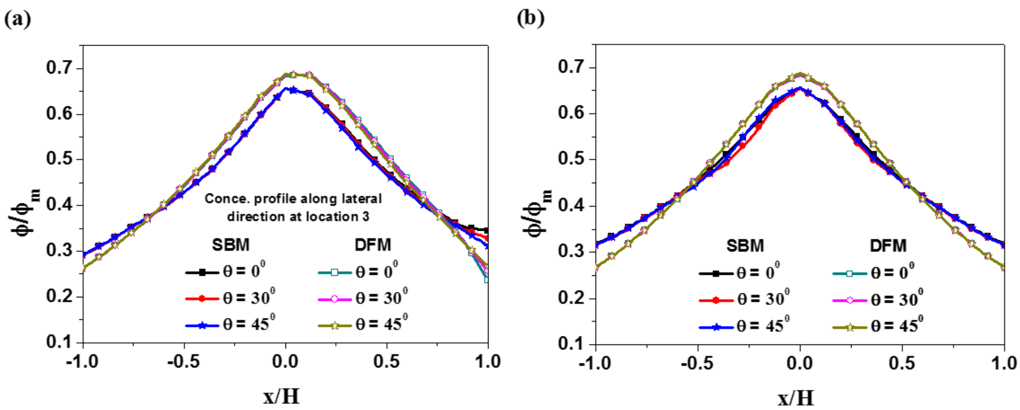

Figure 4.15: Comparison of the concentration profiles at bifurcation point (location 3) for various bifurcation angles along (a) lateral direction, and (b) span-wise direction.

In order to understand the quantitative nature of the particle distribution, we have shown the lateral and span-wise concentration profiles in the parent branch at different locations in Fig. 4.14. Likewise the velocity field, since the concentration field also does not felt the bifurcation effect in the upstream locations of the parent branch, up to location 2 the concentration profiles are common for all θ. As described earlier, the shear-induced migration phenomenon causes the initial homogeneous particle distribution at the upstream location of the parent branch becomes non-homogeneous as the suspension moves along the length of the channel. The center of the channel has maximum particle concentration. At the bifurcation point (location 3), the deceleration starts in the central core of the particles towards the side branch and thus the profile is slightly blunted in nature (Fig. 4.15). Unlike the velocity profiles, the concentration profiles are almost unaffected by the bifurcation angle. Except at bifurcation point (location 3), the lateral and span-wise concentration profiles are similar in the parent branch due to the fact that the channel we have considered has cross-sectional aspect ratio 1:1.

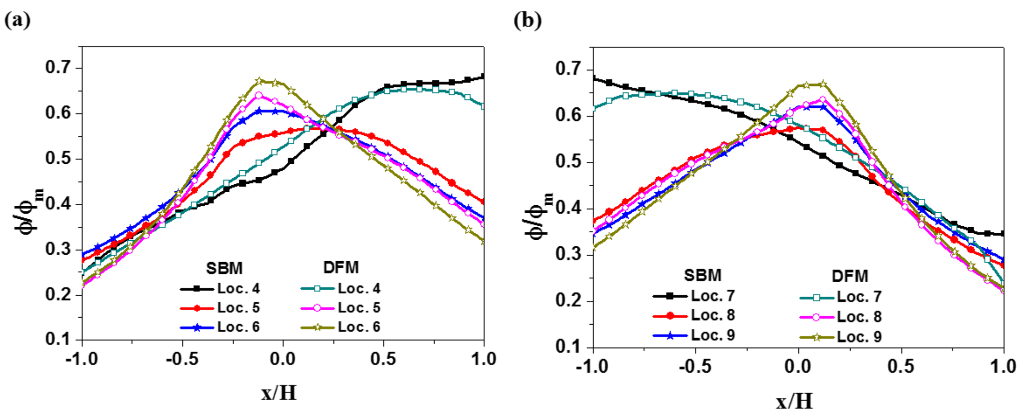

Figure 4.16: Comparison of the concentration profiles at various locations in the main branch (a), and side branch (b) along lateral direction. The bifurcation angle θ was 0^0.

Fig. 4.16 shows the lateral concentration profiles at various locations in the daughter branches for $\theta = 0^0$. The corresponding profiles in the span-wise direction are shown in Fig. 4.17. After the bifurcation asymmetry in the concentration profile formed because the central region of high concentration flows into the inner wall region of the daughter branches and the less concentrated region flows into the outer wall region. As a result,

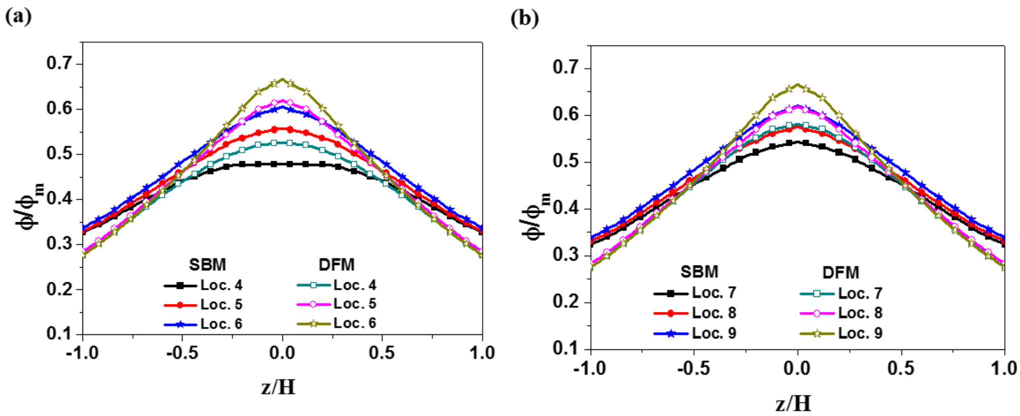

Figure 4.17: Comparison of the concentration profiles at various locations in the main branch (a), and side branch (b) along span-wise direction. The bifurcation angle θ was 0^0.

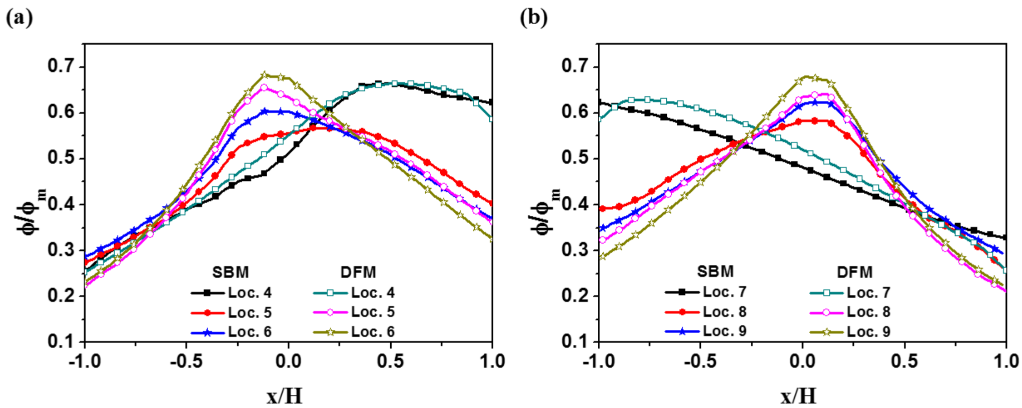

Figure 4.18: Comparison of the concentration profiles at various locations in the main branch (a), and side branch (b) along lateral direction. The bifurcation angle θ was 30^0.

the particle concentration is peaked towards the inner walls of the daughter branches. However, this profile does not persist for the full length of the channel in the downstream region. Again, because of shear-induced migration, the asymmetric post-bifurcation profiles to stabilize into symmetric profiles in the downstream locations of the daughter branches. However, in the span-wise direction, these profiles show symmetric in nature even after bifurcation and the concentration pattern is clearly carried from the parent branch to daughter branches in such a way that the concentration peak remains at channel center-line. The concentration profiles in the daughter branches corresponding

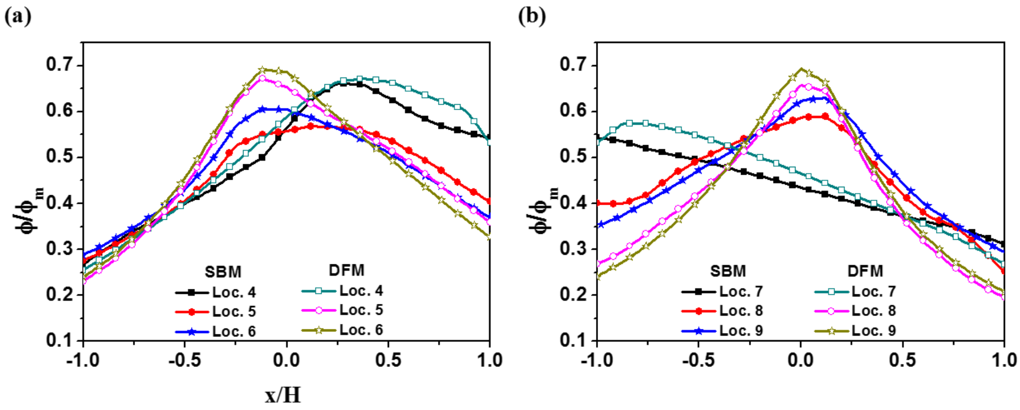

Figure 4.19: Comparison of the concentration profiles at various locations in the main branch (a), and side branch (b) along lateral direction. The bifurcation angle θ was 45^0.

to $\theta = 30^0$ and $\theta = 45^0$ are shown in Figs. 4.18 and 4.19 respectively. Similar skewed profiles were observed for the other bifurcating angles. From the Figs. 4.18 and 4.19, we can observe that the concentration peak gradually shifts towards the center with bifurcation angle.

4.3.3 Flow and particle partitioning

The knowledge of flow and particle partitioning among the daughter branches of the bifurcating channels is required in various applications. The fraction of the particles partitioned in the main branch (X_M^P) was calculated by using the following formula:

$$X_M^P = \frac{\int_{A_M} (\boldsymbol{U}\phi dA)}{\int_{A_M} (\boldsymbol{U}\phi dA) + \int_{A_S} (\boldsymbol{U}\phi dA)}, \tag{4.1}$$

where, A_M and A_S are the area of the cross-section of the main and side branch respectively.

The fluid partitioning between the daughter branches is summarized in Table 4.2. The partitioning of the suspension is different from the pure fluid partitioning. For the equal width ratio of the daughter branches ($\theta = 0^0$), the flow is partitioned almost equally for both pure fluid as well as suspension and is in good agreement with the

Table 4.2: The Fraction of the pure fluid (without particles), and bulk suspension partitioned between the daughter branches.

	Pure fluid		Suspension (SBM)		Suspension (DFM)	
Angle	Main branch	Side branch	Main branch	Side branch	Main branch	Side branch
0	0.499	0.501	0.493	0.507	0.498	0.502
30^0	0.562	0.547	0.547	0.453	0.547	0.453
45^0	0.678	0.322	0.647	0.353	0.648	0.352

Table 4.3: The Fraction of the particles partitioned between the daughter branches.

	Suspension (SBM)		Suspension (DFM)	
Angle	Main branch	Side branch	Main branch	Side branch
0	0.493	0.507	0.499	0.501
30^0	0.558	0.442	0.56	0.44
45^0	0.675	0.325	0.677	0.323

previous findings (Xi and Shapley, 2008). As θ increases, the location of the dividing streamline shifts towards the side branch. Thus, the portion of the fluid that enters into the side branch declines. The presence of the particles decreases the difference in the flow partitioning between the main and side branch. In case of dense suspension the presence of the particles modulates the velocity profiles. As we have seen earlier (Fig. 4.2), the suspension shows blunted profiles around bifurcation (location 3) and the partitioning of the suspension starts immediately when the fluid reaches the location 3. The bluntness of the profiles in the case of suspension decreases the deviation in the percentage flow partitioning between the daughter branches. The predictions of the both DFM and SBM are very similar.

The particle partitioning between the daughter branches is summarized in Table 4.3. The shear-induced particle migration causes the inhomogeneous distribution of the particles in the downstream locations of the inlet branch as described in the section 4.3.2. The peak in the particle concentration was observed at the channel center, and the regions near the walls were devoid of the particles. Since the particle-rich region divided equally at the bifurcation, the particles were partitioned equally between the daughter branches for $\theta = 0^0$. For the other cases ($\theta = 30^0$ and 45^0) particles prefer the branch which receives high flow rate. As the flow rate in the main branch increases, the particle-rich central core preferentially enters into this branch. On the other hand, the material that enters into the side branch originates from the wall regions of the inlet branch which is devoid of particles. The particle partitioning between the daughter branches does not exactly follow the bulk suspension. These results show that the width of the daughter branches influence the flow and particle partitioning.

4.4 Closure

The main theme of this chapter is to study the effect of shear-induced migration phenomenon on the velocity and particle distribution by using DFM and SBM. The particles considered in the present study was non-colloidal, mono-dispersed and neutrally buoyant in the Stokes regime. The ability of particles to form non-uniform configurations influences many aspects of suspension behavior in a bifurcation flow. The features which are greatly affected by the nonuniform distribution of the particles include the detailed concentration and velocity profiles in each branch, position of the dividing streamline, flow and particle partitioning. Subsequently, we have carried out numerical experiments to explain the aforementioned features in the oblique bifurcating channel. The suspension fluid velocity profiles showed a marked difference over pure carrier fluid velocity profiles and greatly depends on the orientation of the geometry (bifurcation angle). After the bifurcation, the velocity and concentration profiles become asymmetric and degree of asymmetry depends on the bifurcation angle. As the bifurcation angle increases, the dividing streamline shifts towards the side branch and suspension shows slightly different behavior over pure carrier fluid. The partitioning of the particles does not follow the fluid partitioning. The findings of DFM and SBM were very similar. The results which we have shown are useful in the microfluidics.

Chapter 5

Effect of carrier fluid rheology on shear-induced particle migration

5.1 Overview

The literature mentioned in chapter 1 addressed the shear-induced migration phenomenon and fluid-particle partitioning through symmetric and asymmetric bifurcating channels considering the carrier fluid as a Newtonian fluid. Within the Stokes flow regime, as long as the suspending fluid is Newtonian, the magnitude of the suspending fluid viscosity hardly affects the distribution of the particles and fluid-particle partitioning (Abbott et al., 1991). Karnis and Mason (1966) first reported the impact of the nature of suspending fluid on the particle trajectories. They have carried out experiments for a single particle in a shear-thinning fluid and observed that the particle moves towards the wall, whereas in the Newtonian fluid the migration is towards the channel center. Later, Gauthier et al. (1971) and Huang and Joseph (2000) also confirmed the findings of Karnis

Published as:

- **M.M. Reddy**, P. Tiwari and A. Singh. (2019). Effect of carrier fluid rheology on shear-induced particle migration in asymmetric T-shaped bifurcation channel. https://doi.org/10.1016/j.ijmultiphaseflow.2018.10.005.

and Mason (1966). Rao et al. (2002) through numerical simulations investigated the effect of the shear-thinning nature of the carrier fluid on the shear-induced migration of neutrally buoyant particles. Their results led them to conclude that self-diffusivity coefficients in the original model of Phillips et al. (1992) needs to be corrected for the extension to non-Newtonian carrier fluids and proposed the values for diffusivity coefficients. Later, Lam et al. (2004, 2002) through numerical simulations and experimental studies investigated the particle migration during pressure-driven tube flow of dense suspension in the shear-thinning carrier fluid. Effects of different viscosity models of carrier fluid on particle migration during non-homogeneous shear flow were investigated using the model of Phillips et al. (1992). The constant empirical parameters were arrived at by fitting the particle concentration data between experimental observations and numerical predictions. In our study, we have employed these values to study the effects of non-Newtonian carrier fluid on particle migration in asymmetric bifurcation channels. Recent studies have indicated that the particle partitioning between the daughter branches of a bifurcating channel strongly depends on the rheology of suspending fluid. D'Avino et al. (2015) found that the fluid elasticity enhances the deviations between the fluid and particle partitioning and the shear-thinning fluid does not show any significant deviation from the Newtonian case.

Most of the previous works have focused on the effect of non-Newtonian carrier fluid rheology on the motion of a single particle in bifurcating channels. The shear-induced particle migration which is important in concentrated suspensions has received much less attention in such geometries. Since the hydrodynamic interactions between the particles play an important role in the distribution of the particles, the fluid-particle partitioning between the downstream branches for concentrated suspension will not be the same as in the dilute limit. Motivated by the need to have a clear understanding of the effect of suspending fluid rheology on the shear-induced migration phenomenon and fluid-particle partitioning between the downstream branches, the study of suspension flow in a 3D asymmetric T-shaped bifurcating channel was considered in this chapter. The effect of flow rate across the daughter branches on the flow and particle partitioning was also investigated. At both the outlets, zero pressure condition was assigned and the flow rate ratio was varied by changing the cross-section area of the side branch. Both DFM and SBM can be successfully applied to the numerical simulation of suspension flow for Newtonian carrier fluids. However, the empirical parameters in the SBM for non-Newtonian carrier fluids are not known. Therefore, in this study, the DFM was employed to study the shear-induced migration in 3D asymmetric T-junction bifurcation. The suspension considered in our simulations was non-colloidal, mono-dispersed, and non-Brownian rigid particles suspended in different inelastic carrier fluids. To model the viscosity of the carrier fluid in the DFM, power-law and Bird-Carreau models were used.

5.2 Constitutive modelling

For the Newtonian carrier suspension, the bulk stress tensor $\boldsymbol{\tau}$ can be written as:

$$\boldsymbol{\tau} = 2\eta(\phi)\boldsymbol{E}. \tag{5.1}$$

For the non-Newtonian carrier suspension, the effective viscosity of the suspension is a function of particle concentration as well as local shear-rate $\dot{\gamma}$

$$\eta_{eff} = \eta(\dot{\gamma}, \phi). \tag{5.2}$$

The functional relationship of η can takes several forms that adequately fit the viscosity data for concentrated suspensions. The Krieger's correlation has been adopted here and is given by:

$$\eta_{eff} = \eta_{pure}\left(1 - \frac{\phi}{\phi_m}\right)^{-m}, \tag{5.3}$$

where η_{pure} is the viscosity of the carrier fluid, and m is the material constant.

The constitutive equations for the viscosity need to be specified to capture the suspending fluid rheology on the shear-induced migration phenomenon. The shear-rate dependent viscosity of the suspending fluid using the power-law model is:

$$\eta_{pure} = K(\dot{\gamma})^{n-1}, \tag{5.4}$$

where n and K are two empirical parameters and are known as the flow behavior index (dimensionless) and the flow consistency index (SI unit: $Pa.s^n$) respectively.

The Bird-Carreau constitutive equation is:

$$\eta_{pure} = \eta_\infty + (\eta_0 - \eta_\infty)\frac{1}{[1 + (\lambda\dot{\gamma})^2]^{\frac{1-n}{2}}}, \tag{5.5}$$

where η_0 and η_∞ are the zero-shear and infinite-shear rate viscosities respectively, and λ is the time constant.

For the non-Newtonian carrier suspension, the diffusivity constants K_c and K_η in Eqs. 2.9 and 2.10 need to be adjusted. Lam et al. (2004) investigated the particle migration in Poiseuille flow of nickel powder injection moldings. They also investigated the effects of a shear-thinning carrier fluid on particle migration by fitting the non-Newtonian power-law model. Their resulting best fit values for the parameters are: $K_c = 0.32$ and $K_\eta = 0.65$. The value of material constant, m in the Eq. 5.3 has been found to be 0.82 for the shear-thinning case, and 1.82 in the case of Newtonian carrier suspensions.

5.3 Model validation

The mathematical model was validated by comparing the numerical simulations of the pipe flow with the experimental data of Hampton et al. (1997) for Newtonian ($n = 1$), and Lam et al. (2004) for non-Newtonian ($n = 0.385$) carrier fluids. Fig. 5.1(a) shows the comparative plot of fully-developed concentration profile from CFD simulations with the experimental data of Hampton et al. (1997). The comparative plot of the concentration profile for the shear-thinning carrier fluid with the experimental data of Lam et al. (2004) is shown in Fig. 5.1(b). The power-law model was employed to calculate the carrier fluid viscosity. The concentration profiles from the numerical simulations are found to be in good agreement with the experimental results. The values of K_c and K_η are not known for shear-thickening ($n > 1$) carrier fluid. However, in order to qualitatively compare the effect of suspending fluid rheology on the particle migration, same values ($K_c = 0.41$ and $K_\eta = 0.62$) as that of Newtonian carrier fluid were considered for the shear-thickening fluid.

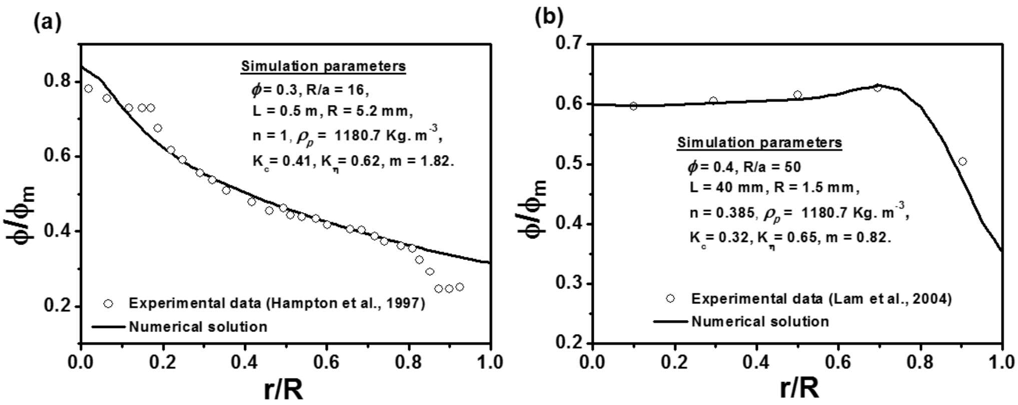

Figure 5.1: Comparison of the particle concentration profile obtained from our numerical simulations with the experimental data in a pipe flow for (a) $n = 1$, and (b) $n = 0.385$.

5.4 Problem description

The computational geometry of 3D asymmetric T-shaped bifurcating channel is shown in Fig. 5.2. The computational domain consists of an inlet branch (also termed as parent branch) which bifurcates into two orthogonal daughter branches. The daughter branch having the same axis of symmetry as that of the inlet is termed as the main branch and the other branch having the axis of symmetry orthogonal to that of the inlet is

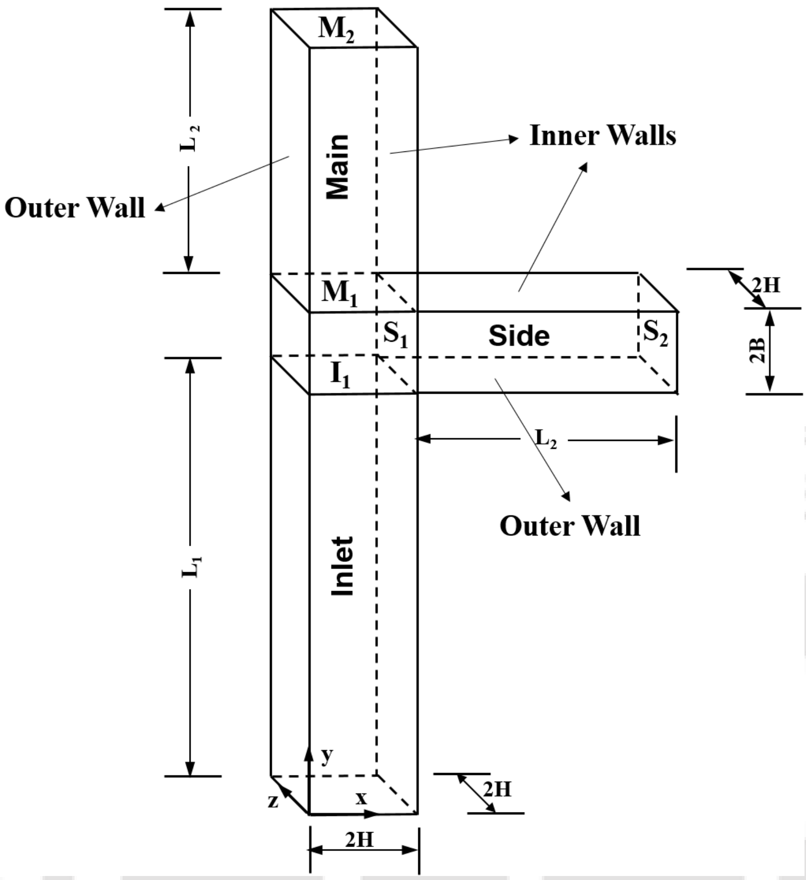

Figure 5.2: Schematic diagram of the computational geometry.

Table 5.1: Geometry details and simulation parameters.

S.No	Parameter	Symbol[Unit]	Value
1	Width of the channel	$2H$ [m]	0.0018
2	Flow consistency index	K [Pa.s^n]	1
3	Fluid density	ρ [kg.m^{-3}]	1190
4	Particle radius	a [μm]	50
5	Zero-shear viscosity	η_o [Pa.s]	1
6	Infinite-shear viscosity	η_∞ [Pa.s]	0.1
7	Time constant	λ [s]	1
8	Average inlet velocity	U [m.s^{-1}]	0.0063
9	Average inlet concentration	ϕ	0.3

termed as the side branch. The minimum length required for the fully-developed flow for different sections were calculated based on the formula proposed by Nott and Brady

(1994) (Eq. 3.5). The particle radius (a) was taken as 50 μm. The length of the inlet branch was L_1 (0.5 m), whereas the two daughter branches have the same length L_2 (0.15 m). Both the inlet and main branch have the square cross-section with half width of the channel equal to 0.0009 m. The side branch has a rectangular cross-section with half-width $H = 0.0009$ m. The depth ($2B$) was varied in the simulations in order to achieve different volumetric flow rates in the daughter branches. Five bifurcating channels with a depth ratio (H/B) of 1, 1.25, 1.5, 1.75, and 2 were considered. In the inlet branch, the local coordinates x, y, and z denote lateral, flow, and span-wise directions respectively. For the quantitative comparison purpose, the velocity and concentration profiles are drawn at different locations in the bifurcating channel. In order to match the Reynolds number (Re) when n was varied, the viscosity of a typical shear-rate requires appropriate adjustments as reported by Matos and Oliveira (2013). However, our simulations were carried out in the Stokes regime ($Re \ll 1$) and the concentration profiles are found to be independent of the magnitude of the viscosity (see section 5.5.2); the same magnitude of the inlet velocity (0.0063 m/s) was considered for all n values. The geometry details and simulation parameters are summarized in Table 5.1.

5.5 Results and discussion

5.5.1 Velocity field

The simulations in the straight channel without bifurcation having the same dimensions as that of the inlet branch were carried out. To study the impact of the particle phase on the velocity field, simulations were also carried out for the pure carrier fluid. The power-law constitutive model was used to calculate the apparent viscosity of the carrier fluid. The comparison of fully-developed cross-sectional velocity contours for the carrier fluid and suspension in the straight channel is shown in Fig. 5.3 for a range of n values. The scales of velocity magnitudes of suspension were normalized with that of

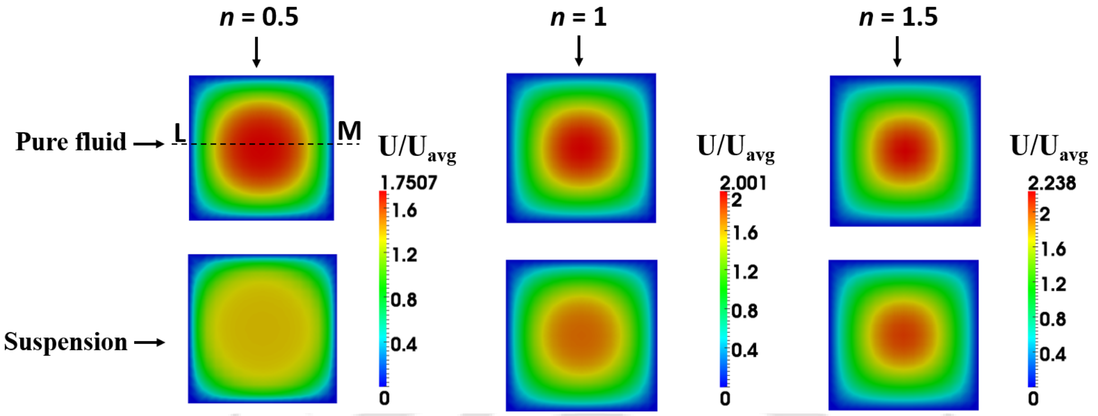

Figure 5.3: Fully-developed cross-sectional velocity contours for carrier fluid and suspension in the straight channel.

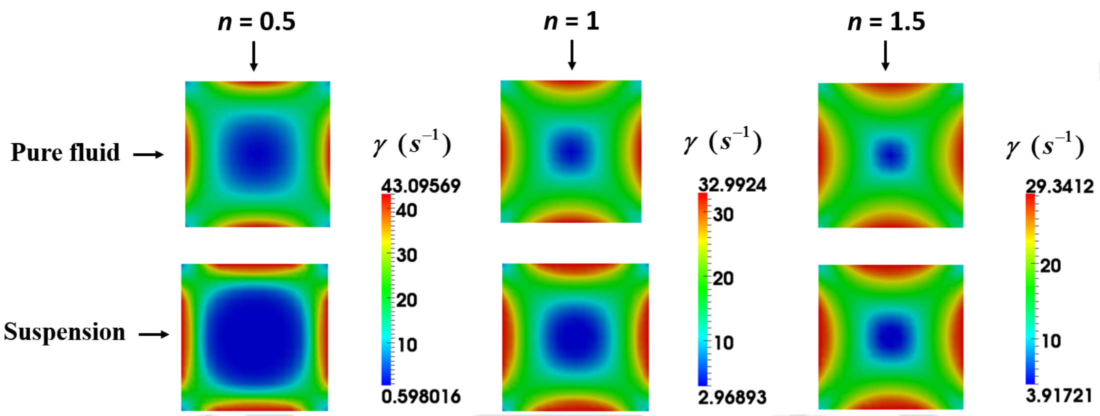

Figure 5.4: Fully-developed cross-sectional shear-rate contours for carrier fluid and suspension in the straight channel.

corresponding carrier fluid. The corresponding shear-rate contours are shown in Fig. 5.4. For the validation purpose of the numerical results, simulations were carried for the carrier fluid in a 2D straight channel and compared with the fully-developed analytical solution (Chhabra and Richardson, 1999) of power-law fluid (Fig. 5.5a). The velocity profiles in the 3D straight channel along the mid-plane are shown in the Fig. 5.5(b). The non-Newtonian behavior alters the parabolic velocity profile observed in the case of the Newtonian fluid. A blunted velocity profile was observed for the shear-thinning fluid ($n = 0.5$), and a much sharper profile was observed in the case of shear-thickening

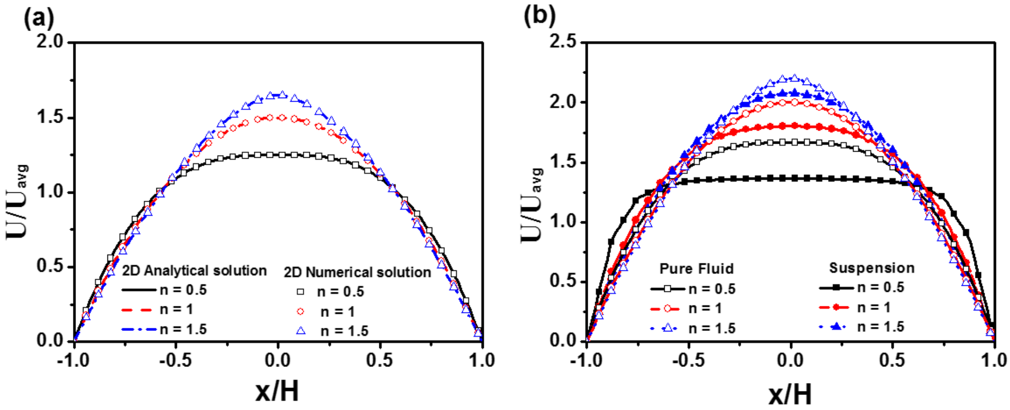

Figure 5.5: (a) Comparison of the fully-developed 2D analytical solution (pure fluid) with the 2D numerical solution, (b) Mid-plane velocity profiles for pure fluid and suspension in a 3D straight channel.

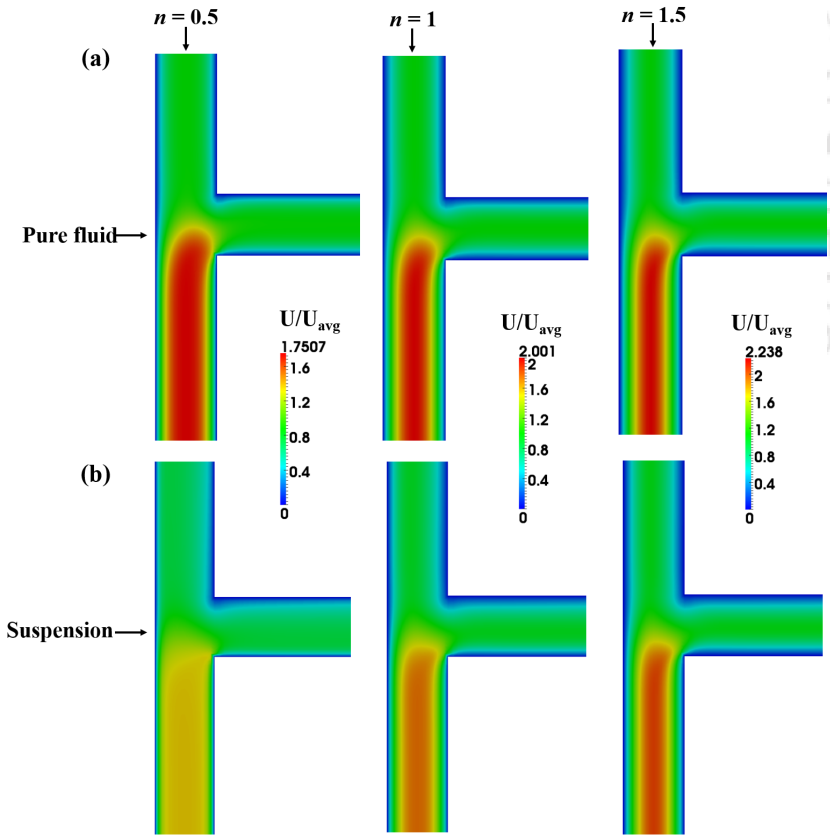

Figure 5.6: The front view ($x-y$ plane) velocity contour planes for (a) pure fluid, and (b) suspension in the bifurcating channel at mid-plane ($z = H$) for three different n values. The depth ratio (H/B) of the daughter branches was 1.

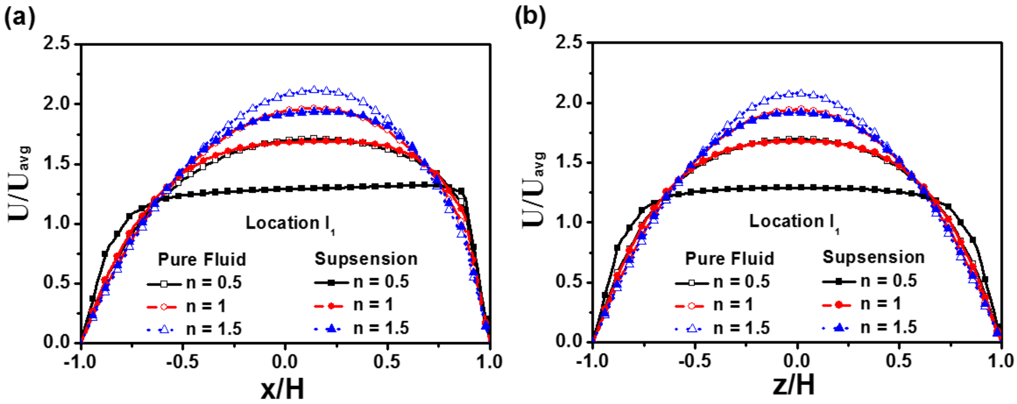

Figure 5.7: Comparison of mid-plane velocity profiles for the pure fluid and suspension at bifurcation point (location I_1) in the (a) lateral direction, and (b) span-wise direction for various n values ($n = 0.5$, 1, and 1.5). The depth ratio (H/B) of the daughter branches was 1.

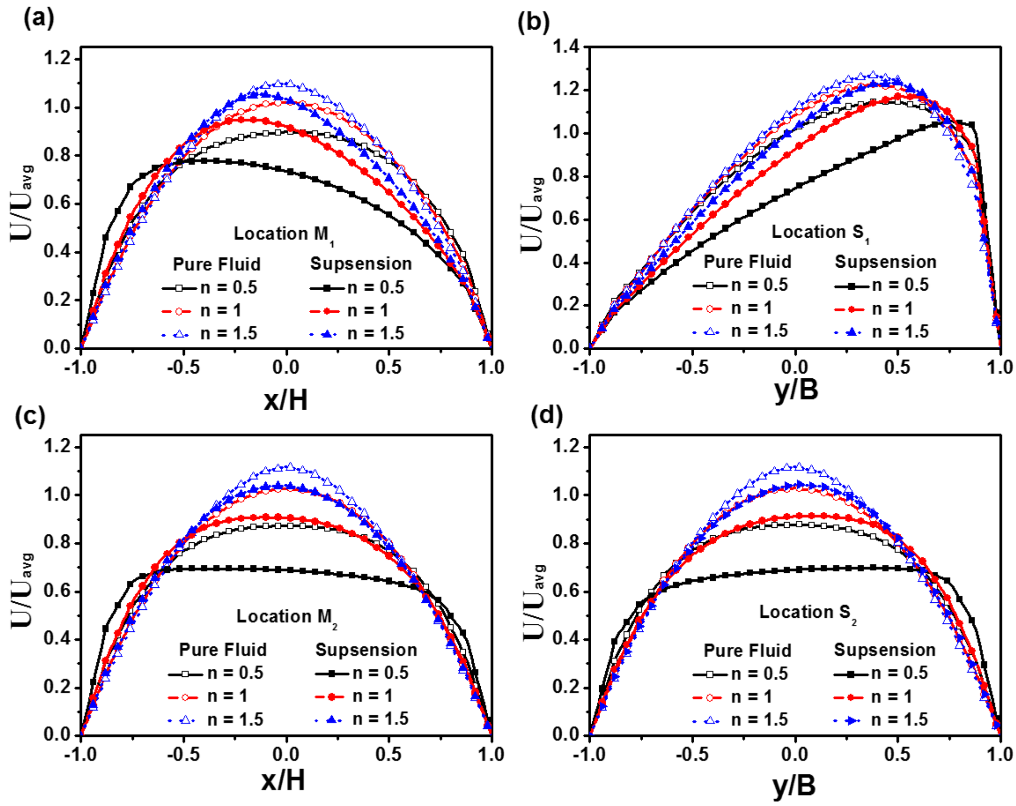

Figure 5.8: Comparison of mid-plane velocity profiles for the pure fluid and suspension along the lateral direction at (a) location M_1, (b) location S_1, (c) location M_2, and (d) location S_2 for various n values. The depth ratio (H/B) of the daughter branches was 1.

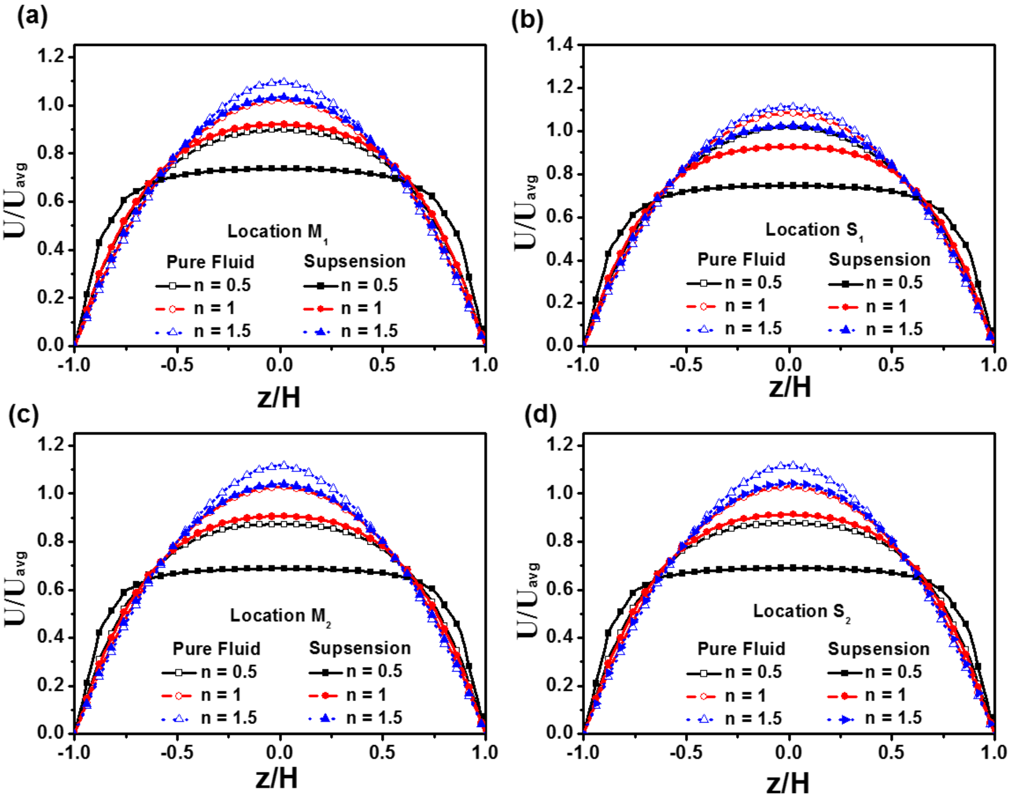

Figure 5.9: Comparison of mid-plane velocity profiles for the pure fluid and suspension along the span-wise direction at (a) location M_1, (b) location S_1, (c) location M_2, and (d) location S_2 for various n values. The depth ratio (H/B) of the daughter branches was 1.

fluid ($n = 1.5$). A marked difference between the velocity profiles of carrier fluid and the corresponding suspension can be found. The presence of the particles and their redistribution flatten the velocity profile around the center-line of the channel (Averbakh et al., 1997; Karnis et al., 1966; Koh et al., 1994). The degree of the bluntness strongly depends on the rheology of the carrier fluid. The bluntness in the case of shear-thinning suspension was very high and gradually decreased with n. The high shear-rate was observed near the walls and low at the center core of the channel in all types of fluids. However, the corners of the channel have relatively lower shear-rates compared to the middle regions near the wall and this has an influence on the distribution of the particles near the corners. The shear-thinning nature decreases the viscosity and increases the shear-rate at the walls, which amplifies the particle migration.

Further simulations were carried out for the suspension flow in the 3D asymmetric T-shaped bifurcating channel. Fig. 5.6 shows the comparison of the front view ($x-y$ plane) velocity contours for carrier fluid and suspension at mid-plane ($z = H$). The depth ratio (H/B) of the daughter branches was 1. Due to the high aspect ratio of the channel the full channel is not shown, and for clarity purpose, these contours were drawn around the bifurcation junction only. The smearing of the flow towards the side branch at bifurcation section (location I_1) was relatively high for suspension compared to the pure carrier fluid. The presence of the particles in suspension causes the early smearing of the velocity profile. Fig. 5.7 shows the comparison of velocity profiles for carrier fluid and suspension at location I_1 along the lateral and span-wise directions. The suspension shows relatively more skewed profiles towards the side branch along the lateral direction. However, the profiles along the span-wise direction are nearly symmetric. One more interesting observation is that suspension in a Newtonian carrier behaves like a pure shear-thinning fluid and the suspension in shear-thickening carrier fluid behaves like a pure Newtonian fluid.

The comparison of mid-plane lateral and span-wise direction velocity profiles in the daughter branches are shown in Figs. 5.8 and 5.9 respectively for the bifurcating channel having the width ratio $H/B = 1$. Across the lateral direction, the maximum velocity in both the daughter branches was skewed towards the outer walls. The degree of skewness strongly depends on the rheology of the carrier fluid. Moreover, in all cases concentrated suspension exhibits more skewed profile compared to the pure fluid. The side branch has more skewed profile than the main branch for both suspension as well as pure fluid, and an abrupt 90^0 turn in the case of side branch is responsible for it. As the fluid flows towards downstream locations (locations M_2 and S_2) of the daughter branches, the peak in velocity profile again shifts towards the channel center. The span-wise direction profiles (Fig. 5.9) were symmetric in nature even after bifurcation and the velocity pattern clearly carried from the parent branch to the daughter branches with the peak at channel center. As the value of H/B increases, the flow rate through the main branch increases with similar skewed profiles (not shown here).

5.5.2 Concentration field

Fig. 5.10 shows the comparison of fully-developed cross-sectional particle concentration contours for various n values (n = 0.5, 1, and 1.5) in the straight channel. The corresponding profiles along the line $L-M$ (cutting through the mid-plane of the channel) are shown in Fig. 5.11(a). Migration of the particles from high shear-rate to the low shear-rate region led to an inhomogeneous distribution of the particles. The fully-developed particle concentration profiles showed the spatial inhomogeneity in both span-wise and lateral directions with maximum particle concentration at the center. The cross-sectional particle concentration profiles can be divided into particle-rich plug flow region around the channel center and the particle-free region near the walls. The regions of high particle concentration coincide with the regions of low shear-rate magnitude. Since the shear-rate at the walls in the case of shear-thinning fluid is relatively high (see Fig. 5.4), larger migration flux is expected there. Therefore, the thickness of the particle-rich central core is larger (with a very low concentration near the walls) for the shear-thinning case. This particle-rich central core decreases with flow behavior index (n), and therefore, the particle concentration at the walls increases. The particle concentration at the corners of the channel was high compared to the middle regions near the walls, and the low shear-rate at the corners is responsible for it (see Fig. 5.4). In the Fig. 5.11(b) we have shown the central-line concentration profiles along the length of the channel. Due to the shear-induced migration, the center-line concentration gradually increases and at some location fully-developed profile was achieved. This confirms that the length of the inlet branch was sufficient enough for the fully-developed flow. The simulations were also carried out to study the impact of the flow consistency index (K) on the particle migration. The comparison of the fully-developed concentration profiles in the straight channel for two different K values is shown in Fig. 5.11(a). It was found that the magnitude of the flow consistency index K has no effect on the fully-developed profiles.

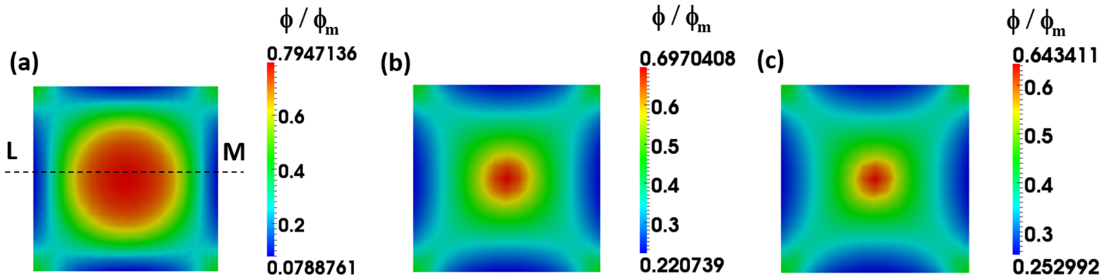

Figure 5.10: Fully-developed cross-sectional particle concentration contours in the straight channel for (a) $n = 0.5$, (b) $n = 1$, and (c) $n = 1.5$.

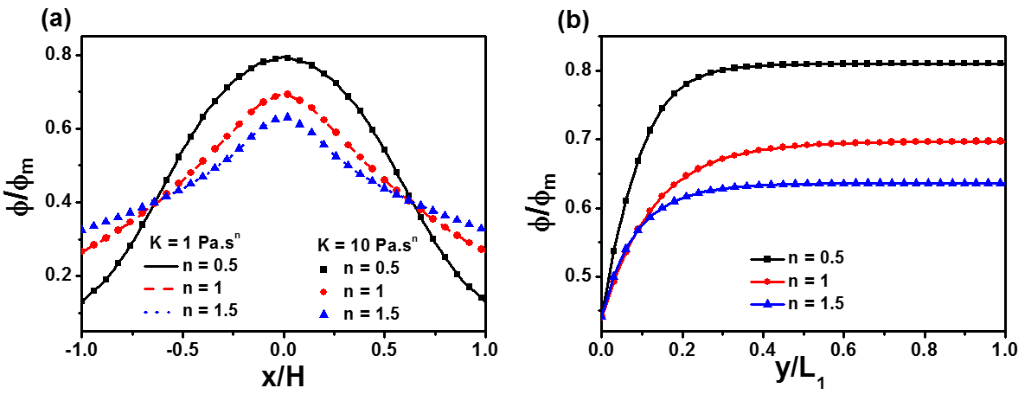

Figure 5.11: Fully-developed mid-plane (along $L - M$) concentration profiles (a), and centerline concentration profiles in the straight channel (b) for various n values.

Karnis and Mason (1966) observed that a particle released near the wall of a pipe carrying shear-thinning fluid migrates towards the center and settles to a position where the velocity/shear-rate profile becomes flat (i.e. between channel center and the wall of the channel). The dynamics of single particle has bearing on the concentration profiles of dense suspension (Fig. 5.11a), which showed inverted V shape profile for suspension in the Newtonian and shear-thickening carrier, but a relatively flat profile in the shear-thinning carrier. To understand the relationship between the shear-rate gradient and the

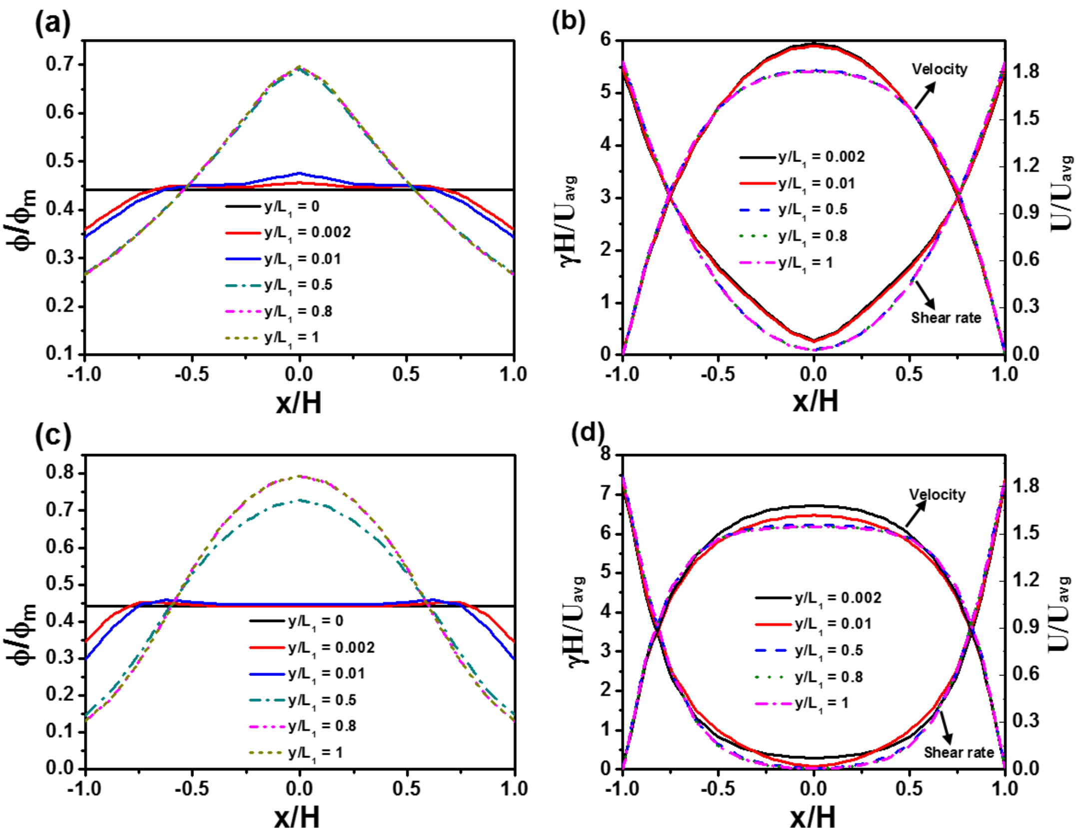

Figure 5.12: Development of particle concentration profiles (a), shear-rate and velocity profiles (b) for Newtonian suspension flowing through the straight channel. The corresponding profiles for shear-thinning suspension ($n = 0.5$) are shown in (c) and (d) respectively.

resulting migration flux, the evolution of velocity and concentration profiles were plotted at various locations along the length of the channel (Fig. 5.12). The concentration profiles at various positions in the case of Newtonian suspension are shown in Fig. 5.12(a), and the corresponding velocity and shear-rate profiles are shown in Fig. 5.12(b). The flat velocity profile at the inlet of the channel quickly becomes parabolic. A large gradient in the shear-rate causes depletion of the particles near the wall. Initially, the rise in the concentration of particles in the center was weak but later in this region, the migration flux was stronger compared to the wall regions. None the less, the peak value of concentration was always at the center of the channel. This is not the case with the shear-thinning suspension whose concentration and velocity profiles at various locations

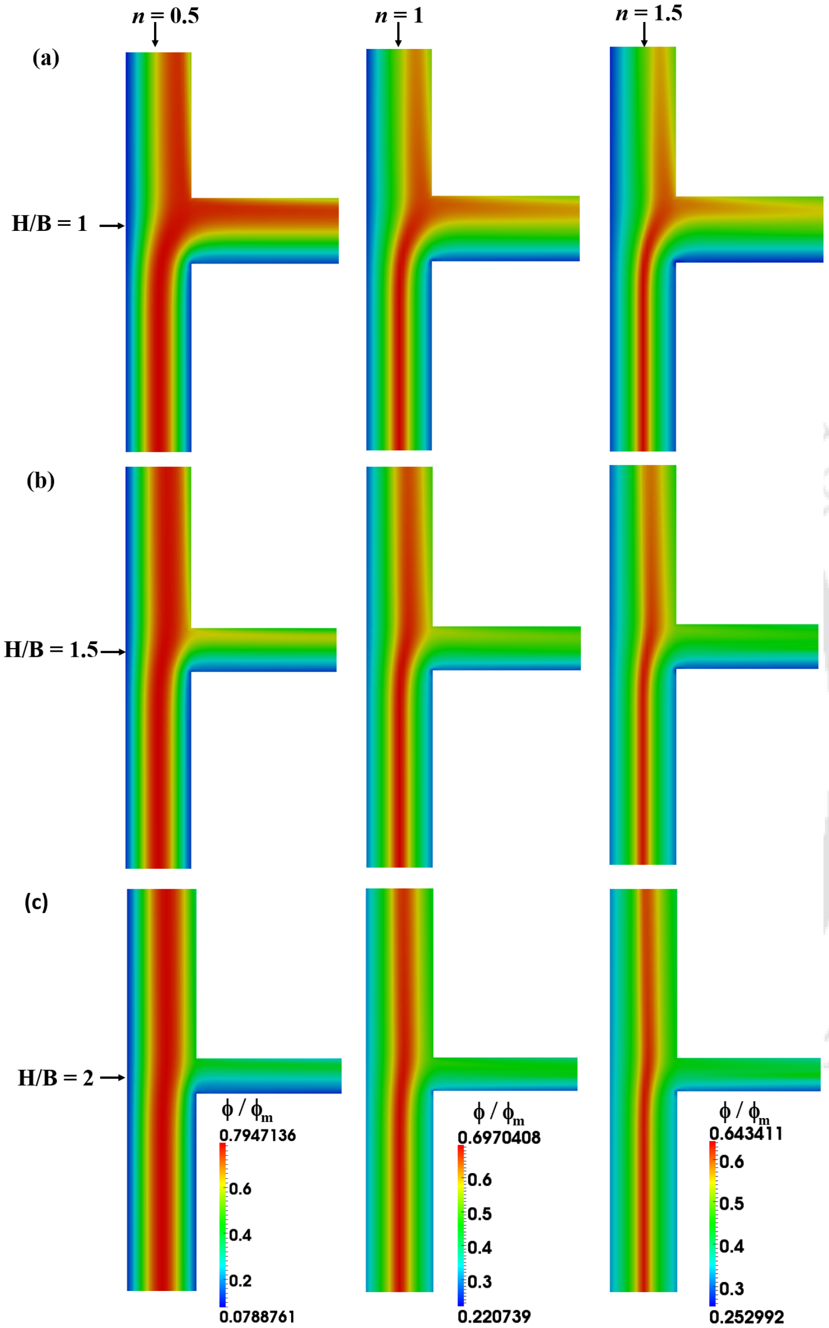

Figure 5.13: The front view ($x - y$ plane) particle concentration contour planes in the bifurcating channel for (a) $H/B = 1$, (b) $H/B = 1.5$, and (c) $H/B = 2$ at mid-plane ($z = H$) three different n values.

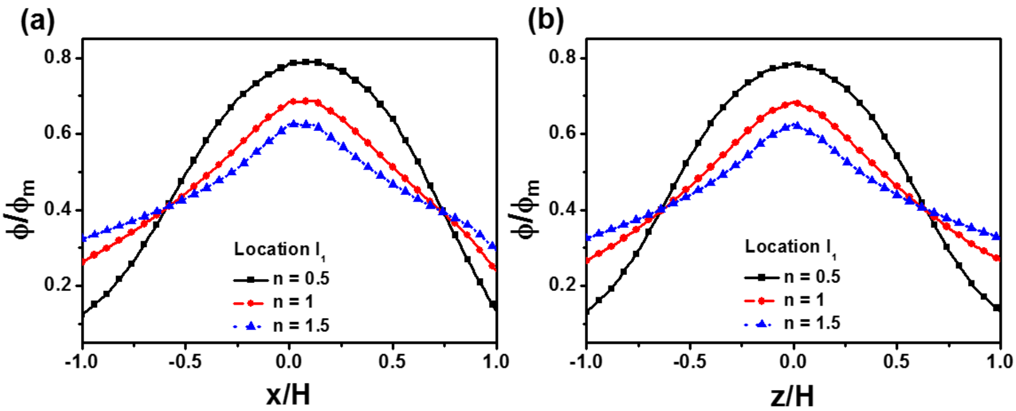

Figure 5.14: Comparison of mid-plane concentration profiles at location I_1 in the (a) lateral direction, and (b) span-wise direction for various n values ($n = 0.5$, 1, and 1.5). The value of (H/B) was 1.

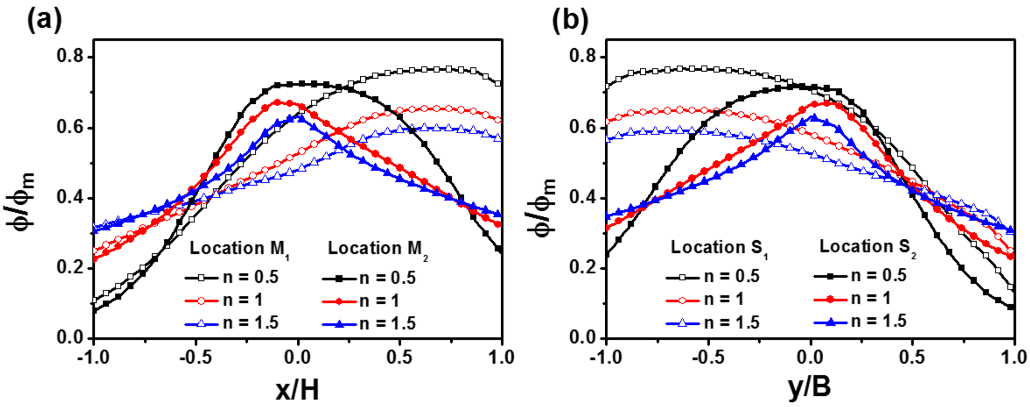

Figure 5.15: Comparison of mid-plane concentration profiles along lateral direction at different locations in the main branch (a) and side branch (b) for various carrier fluids. The value of H/B was 1.

are shown in Fig. 5.12(c) and 5.12(d) respectively. The velocity profile was very much flat in the region $-0.5 < x/H < 0.5$, and the corresponding shear-rate values were nearly zero. The concentration profiles at the locations close to the entrance of the channel showed a peak-valley-peak pattern (Fig. 5.12c). The sharp gradient in the shear-rate near the wall causes stronger particle flux which is larger compared to the opposite flux arising due to the gradient in concentration. The locations of these peaks coincide with the positions at which the shear-rate profiles become nearly flat. The large shear-rate

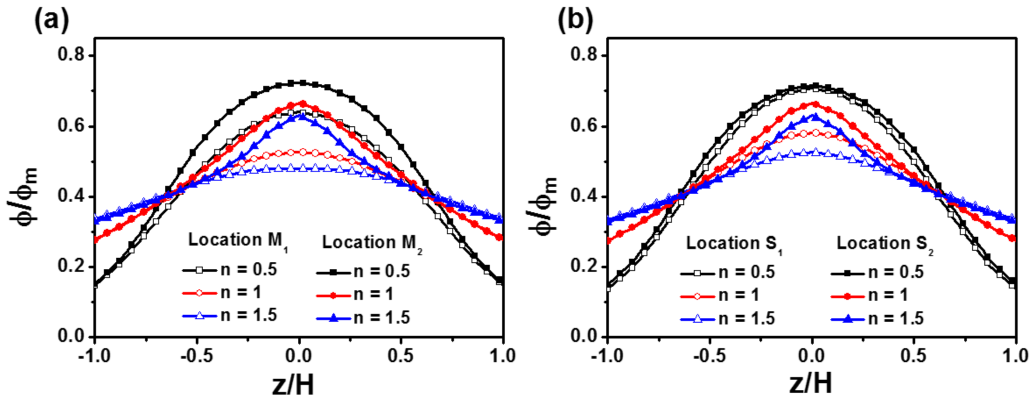

Figure 5.16: Comparison of mid-plane concentration profiles along span-wise direction at different locations in the main branch (a) and side branch (b) for various carrier fluids. The value of H/B was 1.

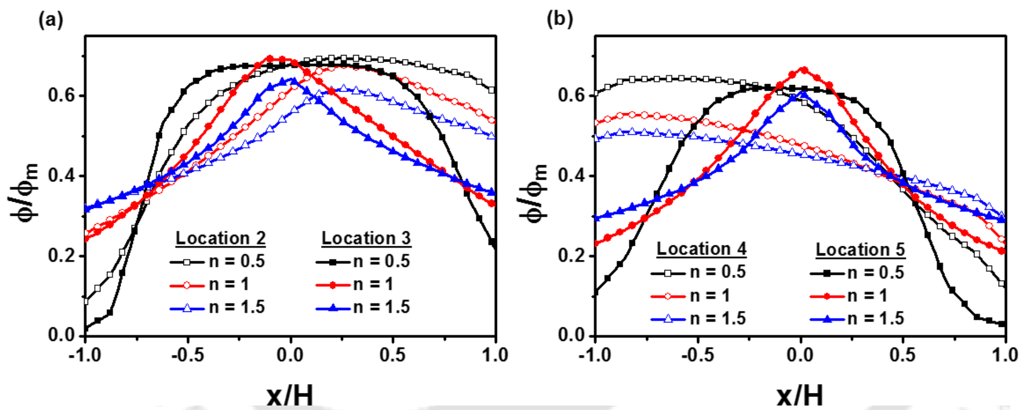

Figure 5.17: Comparison of mid-plane concentration profiles along lateral direction at different locations in the main branch (a) and side branch (b) for various carrier fluids. The value of H/B was 1.5.

gradient near the wall causes a further decrease in the concentration there and a gradual increase in the concentration in the middle regions. As a consequence, the two peaks near the wall disappear and gradually the concentration profile develops in the form of inverted U shape. Lam et al. (2004, 2002) also observed similar behavior in the case of shear-thinning carrier suspension flow in a straight pipe. In their experimental study the length of the pipe was very small (L = 40 mm) and hence, the concentration peak was observed near the wall (Fig. 5.1b). However, for the fully-developed simulation, our

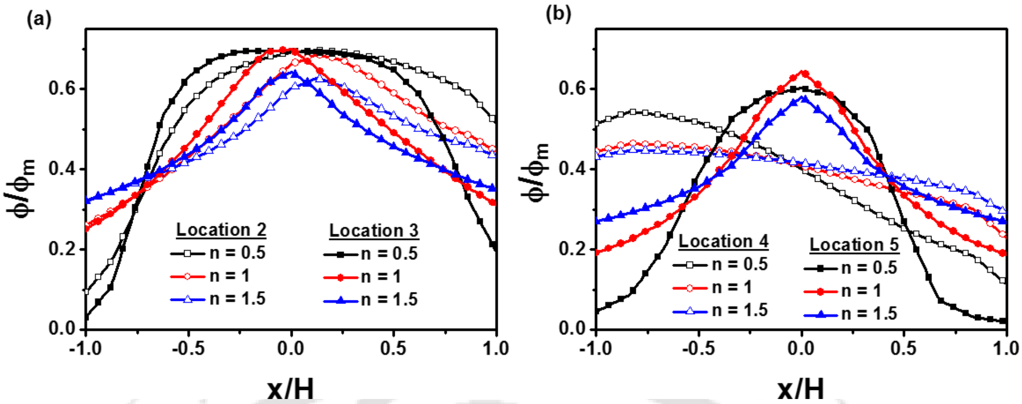

Figure 5.18: Comparison of mid-plane concentration profiles along lateral direction at different locations in the main branch (a) and side branch (b) for various carrier fluids. The value of H/B was 2.

results show that the peak gradually shifts towards the channel center.

Following the simulations in the straight channel, the migration in bifurcating channels was studied. The particle concentration contours (in the $x-y$ plane) at the mid-plane ($z = H$) around the bifurcation for various n and H/B are shown in Fig. 5.13. The symmetric profiles persist in the upstream locations of the inlet branch and become slightly asymmetric as the suspension reaches the bifurcation section (location I_1). This can be seen more clearly in Fig. 5.14(a) which shows the comparison of lateral direction concentration profiles at this location. Slight smearing of the profiles towards the side branch is observed in the lateral direction as the flow reaches the bifurcation. On the other hand, symmetric profiles are observed in the span-wise direction (Fig. 5.14b). Immediately after leaving the parent branch, the suspension diverges into the main and side branch. The peak in the particle concentration shifts towards the inner walls and this has also been observed in many experimental studies and numerical simulations (Reddy and Singh, 2014; Roberts and Olbricht, 2006; Xi and Shapley, 2008; Yadav et al., 2015). This is due to the fact that the particles near the inner walls of the daughter branches arrive from the particle-rich central core of the inlet branch, whereas, the outer walls receive particles coming from the low concentration regions (near the channel walls) of the

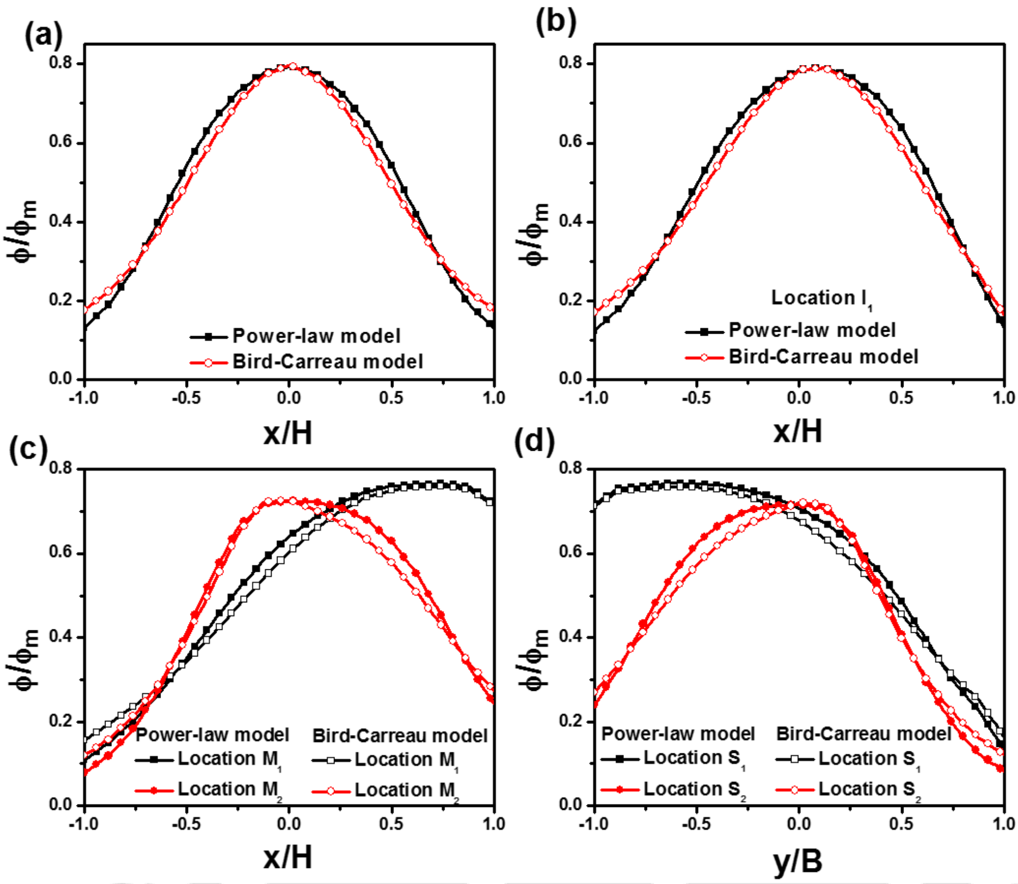

Figure 5.19: Comparison of mid-plane concentration profiles in the lateral direction for power-law and Bird-Carreau model: (a) fully-developed profile in the straight channel (b) profiles in the inlet section of bifurcating channel at the location I_1, (c) profiles at different locations in the main branch, and (d) profiles at different locations in the side branch. The flow rate in the main and side branch was equal ($H/B = 1$), and the flow behavior index (n) was 0.5.

inlet branch. The corresponding lateral concentration profiles at various locations in the daughter branches are shown in Fig. 5.15. The regions of high particle volume fraction and low-velocity magnitude coincide at the upstream locations of the daughter branches. For the lateral directions, the highly asymmetric profiles of the main branch (Fig. 5.15a) and the side branch (Fig. 5.15b) near the bifurcation gradually become more symmetric at the downstream locations. The trends for different carrier fluids are similar. Again the shear-induced migration phenomenon causes the asymmetric post-bifurcation profiles to stabilize into symmetric profiles in the downstream locations of the daughter branches. However, in the span-wise direction, these profiles in the main and side branch remain the same throughout, and the concentration peak is always at the center (Fig. 5.16). The peak concentration at the inner walls is high for the shear-thinning suspension and low for the shear-thickening when compared with the Newtonian suspension. The concentration profiles along the lateral direction in the daughter branches corresponding to $H/B = 1.5$ and 2 are shown in Figs. 5.17 and 5.18 respectively. The profiles show similar skewed profiles with the peak in the main branch gradually shifts towards the center with H/B. As the flow rate in the main branch increases, more and more particles enter into this branch. For the case of $H/B = 2$, nearly the entire particle-rich central core enters into the main branch.

We have compared the concentration profiles obtained by using two different constitutive models of the carrier fluid: power-law model and Bird-Carreau model. The parameters for both the constitutive models are shown in the Table 5.1. The simulations were carried out for the case of $H/B = 1$, and flow behavior index, $n = 0.5$. The fully-developed concentration profiles were compared by carrying out simulations in the straight channel (without bifurcation) having the same dimensions as that of the inlet branch (Fig. 5.19a). The corresponding comparisons for the bifurcating channel at different locations are shown in the Figs. 5.19(b)-(d). The predictions of the concentration profile for the two constitutive models are very similar.

5.5.3 Flow and particle partitioning

The knowledge of flow and particle partitioning among the daughter branches of the bifurcating channels is required in various applications. The fraction of the particles partitioned in the main branch (X_M^P) was calculated by using the following formula:

$$X_M^P = \frac{\int_{A_M} (\boldsymbol{U} \phi dA)}{\int_{A_M} (\boldsymbol{U} \phi dA) + \int_{A_S} (\boldsymbol{U} \phi dA)}, \tag{5.6}$$

Table 5.2: The Fraction of pure fluid (without particles), bulk suspension and particles partitioned between the daughter branches.

	H/B	n = 0.5		n = 1		n = 1.5	
		Main branch	Side branch	Main branch	Side branch	Main branch	Side branch
Pure Fluid Partitioning (without particles)	1	0.498	0.502	0.499	0.501	0.499	0.501
	1.25	0.643	0.357	0.623	0.377	0.608	0.392
	1.5	0.751	0.249	0.706	0.294	0.69	0.31
	1.75	0.826	0.174	0.775	0.225	0.755	0.245
	2	0.879	0.121	0.829	0.171	0.808	0.192
Bulk suspension Partitioning (ϕ = 0.3)	1	0.499	0.501	0.499	0.501	0.499	0.501
	1.25	0.608	0.392	0.593	0.407	0.595	0.405
	1.5	0.715	0.285	0.674	0.326	0.676	0.324
	1.75	0.792	0.208	0.741	0.259	0.74	0.26
	2	0.845	0.155	0.795	0.205	0.791	0.209
Particle Partitioning	1	0.502	0.498	0.5	0.5	0.5	0.5
	1.25	0.642	0.358	0.61	0.39	0.606	0.394
	1.5	0.77	0.23	0.7	0.3	0.691	0.309
	1.75	0.85	0.15	0.77	0.23	0.757	0.243
	2	0.898	0.102	0.823	0.177	0.808	0.192

where, A_M and A_S are the area of the cross-section of the main and side branch respectively.

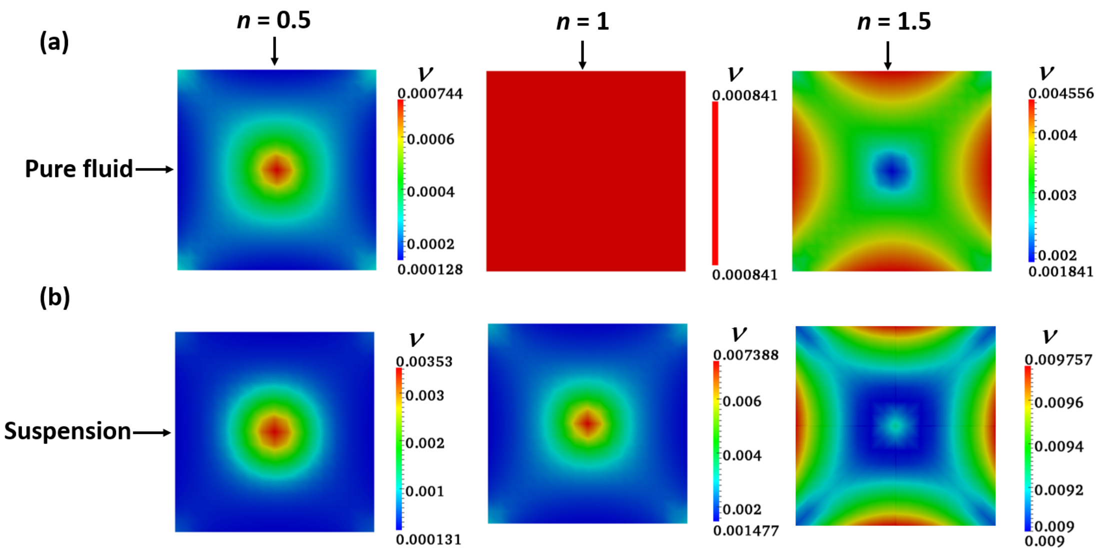

Figure 5.20: Fully-developed cross-sectional kinematic viscosity contours for (a) carrier fluid, and (b) suspension in the straight channel.

The fluid and particle partitioning between the daughter branches are summarized in Table 5.2. The partitioning of the suspension is different from the carrier fluid partitioning. For the equal depth ratio of the daughter branches ($H/B = 1$), the flow is

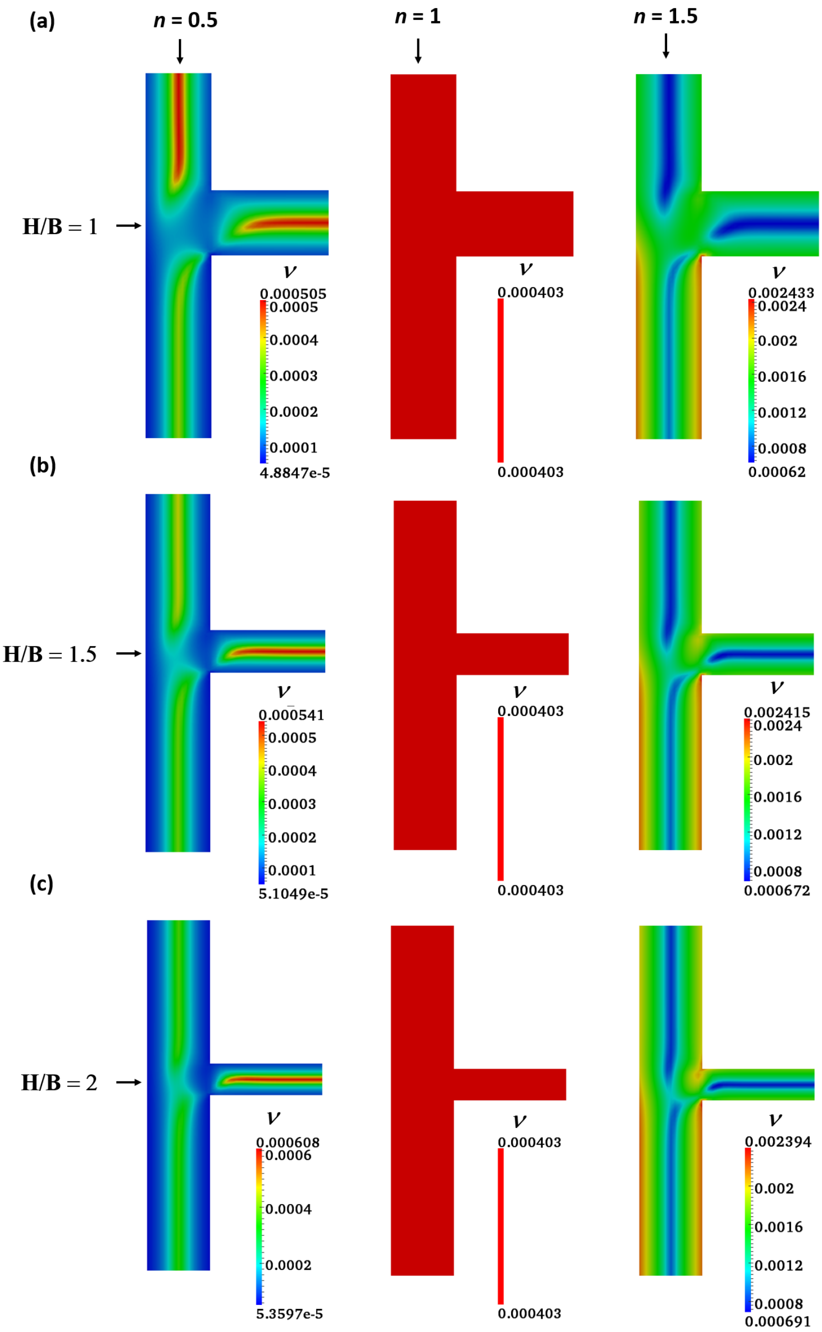

Figure 5.21: The front view ($x - y$ plane) kinematic viscosity contour planes in the bifurcating channel for (a) $H/B = 1$, (b) $H/B = 1.5$, and (c) $H/B = 2$ at mid-plane ($z = H$) for a range of n values for carrier fluid.

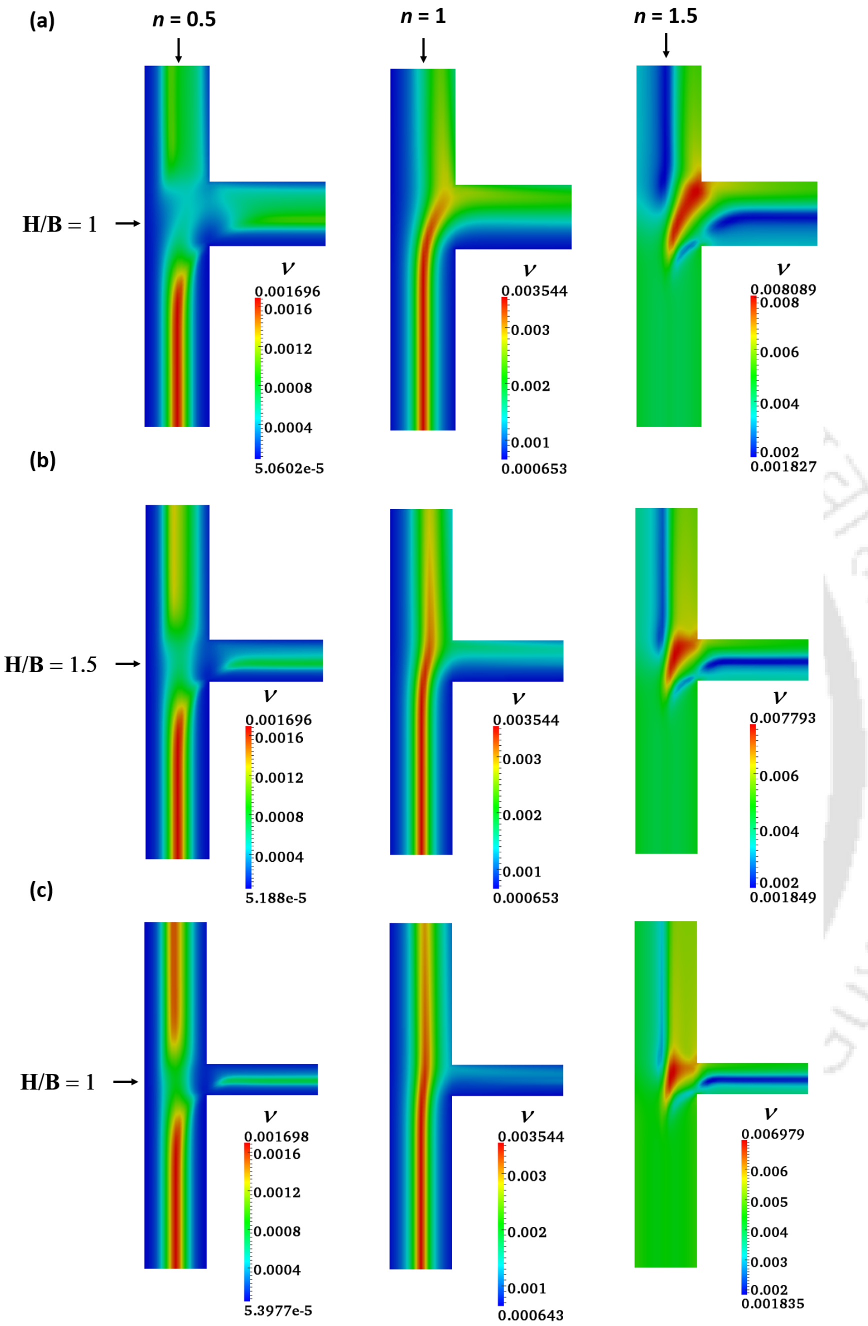

Figure 5.22: The front view ($x - y$ plane) kinematic viscosity contour planes in the bifurcating channel for (a) $H/B = 1$, (b) $H/B = 1.5$, and (c) $H/B = 2$ at mid-plane ($z = H$) for a range of n values for suspension. The particle concentration was 30%.

partitioned almost equally for both pure fluid as well as suspension. This is true for all types of suspension and is in good agreement with the previous findings (Xi and Shapley, 2008). For unequal flow rates in the daughter branches ($H/B = 1.25$, 1.5, 1.75 and 2), the rheology of carrier fluid affects the flow partitioning. As H/B increases, the location of the dividing streamline shifts towards the side branch. Thus, the portion of the fluid that enters into the side branch declines. Among the three carrier fluids, the shear-thinning fluid has the lowest fraction in the side branch. Fig. 5.20 shows the fully-developed cross-sectional kinematic viscosity contour planes for carrier fluid and suspension in the inlet branch. The corresponding mid-plane contours for various n and H/B values for the carrier fluid and suspension around the bifurcation is shown in Figs. 5.21 and 5.22 respectively. For the pure carrier fluid, it can be observed that the shear-thinning fluid has relatively higher viscosity at the inner core compared to the regions near the channel walls. Whereas, the opposite trend is observed for the shear-thickening fluid. As expected for $H/B = 1$, the fluid almost partitioned equally between the daughter branches for all the carrier fluids. However, for $H/B > 1$, this viscosity distribution influences the partitioning of the fluid. The low viscosity region of the shear-thinning fluid encounters less resistance and quickly enters into the side branch. On the other hand, more viscous central core resists diversion into the side branch of the bifurcation, and accordingly, a higher fraction of the flow enters into the main branch, especially for larger values of H/B. Since the viscosity of the shear-thickening fluid is lowest in the fast moving central core compared to the corners and wall regions, the fluid in the core has more tendency to enter the side branch. For a given H/B and n, the presence of the particles decreases the difference in the flow partitioning between the main and side branch. In the case of dense suspension, the presence of the particles modulates the viscosity profiles as shown in Fig. 5.20(b). As we have seen earlier (Fig. 5.6), the suspension shows blunted profiles around bifurcation (location I_1) and the partitioning of the suspension starts immediately when the fluid reaches the location I_1. The bluntness of the profiles in the case of suspension decreases the deviation in the percentage flow partitioning between the daughter branches.

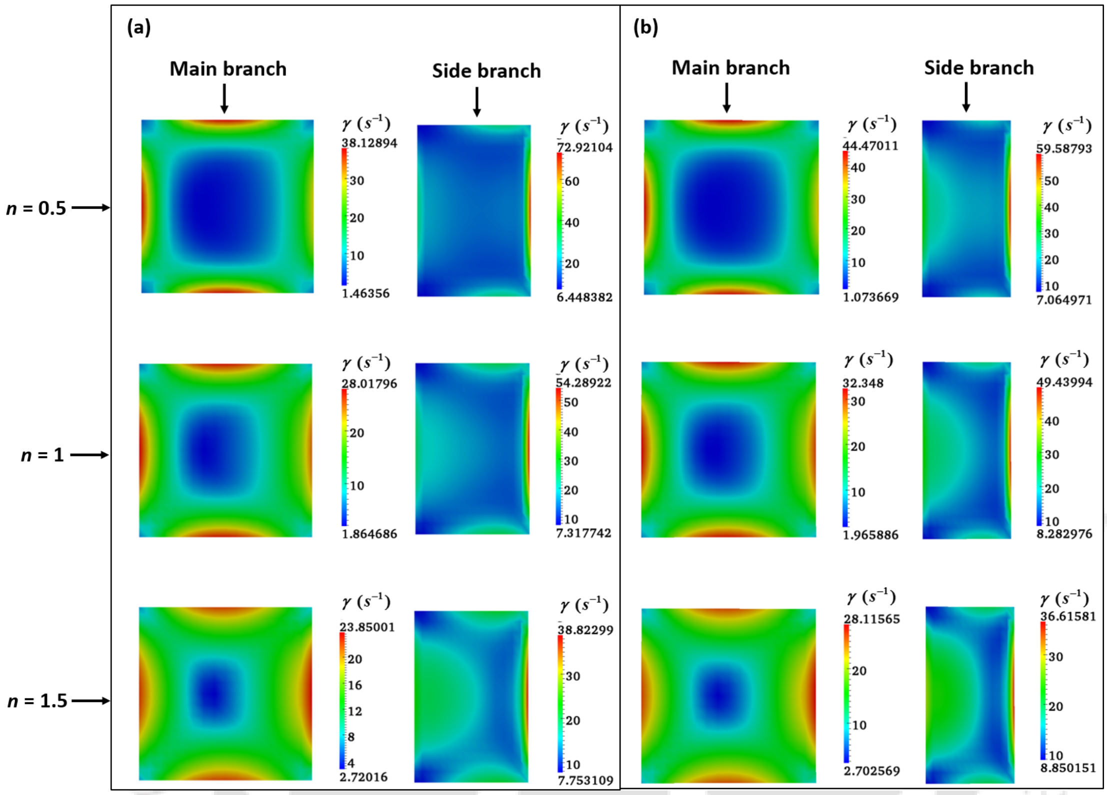

Figure 5.23: The cross-sectional shear-rate contour planes at the entrance of main branch and side branch in the bifurcating channel for (a) $H/B = 1.5$, and (b) $H/B = 2$ for different carrier fluids. The particle concentration was 30%.

The particle partitioning in the non-Newtonian carrier fluids shows a marked difference when compared with the Newtonian carrier (Table 5.2). The shear-induced particle migration causes the inhomogeneous distribution of the particles in the downstream locations of the inlet branch as described in the section 5.5.2. The peak in the particle concentration was observed at the channel center, and the regions near the walls were devoid of the particles. Since the particle-rich region divided equally at the bifurcation, the particles were partitioned equally between the daughter branches for $H/B = 1$. Similar behavior was observed for all types of suspension. For the other cases (H/B = 1.25, 1.5, 1.75 and 2) particles prefer the branch which receives high flow rate. As the flow rate in the main branch increases, the particle-rich central core preferentially enters into this branch. On the other hand, the material that enters into the side branch originates from the wall regions of the inlet branch which is devoid of particles. Among all the carrier fluids, the fraction of the particles entering into the side branch is low for the shear-thinning case. There are two main reasons for the greater fractionation between the daughter branches for the shear-thinning case: the pre-bifurcation concentration profile and the shear-rate field in the bifurcation region. We observe that for the shear-thinning case the shear-rate at the entrance of the side branch is higher compared to the main branch (Fig. 5.23). This is followed by the Newtonian and shear-thickening fluid. Therefore, the gradient in shear-rate causes preferential migration of the particles towards the main branch. The role of particle concentration profile in the inlet branch is also important here. For $H/B > 1$ the particle-rich central core after the bifurcation would preferentially enter into the main branch. On the other hand, the fluid that enters into the side branch originates from the wall regions of the inlet branch. Since the wall regions in case of the shear-thinning suspension have lesser particle concentration compared to the Newtonian and shear-thickening case, we expect higher fractionation of the particles for shear-thinning carrier fluid.

The particle partitioning between the daughter branches does not exactly follow the bulk suspension. The partitioning of the particles depends on the relative volumetric flow rate of the bulk suspension in the daughter branches, and on the rheology of the carrier fluid. Albeit, the carrier fluid rheology has no effect on the particle partitioning as long as the volumetric flow rates in the daughter branches are equal. Here we define a parameter known as fractionation index (χ) which is the percentage difference between the fluid (bulk suspension) and particle partitioning in any one of the daughter branch, say the main branch. Mathematically, it is defined as:

$$\chi = \frac{|X_M^P - X_M^F|}{X_M^F + X_S^F} \times 100, \tag{5.7}$$

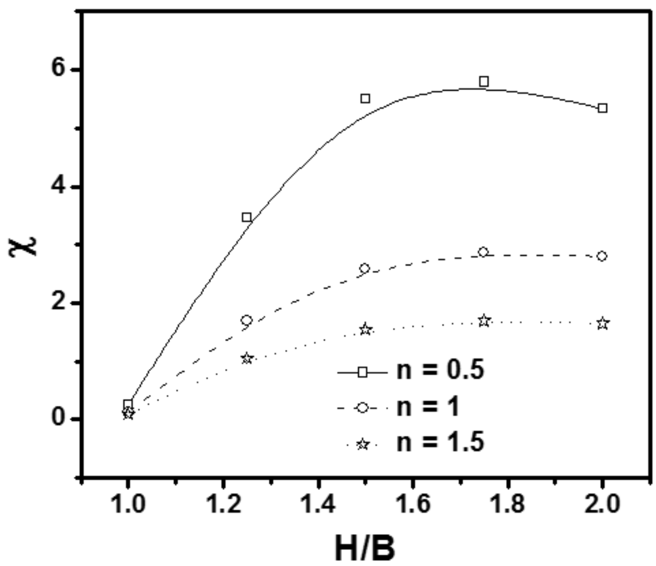

Figure 5.24: The variation of fractionation index with the ratio of the width of the main and daughter branches (H/B) for shear-thinning, shear-thickening and Newtonian carriers.

where X_M^P is the fraction of the particles that enters into the main branch, X_M^F is the fraction of the fluid (bulk suspension) that enters into the main branch, and X_S^F is the fraction of the fluid that enters into the side branch. The comparison of the fractionation index for different H/B and n is shown in the Fig. 5.24. The fractionation index is high for the shear-thinning suspension and low for the shear-thickening when compared with the Newtonian case. These observations are in contrast with the study of D'Avino et al. (2015) who carried out 2D direct numerical simulations of the partitioning of particles suspended in non-Newtonian fluids flowing in a T-junction. They observed that shear-thinning nature of the carrier fluid does not have significant effect as compared to the equivalent Newtonian case. The reason for this mismatch is that the suspension considered by D'Avino et al. (2015) was very dilute (in fact their simulation using fictitious domain method combined with a grid deformation procedure considered the motion of a single particle in the channel). In the absence of the particle-particle hydrodynamic interactions, a particle released at a particular location in the inlet is expected to simply follow the fluid path, irrespective of the type of the fluid as long as the fluid is inelastic. This was not the case in our continuum based simulation of concentrated suspension. The shear-induced migration was observed to depend on the rheology of carrier fluid which affected the relative partitioning of particles in the daughter branches. The fractionation index increases gradually up to $H/B = 1.75$ and then decreases. This is true for all varieties of the carrier suspensions.

5.6 Closure

The numerical simulations of concentrated suspension flow in an asymmetric T-shaped bifurcating channel were carried out to investigate the effect of carrier fluid rheology on the shear-induced particle migration. The DFM with modified diffusivity coefficients (K_c and K_η) was used to compute the velocity and concentration profiles for non-Newtonian carrier suspensions and the results for Newtonian, shear-thinning, and shear-thickening fluids were compared. Suspensions in non-Newtonian carrier fluid exhibited a marked difference in the velocity and concentration fields compared to those in Newtonian carriers. The power-law constitutive model results were compared with Bird-Carreau constitutive model of the carrier fluid and the findings of two models were in good agreement. The simulations were also carried out for carrier fluid without particle phase to investigate the effect of particle phase on the velocity profiles. The presence of the particles and the resulting shear-induced migration led to the blunted velocity profiles. Though, the partitioning of the particles follows the same trend as that of fluid, we observed significant quantitative difference between the two. Very less deviation in fluid-particle partitioning between the daughter branches was observed in the shear-thickening case. On the other hand, the highest deviation was observed in the case of shear-thinning. Therefore, shear-thinning fluid can be more useful for the separation/fractionation of the suspended particles from the bulk suspension in many microfluidic and industrial applications.

Chapter 6

Shear-induced particle migration and size segregation in bidisperse suspension

6.1 Overview

In this chapter, numerical simulations of bidisperse suspension flowing through symmetric T-shape bifurcating channels in converging as well as diverging flow conditions are presented. We have adopted the continuum model of Kanehl and Stark (2015) to analyze the size segregation phenomenon in bidisperse suspension. The particles in the simulations are considered to be rigid and neutrally buoyant. The velocity and concentration profiles for bidisperse suspension are compared with that of the monodisperse case. The effect of particle size ratio and concentration of individual species on the size segregation is investigated.

Published as:

- **M. M. Reddy** and A. Singh. (2019). Shear-induced particle migration and size segregation in bidisperse suspension flowing through symmetric T-shaped channel. https://doi.org/10.1063/1.5089721/j.ijmultiphaseflow.2018.10.005.

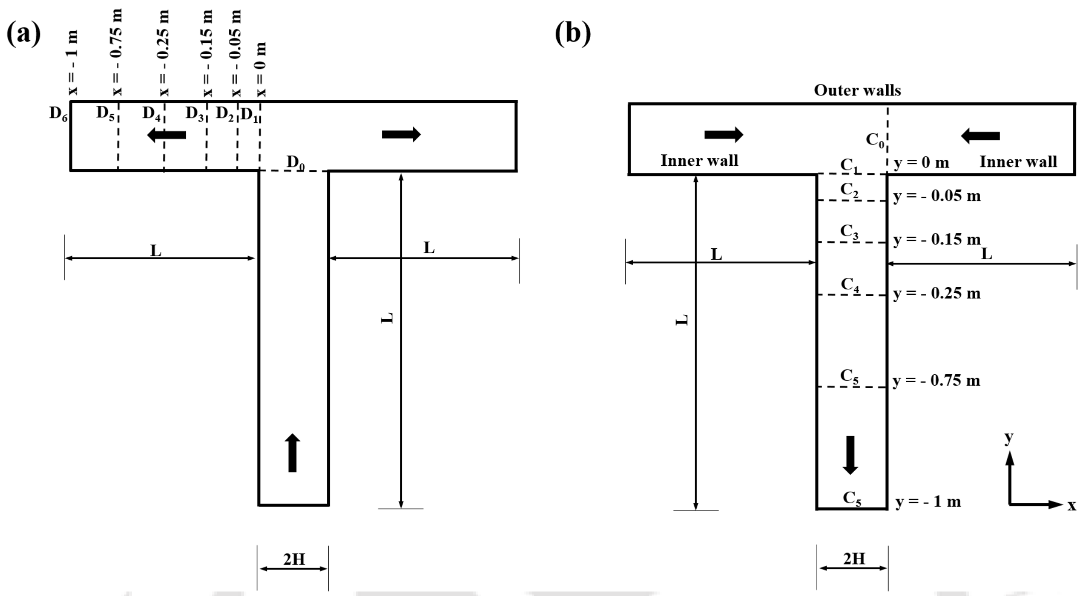

Figure 6.1: Geometrical configuration of the two-dimensional bifurcation channels used in the simulations. (a) diverging flow, and (b) converging flow.

6.2 Problem description

The computational geometry of the diverging bifurcating channel is shown schematically in Fig. 6.1(a). It consists of an inlet and two outlets. The inlet and the daughter branches were of equal width ($2H = 0.0018$ m). The lengths of the inlet and the daughter branches were decided in such a way that the concentration profiles of the individual species in bidisperse suspension become fully-developed. Moreover, the length required for the fully-developed flow depends on the size and concentration of the individual species. For the quantitative comparison purpose, the data was compared at different locations along the length of the channel as shown in Fig. 6.1. The other simulation parameters and geometry details are listed in Table 6.1. The computational geometry for the converging bifurcating channel is shown schematically in Fig. 6.1(b). It consists of two inlets and one outlet. The details of the geometry were the same as in the previous case.

Table 6.1: Geometry details and simulation parameters.

S.No	Parameter	Symbol[Unit]	Value
1	Width of the channel	$2H$ [m]	0.0018
2	Length of the channel	L [m]	1
3	Average inlet velocity	U [m.s^{-1}]	0.0063
4	Fluid density	ρ [kg.m^{-3}]	1190
5	Fluid viscosity	η_0 [cP]	0.48

6.3 Results and discussion

6.3.1 Flow of bidisperse suspension in a straight channel

For a thorough understanding of the effect of particle size ratio and the individual species concentration on the shear-induced migration and margination phenomenon, simulations were carried out for suspension flow in a straight channel without bifurcation. The geometrical details of the straight channel were same as that of the inlet branch. For the comparison purpose, simulations were also carried out for the monodisperse suspension for different particle sizes. Fig. 6.2(a) depicts the fully-developed concentration profiles for monodisperse suspension in the straight channel for two different particle radius (a = 10, 30 μm). The average inlet particle concentration ($\overline{\phi}$) was 0.25 and the velocity magnitude was 0.0063 m/s. The suspension flow in the channel leads to the migration of the particles from high shear-rate wall regions to the low shear-rate center of the channel and forms an inhomogeneity in the particle distribution. Except at the channel center, both sizes of the particles show similar behavior. It is observed that the center-line peak in the case of monodisperse suspension with $a = 10$ μm was slightly high when compared with that of $a = 30$ μm. The non-local shear-rate term which we have introduced in the simulations is a function of the square of the particle size and is responsible for the slight decrease in the peak for $a = 30$ μm. Fig. 6.2(b) depicts the evolution of the concentration profiles along the channel length at various positions in the gradient direction. Since the particle concentration was uniform at the channel entrance, the evolution at various positions starts from a common point. As the suspension flows through the downstream locations of the channel, the shear-induced migration phenomenon causes the gradual increase in the particle concentration at the channel center ($x/H = 0$) and reached the steady-state once the profiles become fully-developed. Whereas, the concentration at the channel walls ($x/H = 1$) and at the location between the channel wall and center ($x/H = 0.5$) decrease gradually. Since the migration flux ($\boldsymbol{N_t}$) scales linearly with the square of the particle size, it is observed that for a given concentration, the suspension with larger particles reaches steady-state relatively quickly in comparison to the smaller particles.

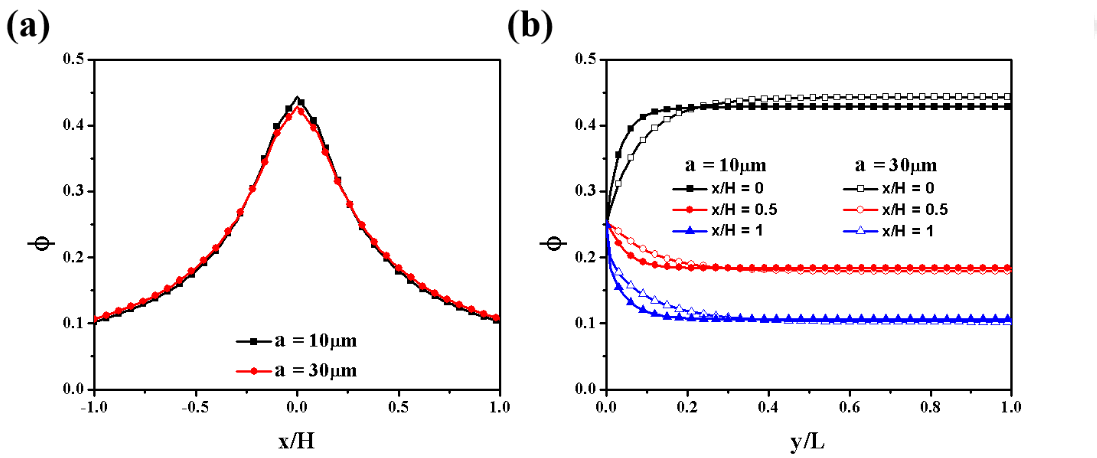

Figure 6.2: (a) Fully-developed concentration profiles and (b) evolution of profiles of monodisperse suspension along the length of the channel in the gradient direction for particle sizes $a = 10\ \mu$m and 30 μm.

Fig. 6.3(a) depicts the fully-developed concentration contour planes of both smaller (ϕ_S) and larger particles (ϕ_L) in a bidisperse suspension. The average inlet particle volume fraction was 0.25 for both the species, with $a_S = 20\ \mu$m and $a_L = 30\ \mu$m having the size ratio, $a_L/a_S = 1.5$. The corresponding contour planes for another mixture with $a_S = 10\ \mu$m and $a_L = 30\ \mu$m ($a_L/a_S = 3$) are shown in Fig. 6.3(b). The quantitative comparison of the fully-developed concentration profiles of bidisperse suspension in the

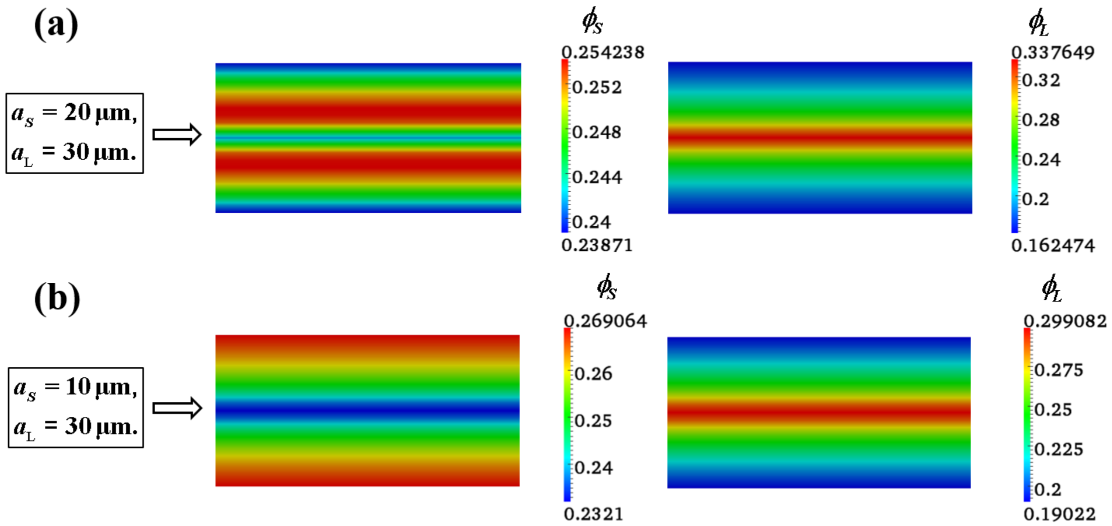

Figure 6.3: Fully-developed concentration contour planes ϕ_i of bidisperse suspension in the straight channel for a_L/a_S = (a) 1.5 and (b) 3. Other parameters were $\overline{\phi}_S = 0.25$ and $\overline{\phi}_L = 0.25$.

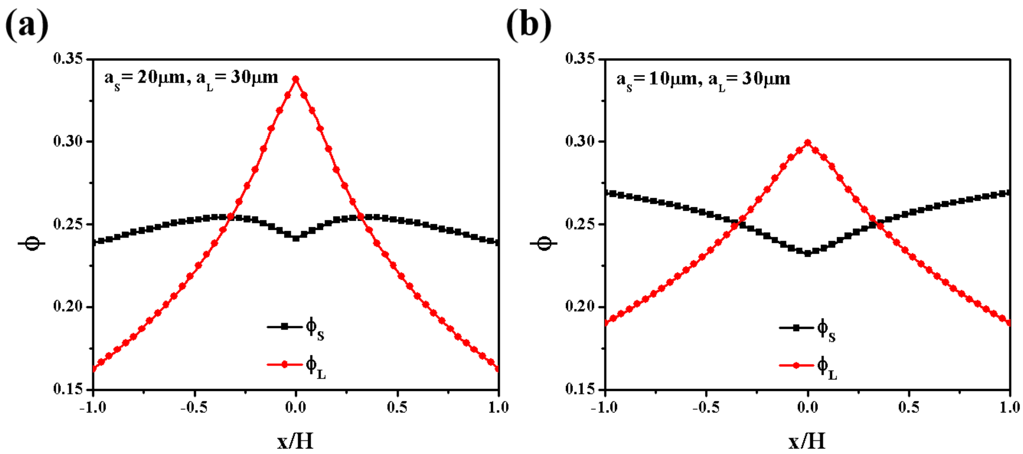

Figure 6.4: Fully-developed concentration profiles ϕ_i of bidisperse suspension in the straight channel for a_L/a_S = (a) 1.5 and (b) 3. Other parameters were $\overline{\phi}_S = 0.25$ and $\overline{\phi}_L = 0.25$.

straight channel for $a_L/a_S = 1.5$ and 3 are shown in Fig. 6.4(a) and 6.4(b) respectively. The profiles clearly show that the particles in the bidisperse suspension behave differently when compared with the monodisperse suspension having the same concentration and size. Irrespective of the particle size, the particle concentration increased at the

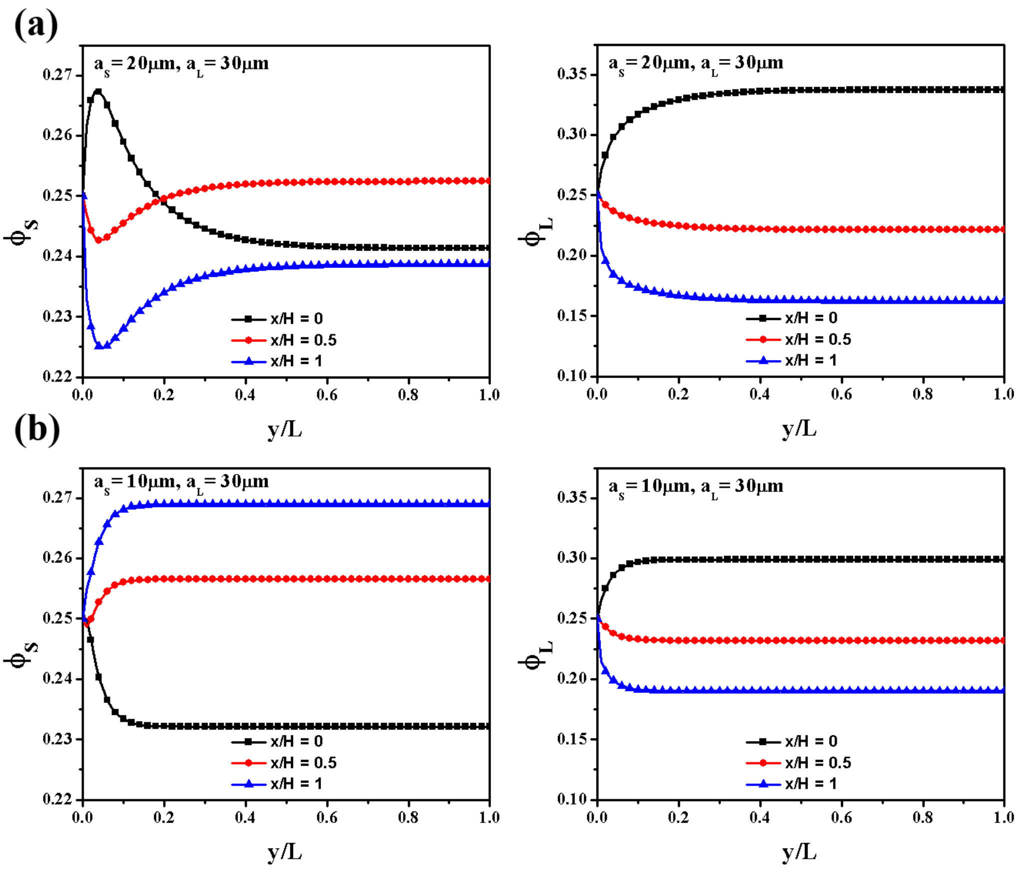

Figure 6.5: Evolution of concentration profiles ϕ_i of bidisperse suspension in the straight channel for a_L/a_S = (a) 1.5 and (b) 3. Other parameters were $\overline{\phi}_S = 0.25$ and $\overline{\phi}_L = 0.25$.

channel center in the monodisperse case. On the other hand, size segregation of the particles occurs favoring the larger particles at the channel center in the bidisperse case composed of an equal concentration of smaller and larger particles ($\overline{\phi}_S = \overline{\phi}_L$). The particle size ratio clearly affects the size segregation of the smaller particles in a bidisperse suspension. For a size ratio of $a_L/a_S = 1.5$, the concentration peak for the smaller particles is located between the channel center and wall. Whereas, for $a_L/a_S = 3$, the peak is located near the channel walls. Previous experimental studies of Husband et al. (1994), Lyon and Leal (1998b), and Semwogerere and Weeks (2008) explained that the enrichment of the larger particles at the channel center is due to the particle size scaling

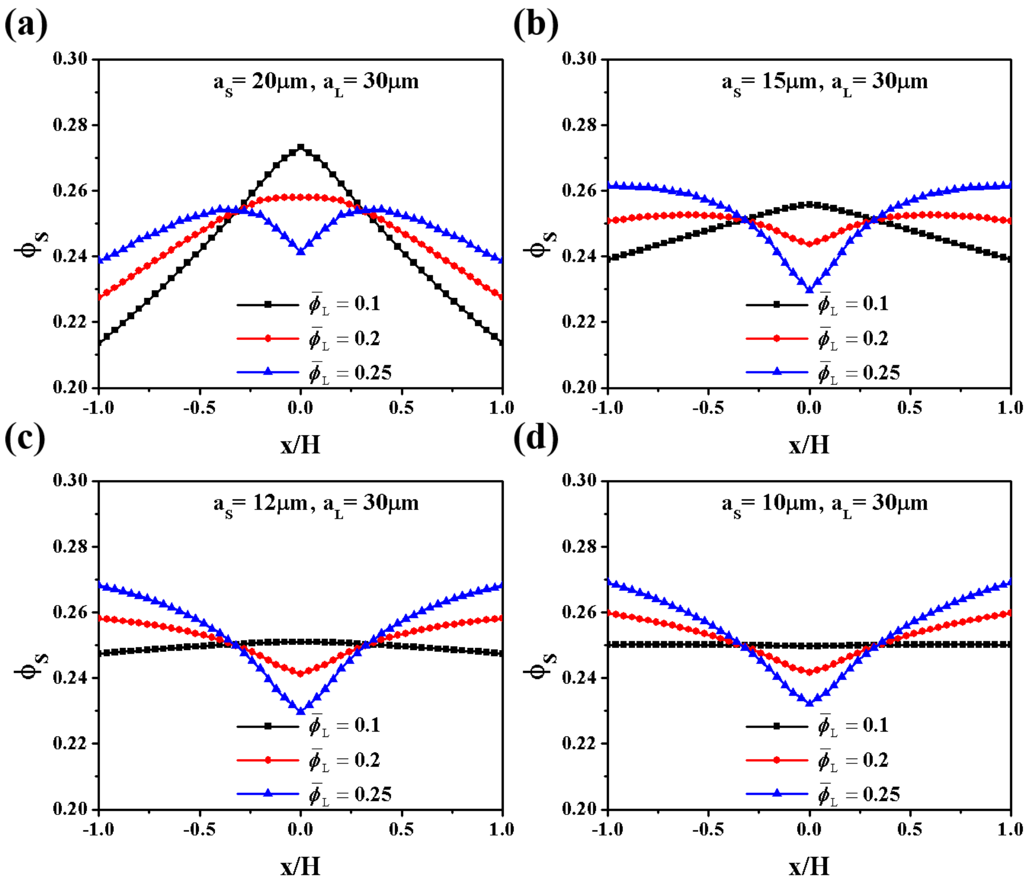

Figure 6.6: Fully-developed concentration profiles ϕ_S of bidisperse suspension for various $\bar{\phi}_L$. The mean concentration of the smaller particles was kept constant ($\bar{\phi}_S = 0.25$). (a) $a_L/a_S = 1.5$, (b) $a_L/a_S = 2$, (c) $a_L/a_S = 2.5$ and (d) $a_L/a_S = 3$.

of shear-induced migration flux in both Brownian and non-Brownian suspension. According to their study, since the migration flux scales linearly with the square of the particle size, the size segregation of the particles is a result of the faster migration of the larger particles to the channel center than that of the smaller particles in the bidisperse suspension having an equal concentration of the individual species. In order to obtain a complete picture of the fully-developed concentration profiles, the evolution of the individual species concentration profiles along the channel length at various positions in the gradient direction is shown in Fig. 6.5. As we have discussed in section 2.2.4, the shear-induced migration and collective diffusion will decide the position of the individual

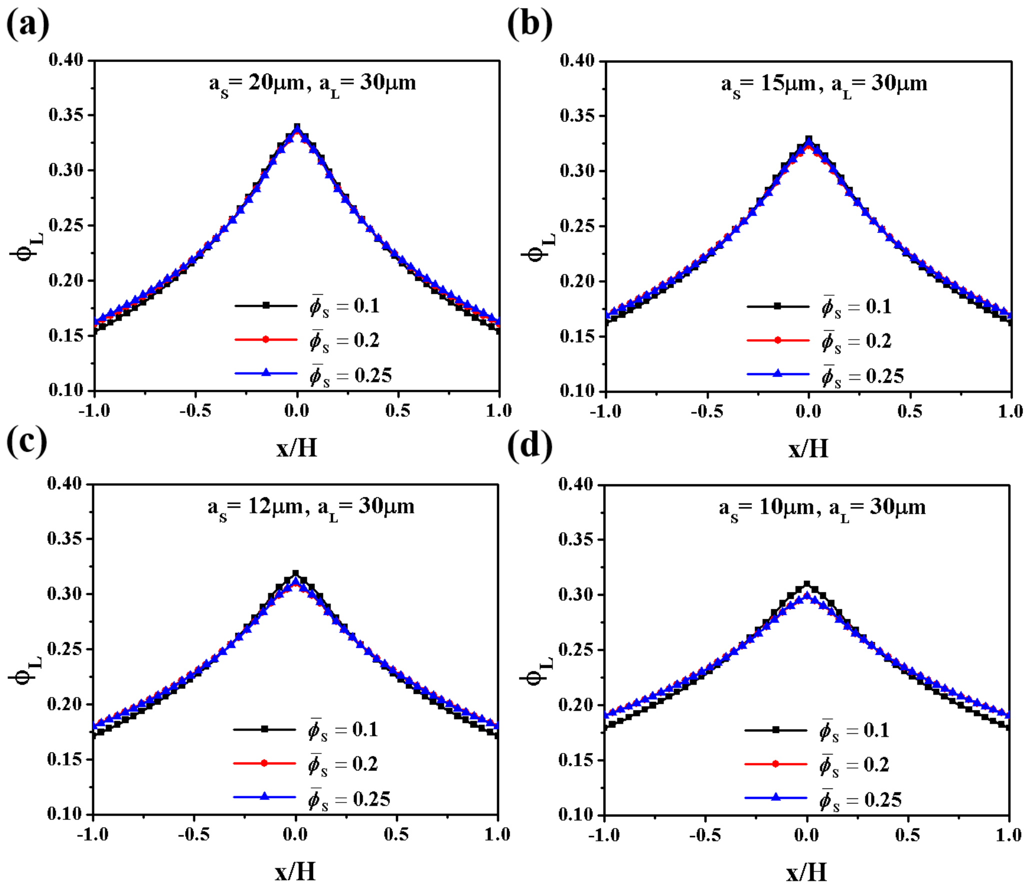

Figure 6.7: Fully-developed concentration profiles ϕ_L of bidisperse suspension for various $\bar{\phi}_S$. The mean concentration of smaller particles was kept constant ($\bar{\phi}_L = 0.25$). (a) $a_L/a_S = 1.5$, (b) $a_L/a_S = 2$, (c) $a_L/a_S = 2.5$ and (d) $a_L/a_S = 3$.

species in a bidisperse suspension. Moreover, these fluxes depend upon the shear-rate, particle size ratio and individual concentration of the particles. Since the concentration of the individual species was uniform at the channel entrance, the flux due to diffusional currents can be neglected across the channel cross-section. Thereby, only the flux due to shear-induced migration dominates. As a result, both species migrate towards the low shear-rate channel center. Since the shear-induced particle migration scales with the square of the particle size, faster migration is observed in the case of larger particles. This is in good agreement with the previous experimental findings. As soon as the inhomogeneity in the particle concentration exists, the flux due to diffusion of the particles comes into play. Though the particles considered in the simulations were in the non-Brownian limit, the thermal collective diffusion dominates close to the channel center over shear-induced migration. Since the larger particles reach high enough local volume fraction at the channel center, they effectively push the smaller particles away from the channel center. Thereby, de-mixing of the particles takes place and the smaller particles will settle at a position where the two aforementioned fluxes balance each other. For $a_L/a_S = 1.5$, the smaller particle concentration at the channel walls and location between the channel wall and center increases gradually until the steady-state is reached. Since the size ratio is less for $a_L/a_S = 1.5$, the concentration peak for the smaller particles is located in between the channel walls and center. The qualitative nature of the evolution of the larger particles was observed to be almost similar for particle size ratio $a_L/a_S = 3$. However, the evolution of the smaller particles is observed to be different in the case of $a_L/a_S = 3$. From the Fig. 6.5(b) it is observed that unlike the previous case, the smaller particles concentration monotonically decreases at the channel center. For higher particle size ratios, the collective diffusion dominates over shear-induced migration. Thereby, smaller particles are pushed towards the walls regions.

The effect of the individual particle size ratio and species concentration on the segregation phenomenon in bidisperse suspension was studied by carrying out simulations for a range of a_L/a_S and $\overline{\phi}_S/\overline{\phi}_L$. Fig. 6.6 depicts the fully-developed concentration profiles of smaller particles (ϕ_S) in the bidisperse suspension for various $\overline{\phi}_S/\overline{\phi}_L$ and a_L/a_S. In all cases, the mean particle concentration of the smaller particles ($\overline{\phi}_S$) was 0.25 and the size of the larger particles was 30 μm. It is observed that for the low concentration of the larger particles, the smaller particles migrate to the center of the channel and this is in good agreement with the previous findings for Brownian suspension as well as for non-Brownian suspension (Lyon and Leal, 1998b; Semwogerere and Weeks, 2008). The particle size ratio, a_L/a_S, also have an influence on the size segregation. From the Fig. 6.6, it is observed that the size segregation of the particles enhances with particle size ratio (a_L/a_S) for a given $\overline{\phi}_S/\overline{\phi}_L$. The corresponding comparison of the fully-developed concentration profiles for the larger particles is shown in Fig. 6.7. It was observed that in all the cases, the larger particles always migrate away from the walls, and thereby, the concentration peak is always at the channel center.

6.3.2 Flow of bidisperse suspension in a diverging channel

For a bidisperse suspension, the distribution of the particles after bifurcation depends on various factors such as relative flow rate through the daughter branches, orientation of the bifurcation, pre-bifurcation concentration profiles etc. As we have seen in the previous section, the fully-developed concentration profiles of individual particles (ϕ_i) in the bidisperse suspension strongly depend on the size and concentration ratio of the individual species. For a bidisperse suspension composed of an equal concentration of both the species, the size ratio of the particles decides the size segregation. In order to understand the influence of the particle size ratio on the distribution of the particles after bifurcation, simulations were extended for the suspension flow in a 2D symmetric T-shaped bifurcating channel. Both diverging and converging cases were considered. In this section, we are dealing with the suspension flow in the diverging bifurcating channel. At the entrance of the channel, the average particle fraction of both the species was equal ($\overline{\phi}_S = \overline{\phi}_L = 0.25$). The average inlet velocity magnitude was 0.0063 m/s. For the comparison purpose, simulations were also carried out for the monodisperse suspension.

Fig. 6.8 depicts the concentration contour of monodisperse suspension around the junction of bifurcation as well as at the outlet locations of the daughter branches in the diverging bifurcating channel. The average inlet concentration ($\overline{\phi}$) was 0.25 and the particle size (a) was 10 μm. In the inlet section, the shear-induced migration causes the particles to move towards the center of the channel. The central core of the inlet channel which has a high concentration of the particles meets the junction of the left and right

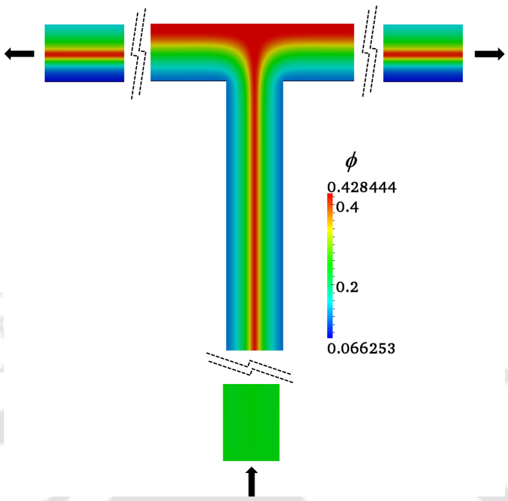

Figure 6.8: Particle concentration contour plane of monodisperse suspension in the diverging bifurcating channel. The average inlet concentration was ($\bar{\phi}$) 0.25 and the particle size (a) was 10 μm.

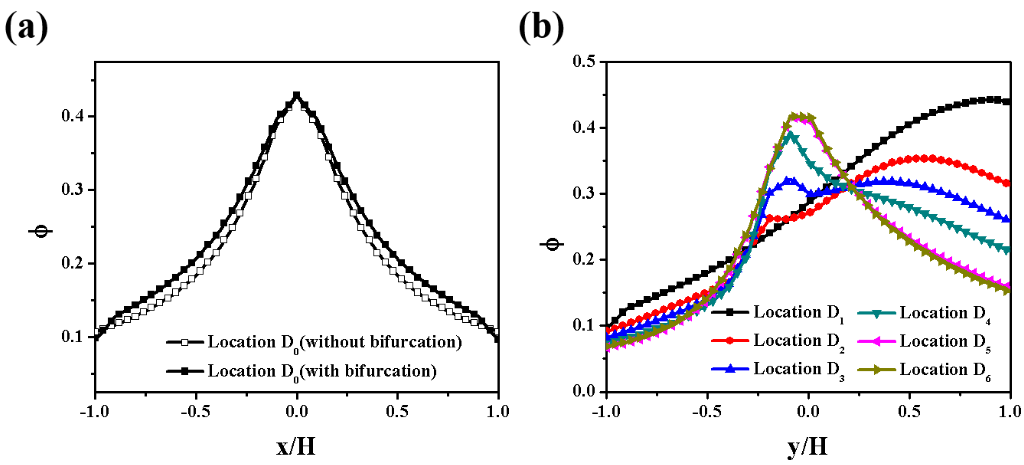

Figure 6.9: Comparison of the concentration profiles (a) at location D_0 with and without bifurcation and (b) at various locations in the outlet branch for monodisperse suspension in the converging bifurcating channel. The average inlet concentration was ($\bar{\phi}$) 0.25 and the particle size (a) was 10 μm.

branches of outer walls. This makes the particle concentration in the daughter branches increase near the outer walls at upstream locations. On the other hand, the inner walls of the daughter branches receive from the wall regions of the inlet branch. As a result, the particle concentration decreases at the inner walls of the bifurcation. However, even in the daughter branches, the channel walls offers high shear-rate compared to the channel center. The shear-rate and concentration gradients drive the particles towards the channel center as the suspension flows through the downstream locations of the daughter branches as shown in Fig. 6.8. In order to understand the quantitative nature of the particle distribution, we have shown the concentration profiles at different locations in the bifurcating channel in Fig. 6.9. Since the bifurcating channel is symmetric, the profiles were drawn only in one daughter branch (left branch). The effect of bifurcation on the fully-developed concentration profile can be seen in Fig. 6.9(a) which shows the comparison of concentration profiles at location D_0 with and without bifurcation. As soon as the suspension reaches the bifurcation point (location D_0), deceleration of the flow into daughter branches starts. Thereby, the concentration profile at location D_0 with bifurcation shows little variation when compared with the profile in the straight channel. The symmetric profiles which were observed in the inlet branch become asymmetric after the bifurcation. Immediately after leaving the inlet branch, the suspension diverges into the left and right branches along the dividing streamlines. After the bifurcation, the particle-rich central core hits the junction of outer walls of the daughter branches. This leads to the shifting of the peak in the concentration towards the outer walls of the channel at location D_1. However, as the suspension moves towards the downstream locations of the daughter branches, the gradients in the shear-rate and concentration leads to the shifting of the concentration peak towards the channel center. The profiles at locations D_5 and D_6 coincide and confirms the profiles were fully-developed. The qualitatively similar behavior can be observed for other particle sizes.

Fig. 6.10 depicts the concentration contour planes of the smaller (ϕ_S) and larger particles (ϕ_L) along with the overall concentration ($\phi_{overall}$) around the junction of bifurcation and at the outlet locations of the daughter branches of bidisperse suspension in diverging bifurcating channel for $a_S = 20$ μm and $a_L = 30$ μm having $a_L/a_S = 1.5$. The corresponding contour planes for $a_S = 10$ μm and $a_L = 30$ μm having $a_L/a_S = 3$ are

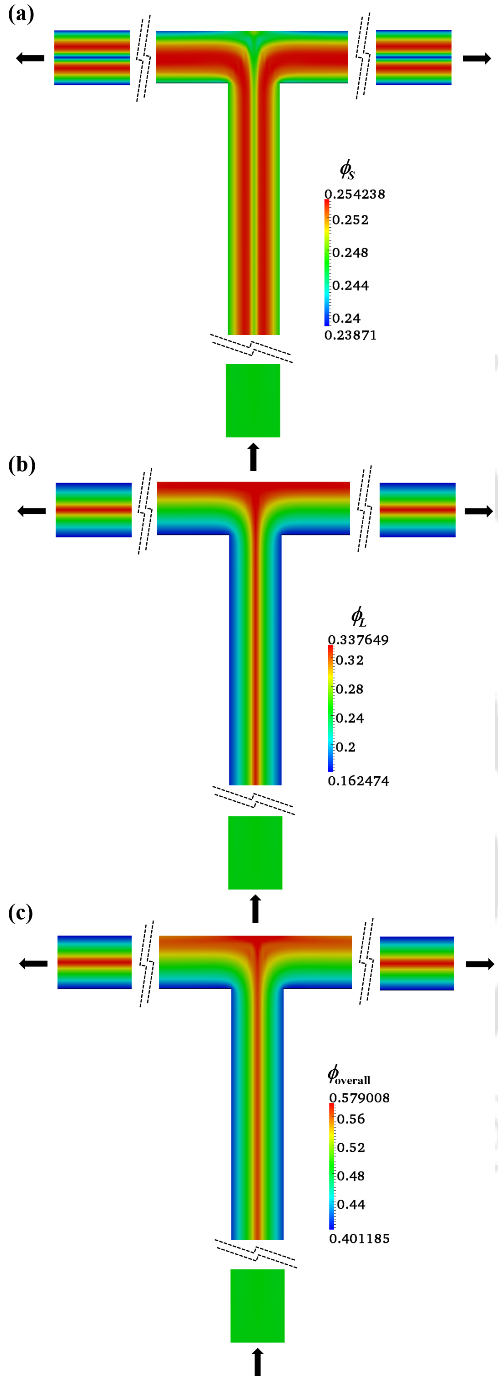

Figure 6.10: The particle concentration contour planes of (a) smaller particles, (b) larger particles and (c) overall concentration of bidisperse suspension in the diverging bifurcating channel. The particle sizes were a_S = 20 μm and a_L = 30 μm.

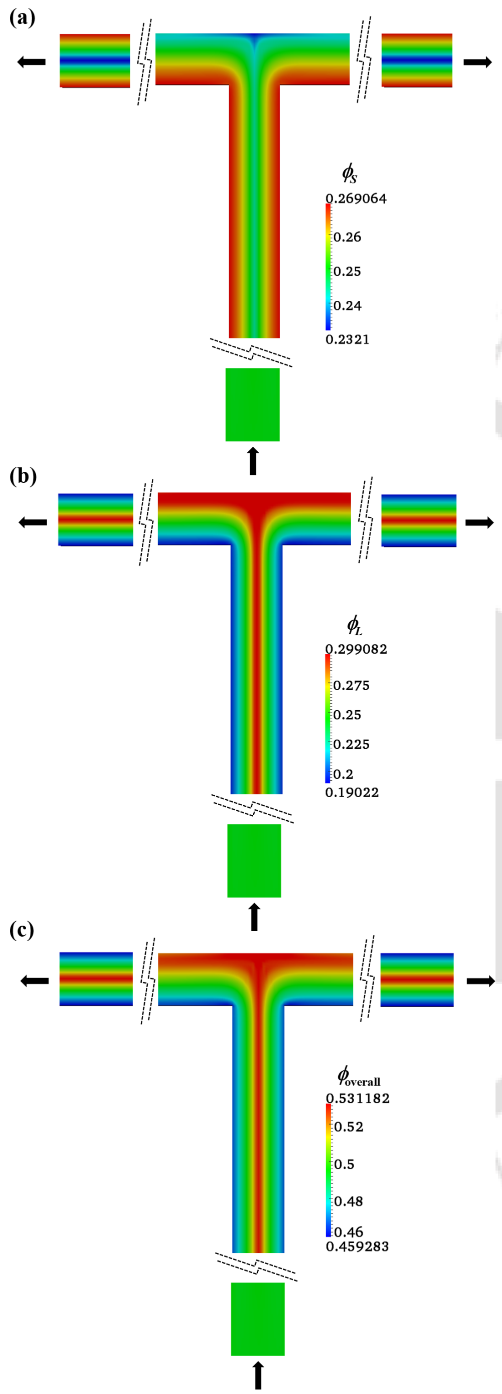

Figure 6.11: Particle concentration contour planes of (a) smaller particles, (b) larger particles and (c) overall concentration of bidisperse suspension in the diverging bifurcating channel. The particle sizes were $a_S = 10$ μm and $a_L = 30$ μm.

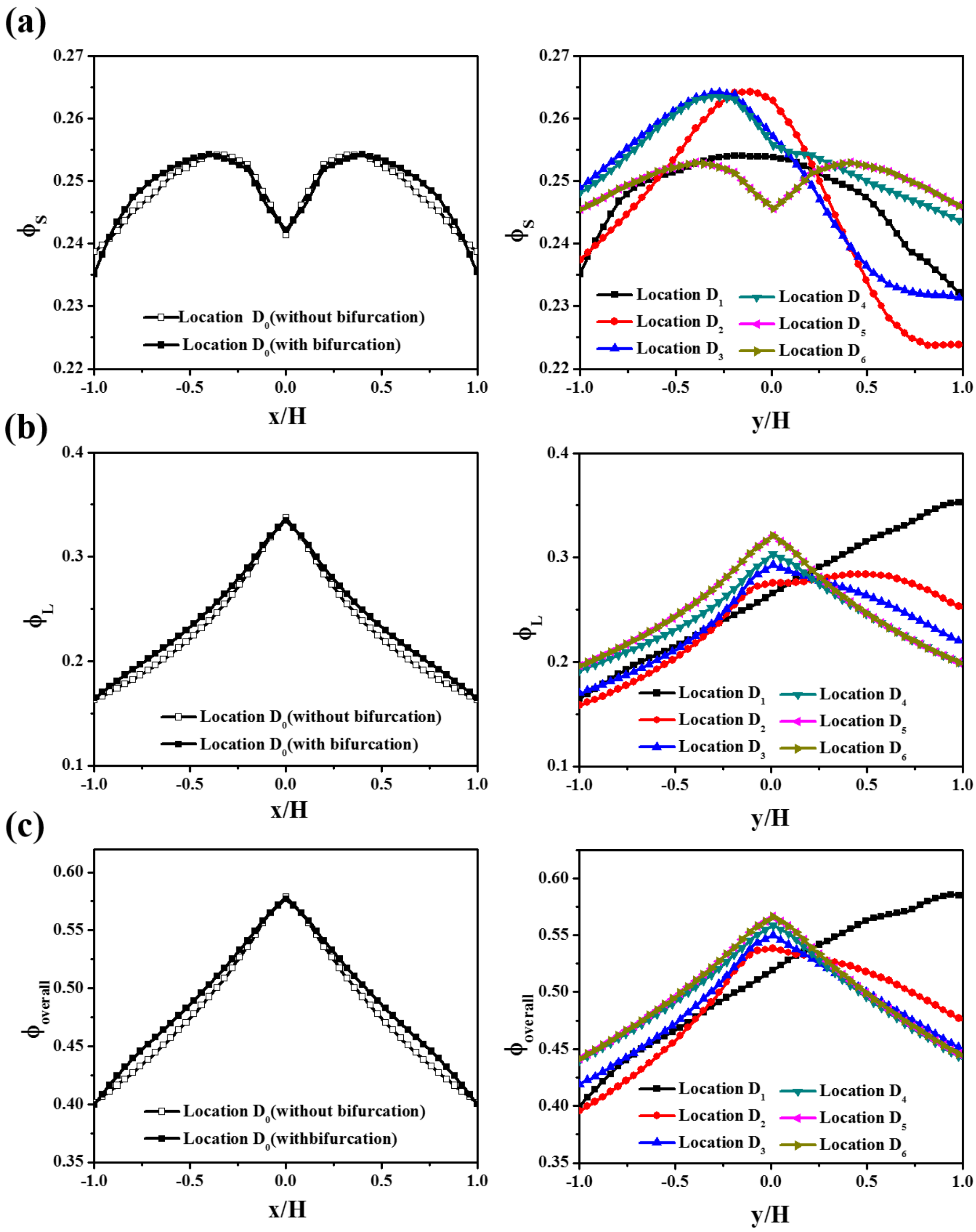

Figure 6.12: Comparison of the concentration profiles of (a) smaller particles, (b) larger particles and (c) overall concentration of bidisperse suspension at different locations in the diverging bifurcating channel. The particle sizes were a_S = 20 μm and a_L = 30 μm.

shown in Fig. 6.11. The individual species behave differently in the bidisperse suspension than in monodisperse suspension flow in a bifurcating channel. Depending on the particle

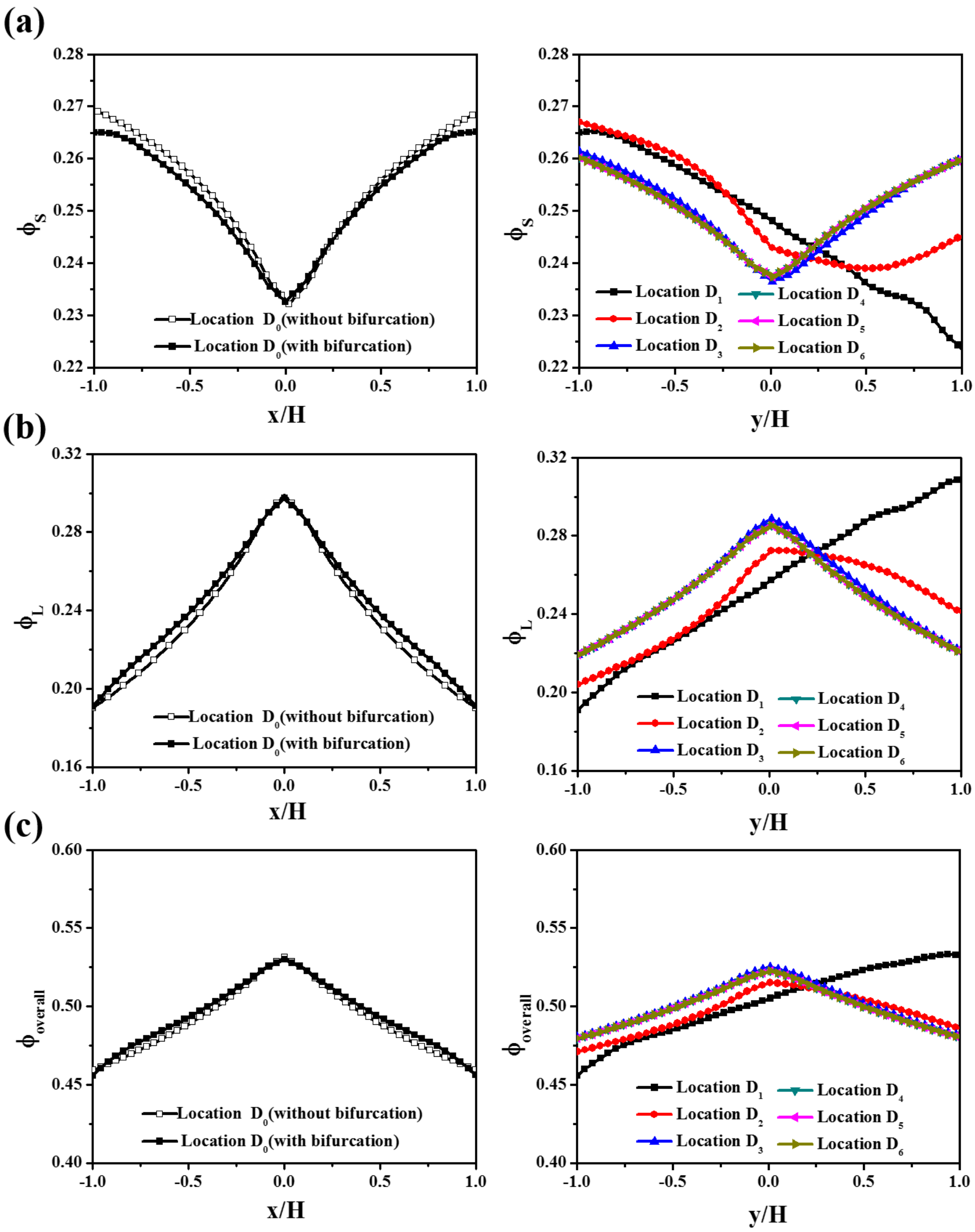

Figure 6.13: Comparison of the concentration profiles of (a) smaller particles, (b) larger particles and (c) overall concentration of bidisperse suspension at different locations in the diverging bifurcating channel. The particle sizes were $a_S = 10$ μm and $a_L = 30$ μm.

size ratio, the position of the concentration peak for smaller particles varies around the channel cross-section and effects the particle distribution after the bifurcation. For particle size ratio $a_L/a_S = 1.5$, the population of the smaller particles is more at locations in between channel wall and center. Whereas, this population is more at the channel walls for particle size ratio $a_L/a_S = 3$. As soon as the suspension reaches the bifurcation junction, the larger particles which were populated at the channel center in the upstream locations of the inlet branch travel without much deviation towards the outer walls of the daughter branches. As a result, the concentration of the larger particles is more at the outer walls and less at the inner walls of the daughter branches (see Figs. 6.10(b) and 6.11(b)). Since the larger particles populated at the channel center for both particle size ratios, qualitatively similar nature is observed with that of the monodisperse case. On the other hand, the smaller particles in the bidisperse case behave differently depending on the particle size ratio. For particle size ratio $a_L/a_S = 1.5$, the two concentration peaks of the smaller particles which are present at the locations between the channel wall and center bifurcate into the left branch and the right branch. As a result, high concentration of the smaller particles is expected near the channel center in the daughter branches. Whereas, for the particle size ratio $a_L/a_S = 3$, the concentration peak which is located at the channel walls in the downstream locations of the inlet branch move along the inner walls of the daughter branches. Thereby, the concentration of the smaller particles is more at the inner walls of the daughter branches. As the suspension flows through the downstream locations of the daughter branches, the gradients in the concentration and shear-rate lead to re-adjustment of the profiles. At the outlet locations, the concentration profiles become almost symmetric.

The quantitative nature of the concentration profiles of bidisperse suspension at different locations in the diverging channel for $a_L/a_S = 1.5$ and 3 are shown in Fig. 6.12 and 6.13 respectively. The bifurcation of the channel causes a slight deviation in the fully-developed concentration profiles at location D_0 (first column in Figs. 6.12 and 6.13). For both particle size ratios, the concentration peak for the larger particles at the entrance of the daughter branches (location D_1) was shifted towards the outer walls. On the other hand, a quite different behavior is observed in the case of smaller particles. For $a_L/a_S = 1.5$, the concentration peak of the smaller particles shifts towards the center of the daughter branches after bifurcation. Whereas, for $a_L/a_S = 3$, it is shifted towards the inner walls of the daughter branches. As the suspension moves towards the downstream locations of the daughter branches, the gradients in the shear-rate and concentration again cause the particles to move towards the channel center. It is clearly seen from Figs. 6.12 and 6.13, the asymmetric profiles observed in the upstream locations of the daughter branches eventually become symmetric in the downstream locations of the daughter branches. The qualitative nature of the overall particle concentration profiles is observed to be similar to that of larger particles.

6.3.3 Flow of bidisperse suspension in a converging channel

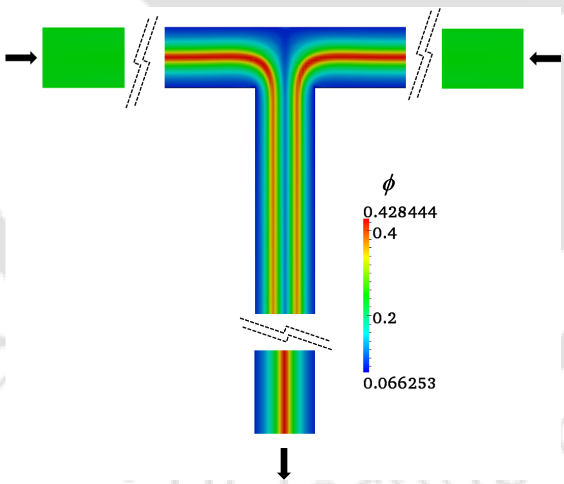

Figure 6.14: Particle concentration contour plane of monodisperse suspension in the converging bifurcating channel. The average inlet concentration was ($\overline{\phi}$) 0.25 and the particle size (a) was 10 μm.

The concentration contour planes for the monodisperse suspension around the junction of the converging section and at the downstream location of the outlet branch in the converging bifurcating channel are shown in Fig. 6.14. The average inlet concentration ($\overline{\phi}$) was 0.25 and the particle size (a) was 10μm. The flow was provided in each inlet

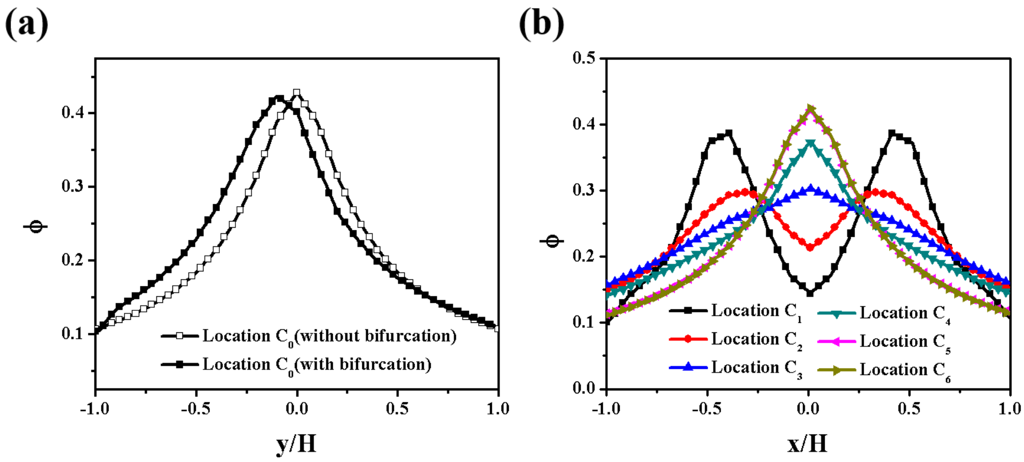

Figure 6.15: Comparison of the concentration profiles (a) at location C_0 with the fully-developed concentration profile in the straight channel and (b) at various locations in the outlet branch for monodisperse suspension in the converging bifurcating channel. The average inlet concentration was $(\overline{\phi})$ 0.25 and the particle size (a) was 10 μm.

arm with an average velocity of $U = 0.0063$ m/s. In both inlet arms, the shear-induced migration causes the particles to move towards the center of the channel. Two separated concentration peaks can be visible as the suspension converges into the outlet branch from the two inlet branches. However, as the suspension flows through the downstream locations of the outlet branch, the two concentration peaks gradually merge at the center of the channel. The quantitative nature of the particle distribution at different locations in the bifurcating channel is shown in Fig. 6.15. The Fig. 6.15(a) shows the comparison of concentration profile at location C_0 with and without bifurcation. As the suspension reaches the converging section (location C_0), the flow bends towards the outlet section and the concentration profile becomes asymmetric. Whereas, the symmetric profile was observed in the case of the straight channel. It was observed that at location C_1, initially two separated concentration cores appear as a result of the flow of suspension from the two inlet branches. However, the gradients in the shear-rate and the particle concentration which were present cause the redistribution of the particles. As we move downstream in the outlet section the two streams gradually come closer. At location

C_3 these two streams of concentration mix completely. As we move down further in the outlet section we observe that the concentration peak at the channel center increases gradually and the profile becomes fully-developed beyond location C_5 (Fig. 6.15(b)). The qualitatively similar behavior can be observed for other particle sizes.

Fig. 6.16 depicts the concentration contour planes of the smaller (ϕ_S) and larger particles (ϕ_L) along with the overall concentration ($\phi_{overall}$) in converging bifurcating channel for $a_L/a_S = 1.5$. The corresponding contour planes for $a_L/a_S = 3$ are shown in Fig. 6.17. For particle size ratio $a_L/a_S = 1.5$, there exist two concentration peaks of the smaller particles in the inlet arms. As soon as the suspension reaches the converging section, four separated concentration streams of smaller particles were observed. Whereas, for particle size ratio $a_L/a_S = 3$, three separated concentration streams of smaller particles were observed. On the other hand, only two were observed for the larger particles irrespective of the particle size ratio. As the suspension flows through the downstream locations of the daughter branches, the separated streams gradually merge each other.

The quantitative nature of the concentration profiles of bidisperse suspension at different locations in the converging channel for $a_L/a_S = 1.5$ is shown in Fig. 6.18. The corresponding profiles for $a_L/a_S = 3$ are shown in Fig. 6.19. As the suspension reaches the converging point (location C_0), the particles bend with the flow towards the outlet section. As a result, the profiles at location C_0 become asymmetric in nature when compared with the corresponding concentration profiles in the straight channel. As the suspension converges from the both inlet arms, two concentration peaks were observed at the location C_1 for the larger particles. This is true for both the particle size ratios. On the other hand, the smaller particles in the bidisperse case behave differently depending on the particle size ratio. For particle size ratio $a_L/a_S = 1.5$, the two concentration peaks of the smaller particles which were present in each inlet arm converge to form two symmetric peak-valley-peak patterns at the entrance of the outlet section. Whereas, for $a_L/a_S = 3$, the concentration peaks which were present on the inner walls of the inlet

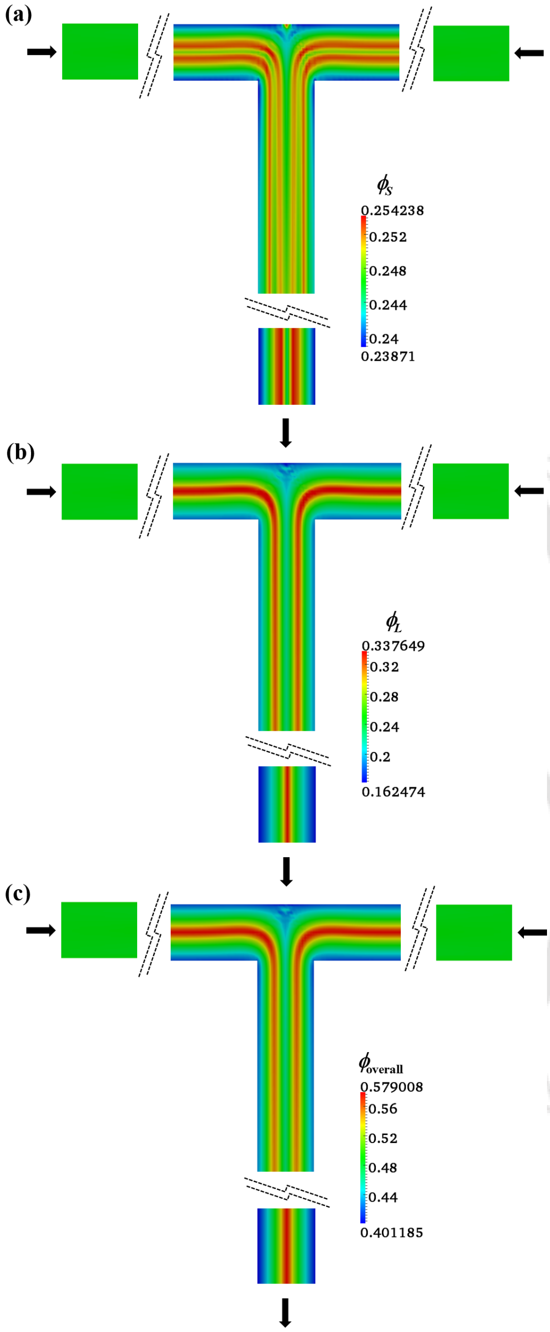

Figure 6.16: The particle concentration contour planes of (a) smaller particles, (b) larger particles and (c) overall concentration of bidisperse suspension in the converging bifurcating channel. The particle sizes were $a_S = 20$ μm and $a_L = 30$ μm.

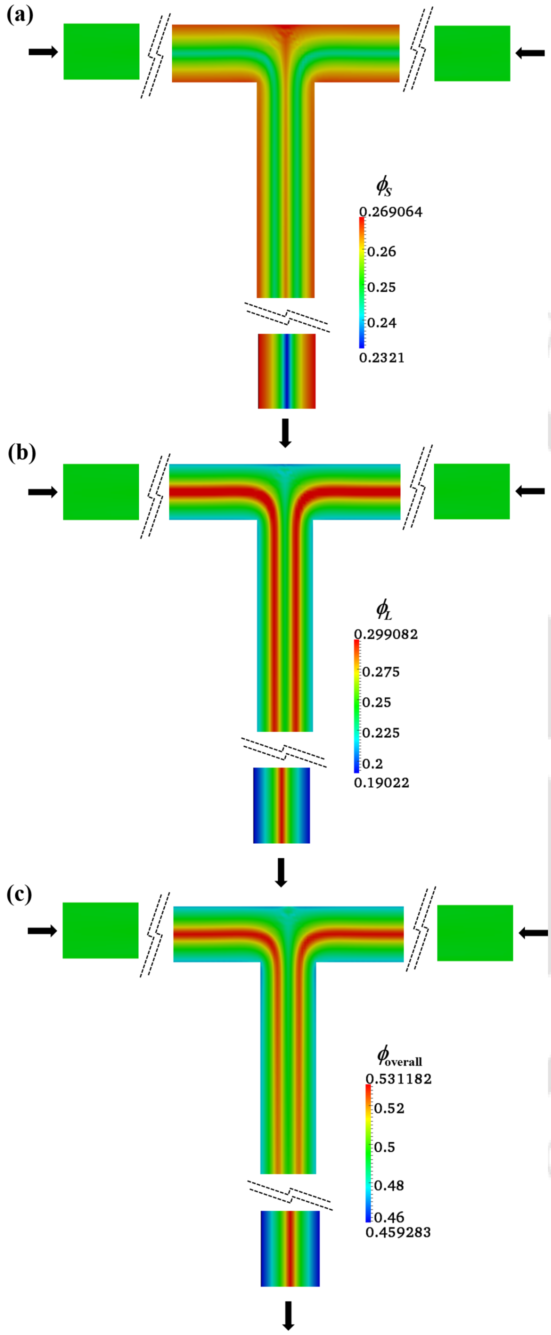

Figure 6.17: Particle concentration contour planes of (a) smaller particles, (b) larger particles and (c) overall concentration of bidisperse suspension in the converging bifurcating channel. The particle sizes were a_S = 10 μm and a_L = 30 μm.

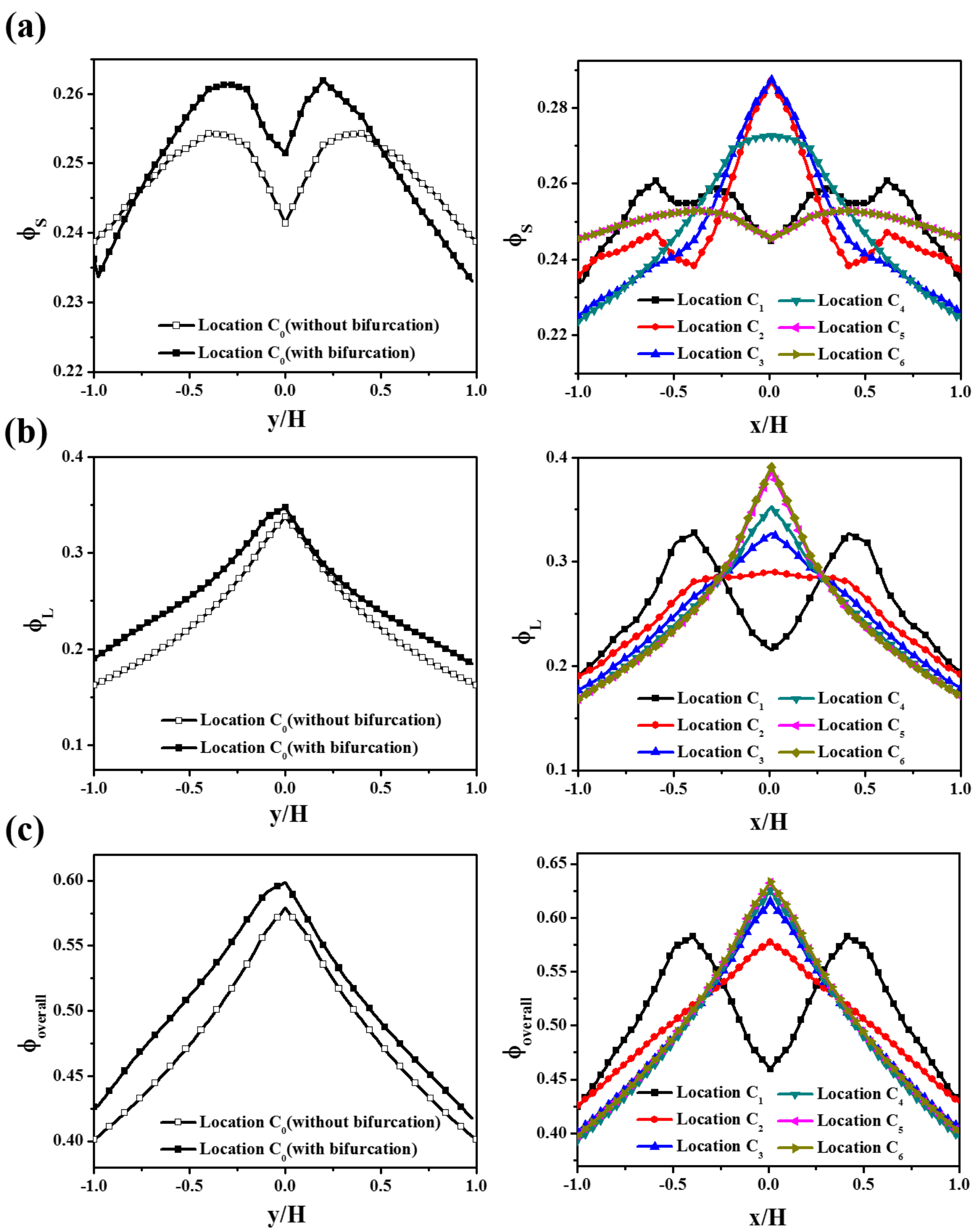

Figure 6.18: Comparison of the concentration profiles of (a) smaller particles, (b) larger particles and (c) overall concentration of bidisperse suspension at different locations in the converging bifurcating channel. The particle sizes were a_S = 20 μm and a_L = 30 μm.

arms follow with the walls of the outlet branch. The concentration peaks which were present on the outer walls of the inlet arms merge together and enter into the outlet

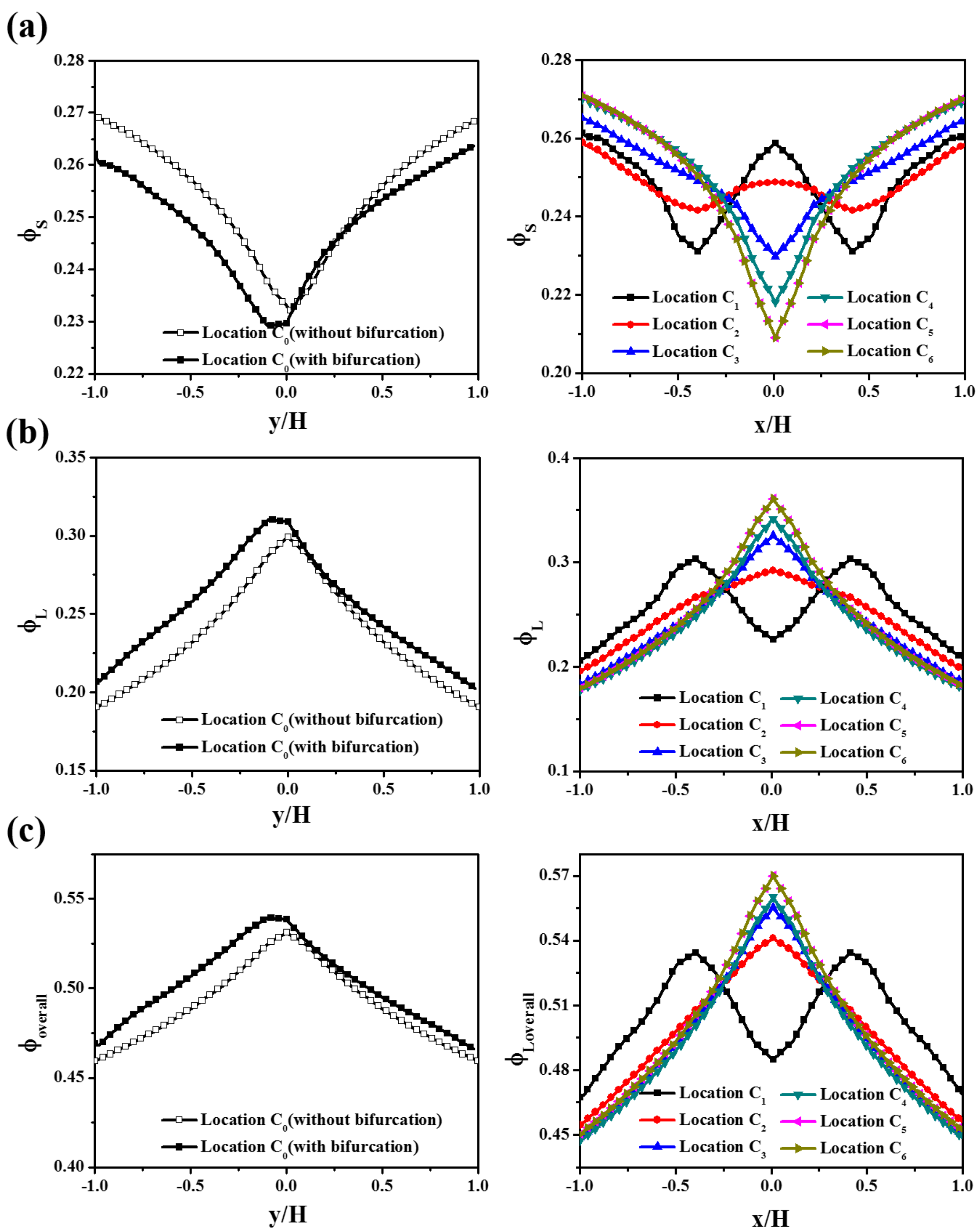

Figure 6.19: Comparison of the concentration profiles of (a) smaller particles, (b) larger particles and (c) overall concentration of bidisperse suspension at different locations in the converging bifurcating channel. The particle sizes were $a_S = 10$ μm and $a_L = 30$ μm.

section. As a result, peak-valley-peak pattern was observed. One interesting observation was that the smaller particles enriched the channel center at location C_2. From the 6.19

it can be observed that the converging of the flow causes the shifting of the concentration peak for the larger particles towards the locations between the channel center and the wall ($y/H = \pm 0.5$) at the entrance of the channel. Since the larger particles populated very less at the channel center, the smaller particles migrate to the center at location C_2. However, the shear-induced migration causes the migration of larger particles to the center. At location C_2, it was observed that both particles migrate to the center. After the location C_2, the interaction of the larger particles causes the size segregation. The concentration of the smaller particles at the channel center gradually decreases and become fully-developed at location C_4. At the very downstream locations, the suspension in the outlet section behaves almost similar to that of suspension in a straight channel. However, as the suspension moves away from the channel entrance, the gradients in the shear-rate and concentration cause the cross-migration of the particles. The species concentration profiles become fully-developed after the location C_5. Since the migration was dominated by the larger particles in the bidisperse suspension, the qualitative nature of the overall particle concentration profile follows the larger particle concentration.

6.4 Closure

We have studied the monodisperse and bidisperse suspension flow through 2D symmetric T-shaped bifurcating channel for diverging and converging flows. The extension of the DFM which was proposed by Kanehl and Stark (2015) has been used to study the shear-induced migration and size segregation of the particles in bidisperse suspension. The model validation has been conducted by comparing our simulations with the experimental results of Semwogerere and Weeks (2008). The model was able to capture the segregation phenomenon observed in the experiments of Semwogerere and Weeks (2008). A thorough study of the effect of the individual particle size and concentration ratio on the size segregation of the particles in bidisperse suspension has been carried out. Irrespective of the size, the particles in monodisperse suspension enriched the channel center. However, this was not the case for bidisperse suspension. It was observed that the relative magnitude of the shear-induced migration and collective diffusion affects the fully-developed concentration profiles of species in the bidisperse suspension. For a suspension composed of an equal concentration of smaller and larger particles, it was observed that the concentration of larger particles enriched the center of the channel. Whereas, the position of concentration peak for the smaller particles depends on the relative size ratio of the particles. It was observed that the faster migration of the larger particles leads to the size segregation. On the other hand, for a suspension composed of an unequal concentration of the species, depending on the size ratio one or both species enrich the channel center. The particles in a bidisperse suspension behaved differently when compared with the particles in monodisperse suspension in the bifurcating channels. In the case of diverging flows, the symmetric concentration profiles in the inlet branch become asymmetric in the daughter branches. The locations of the concentration peak for the smaller particles after the bifurcation were found to strongly depend on the particle size ratio. In the case of converging flows, the two inlet streams merge in the outlet section and the concentration peaks of the individual particles corresponding to the fully-developed profiles from the inlet sections persist for some distance. The evolution of the profiles in the outlet branches was observed to be different for different particle size ratios for both diverging as well as converging flows.

Chapter 7

Concentrated suspension flow in wavy channels

7.1 Problem description

In this chapter, numerical simulations of monodisperse suspension flowing through wavy channels are presented. We have adopted both DFM and SBM to study the shear-induced migration phenomenon. The particles in the simulations are considered to be rigid and neutrally buoyant. Fig. 7.1 shows the geometry considered for investigating the suspension flow in the wavy channels. We have considered two types of 2D wavy channels which are having two different phase lags. The first type of wavy channel also known as a type-1 wavy channel have the phase lag or delay $\theta = 180^0$ and the second type of wavy channel known as a type-2 wavy channel have the phase lag $\theta = 0^0$. The wavy passage consists of 14 waves with an inlet and an outlet section with lengths each equal to that of one wavy section. The schematic representation of the geometry domain and grid is shown in Fig. 7.2. This geometry is an appropriate representation of a practical wavy channel that can be used for applications such as compact heat exchangers or biomedical devices such as blood oxygenators. For the quantitative comparison purpose, the velocity and concentration profiles were drawn at different locations in the channel and these locations were shown in the Fig. 7.2. The inlet velocity has chosen in such a way that the flow is in stokes regime. In all simulations, the magnitude of the inlet velocity was 0.003741 m/s and the particle radius was 10 μm. The flow and particle Reynolds numbers are of the order 10^{-1} and 10^{-3} respectively. It is observed that the fully-developed flow in the wavy channels achieved beyond 7^{th} wave. Thereby, we are reporting the velocity and concentration profiles in wave 9.

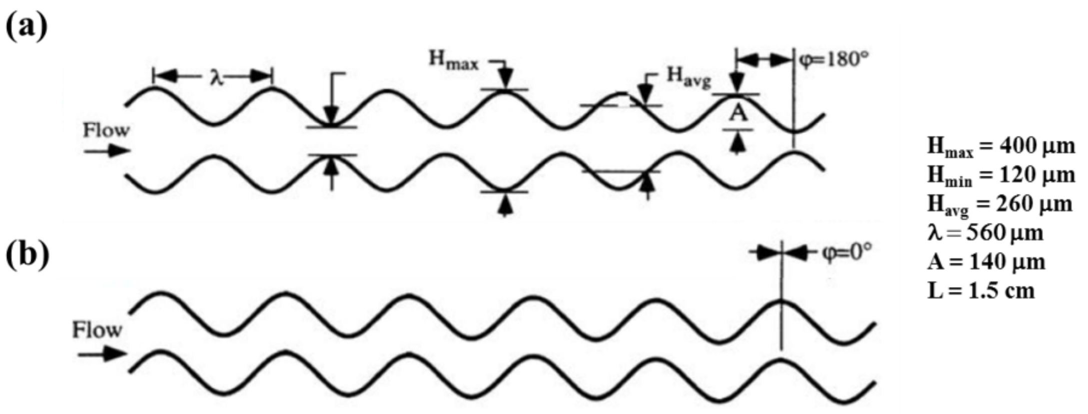

Figure 7.1: Schematic diagram of the computational geometry of (a) type-1, and (2) type-2 wavy channel.

7.2 Results and discussion

7.2.1 Type-1 wavy channel

The numerical results for concentrated suspension flow in a wavy passage are presented in this section. It may be mentioned here that the present study on concentrated suspension flow through a wavy passage aims at investigating the behavior of particle migration. Both DFM and SBM have been used for the simulations in the wavy channel and compared at different locations in the wavy channel. The numerical experiments have been carried out for different average inlet particle concentrations (ϕ_{avg} = 0.2, 0.3, 0.4, and

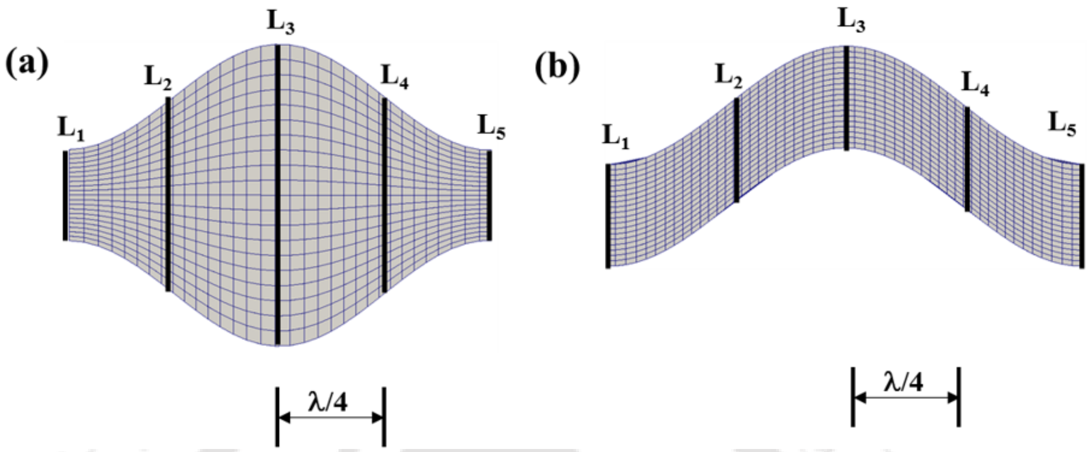

Figure 7.2: Schematic representation of the details of a single wavy section and locations at which the velocity and concentration profiles have been measured. (a) Type-1, and (b) type-2 wavy channel.

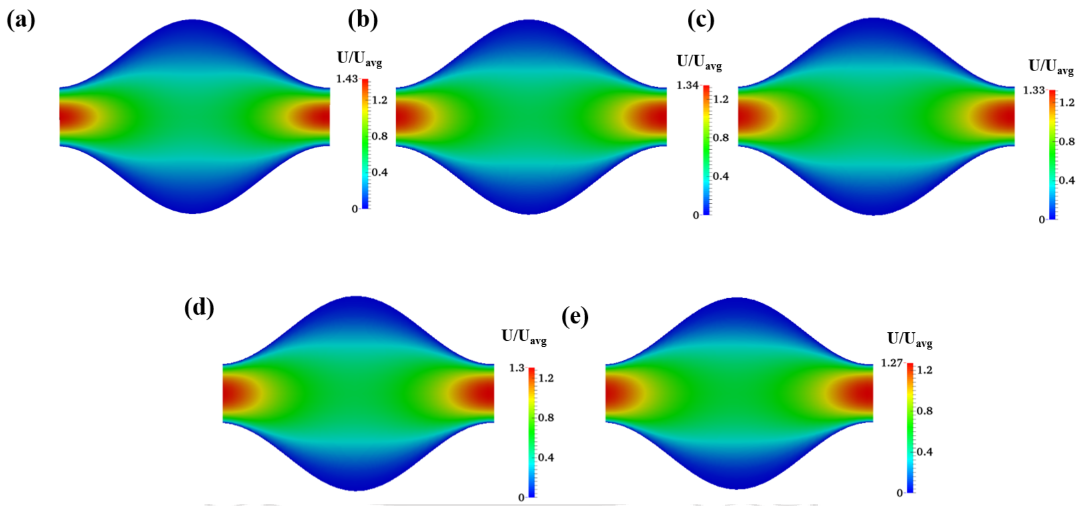

Figure 7.3: Velocity contour planes for (a) $\phi_{avg} = 0$, (b) $\phi_{avg} = 0.2$, (c) $\phi_{avg} = 0.3$, (d) $\phi_{avg} = 0.4$, and (e) $\phi_{avg} = 0.5$ in the type-1 wavy channel.

0.5). To study the impact of the particle phase on the velocity field, simulations were also carried out for the pure carrier fluid without particle phase. The comparison of velocity and shear-rate contours for the pure fluid and suspension for different average inlet particle concentrations (ϕ_{avg} = 0.2, 0.3, 0.4, and 0.5) are shown in Fig. 7.3 and 7.4 respectively. The contours are shown here are obtained from the DFM. The corre-

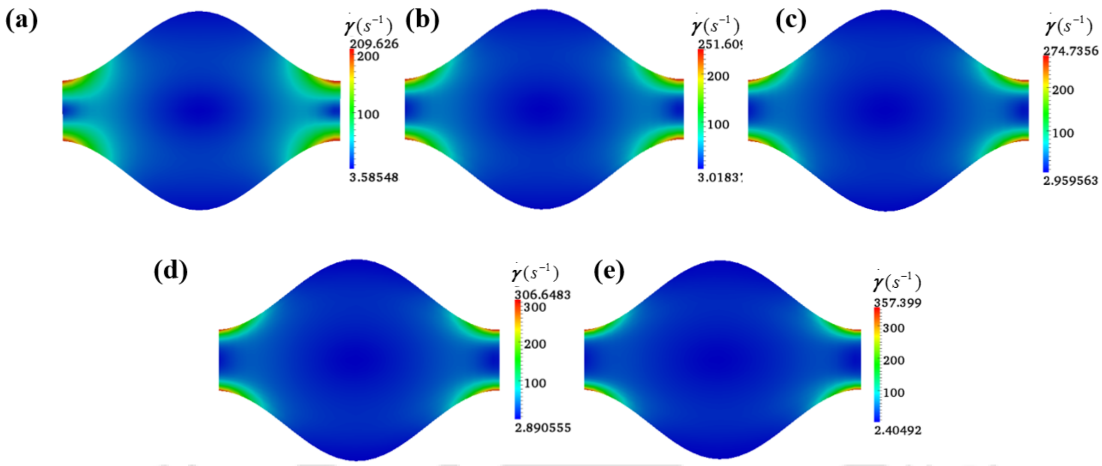

Figure 7.4: Shear-rate contour planes for (a) $\phi_{avg} = 0$, (b) $\phi_{avg} = 0.2$, (c) $\phi_{avg} = 0.3$, (d) $\phi_{avg} = 0.4$, and (e) $\phi_{avg} = 0.5$ in the type-1 wavy channel.

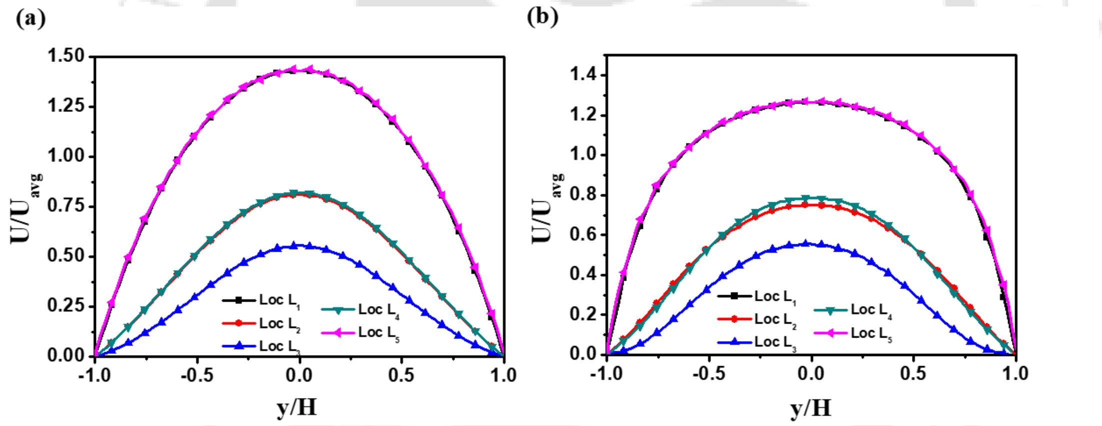

Figure 7.5: Comparison of cross-sectional velocity profiles of (a) pure fluid, and (b) suspension ($\phi_{avg} = 0.5$) flow at different locations in the type-1 wavy channel.

sponding quantitative comparison of pure fluid velocity profiles and shear-rate with the suspension $\phi_{avg} = 0.5$ at different locations in the wave 9 are shown in Fig. 7.5 and Fig. 7.6 respectively. It is observed from the Figs. 7.3 and 7.4, the velocity has a maximum value at the minimum cross-section of the geometry, that is, at the entry to a wavy section. This is due to a sudden reduction in the flow area. As we move further downstream, the centreline velocity of suspension is considerably blunted, as compared with the Newtonian flow velocity profile. The region downstream of the constricted portion

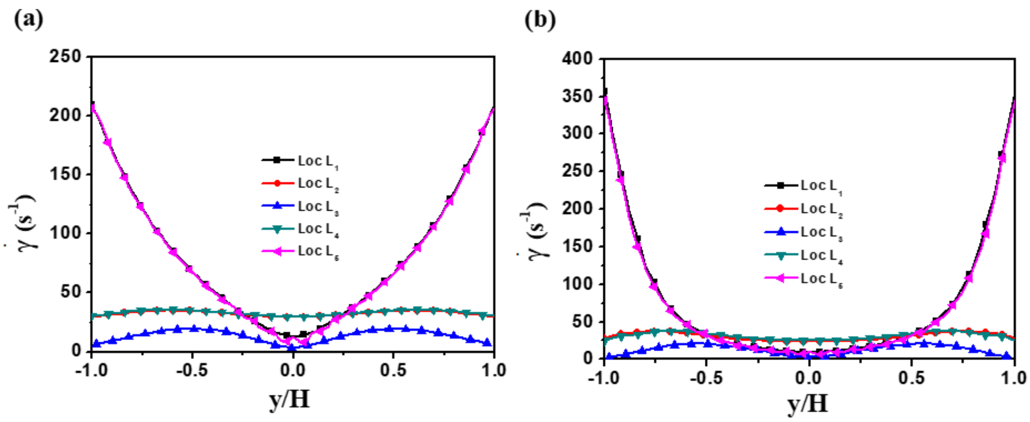

Figure 7.6: Comparison of cross-sectional shear-rate profiles of (a) pure fluid, and (b) suspension ($\phi_{avg} = 0.5$) flow at different locations in the type-1 wavy channel.

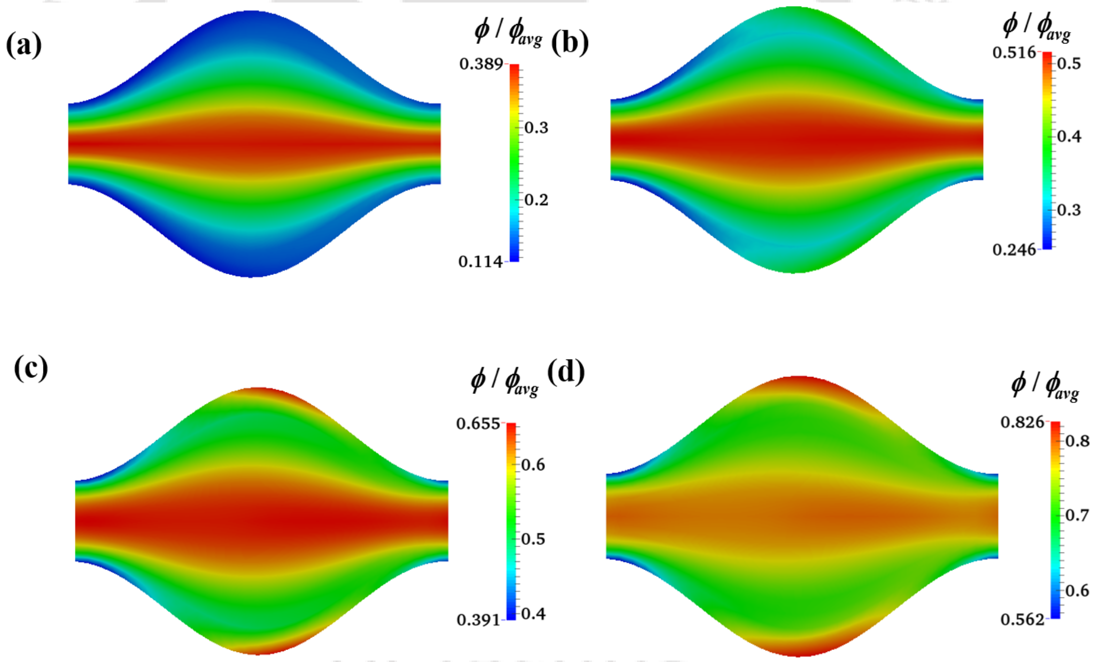

Figure 7.7: Particle concentration contour planes for (a) $\phi_{avg} = 0.2$, (b) $\phi_{avg} = 0.3$, (c) $\phi_{avg} = 0.4$, and (d) $\phi_{avg} = 0.5$ in the type-1 wavy channel.

is subject to low velocities in the central region as compared with that in the region of area reduction. The degree of bluntness strongly depends on the particle concentration. As the particle concentration increases, the bluntness in the velocity profiles increases. At the site of the minimum area of cross-section, the shear-rate is higher at the wall

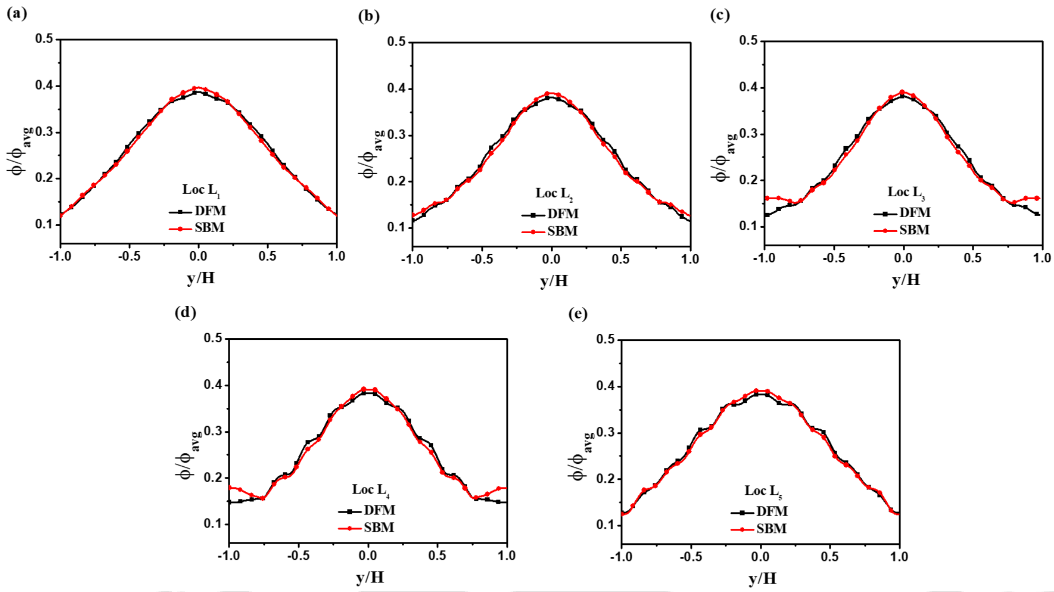

Figure 7.8: Particle concentration profiles at different locations in the type-1 wavy channel obtained from DFM and SBM for $\phi_{avg} = 0.2$. At (a) location L_1, (b) location L_2, (c) location L_3, (d) location L_4, and (e) location L_5.

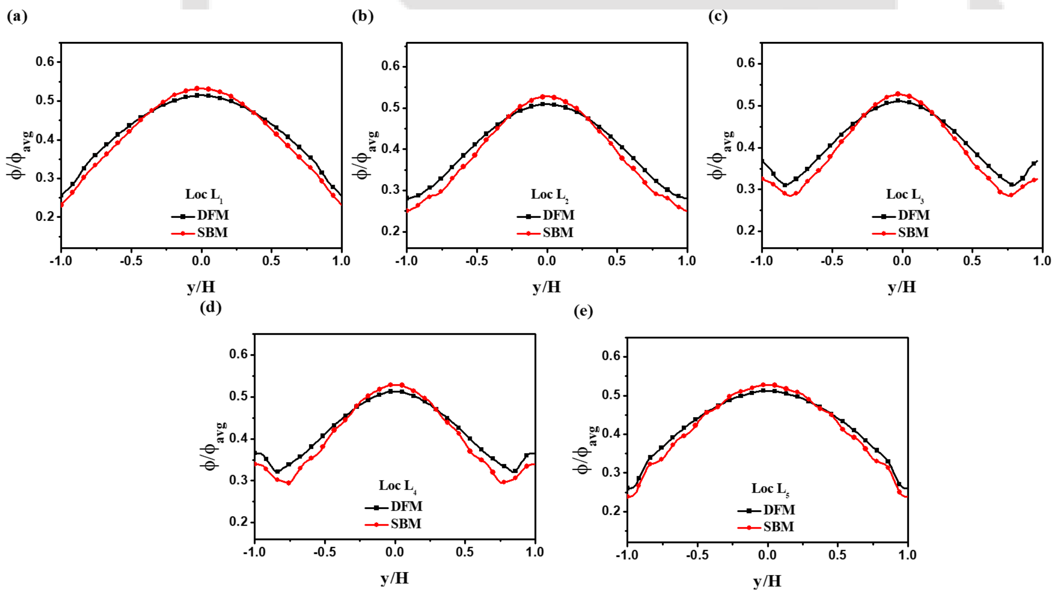

Figure 7.9: Particle concentration profiles at different locations in the type-1 wavy channel obtained from DFM and SBM for $\phi_{avg} = 0.3$. At (a) location L_1, (b) location L_2, (c) location L_3, (d) location L_4, and (e) location L_5.

leading to the migration of the particles from the wall towards the inner section of the geometry (see Figs. 7.5 & 7.6).

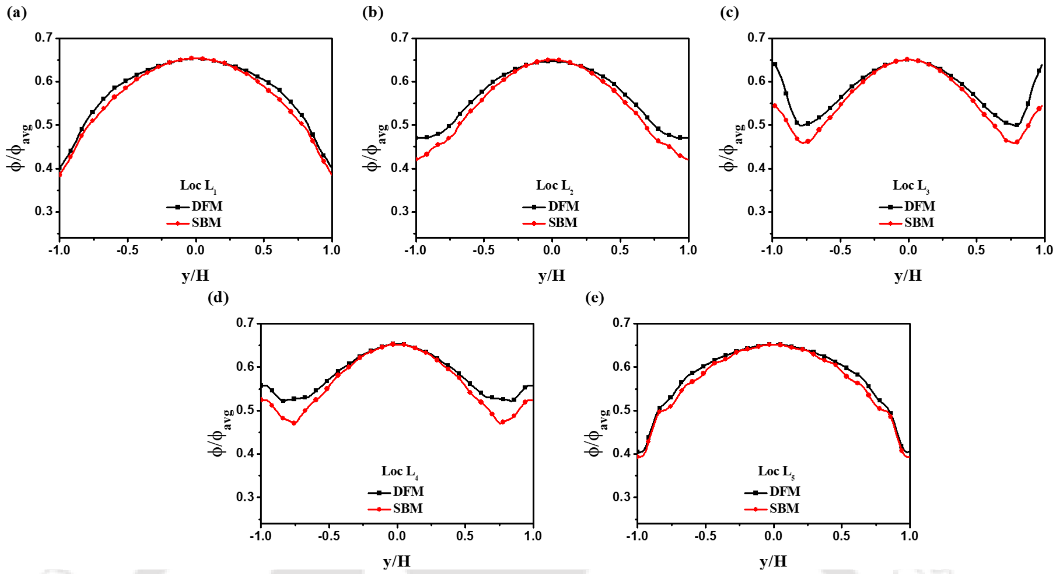

Figure 7.10: Particle concentration profiles at different locations in the type-1 wavy channel obtained from DFM and SBM for $\phi_{avg} = 0.4$. At (a) location L_1, (b) location L_2, (c) location L_3, (d) location L_4, and (e) location L_5.

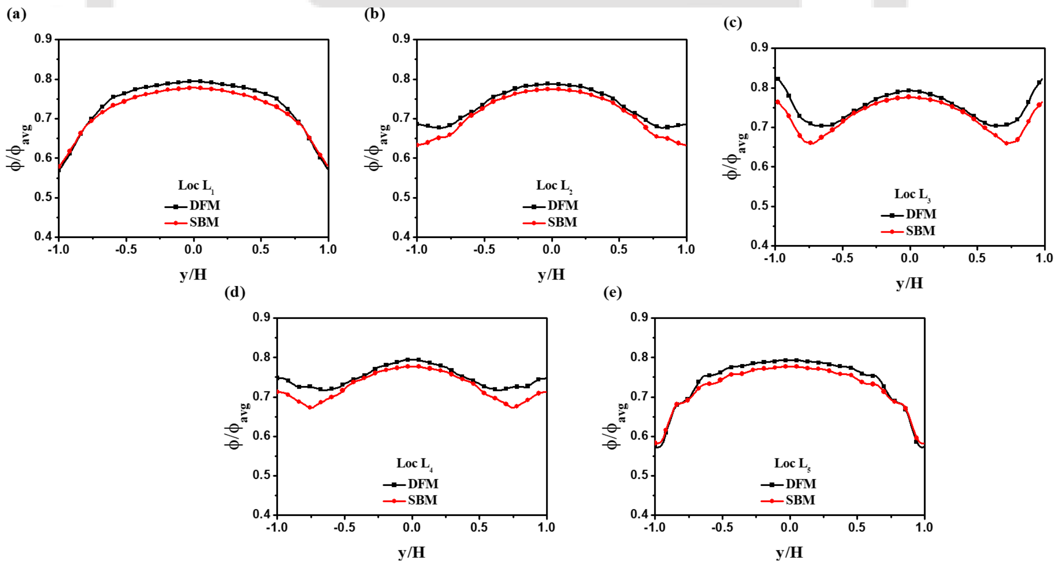

Figure 7.11: Particle concentration profiles at different locations in the type-1 wavy channel obtained from DFM and SBM for $\phi_{avg} = 0.5$. At (a) location L_1, (b) location L_2, (c) location L_3, (d) location L_4, and (e) location L_5.

The comparison of the particle concentration contour planes for different average inlet particle concentrations (ϕ_{avg} = 0.2, 0.3, 0.4, and 0.5) are shown in Fig. 7.7. The corresponding quantitative comparison of the concentration profiles obtained by using DFM and SBM at various locations are shown in Figs. 7.8, 7.9, 7.10, and 7.11 for $\phi_{avg} =$ 0.2, 0.3, 0.4, and 0.5 respectively. At the site of the minimum area of cross-section, the shear-rate is higher at the wall leading to the migration of the particles from the walls toward the inner section of the geometry. The concentration at these higher shear-rate regions is low compared with the center of the channel. The region downstream of the constricted portion is subject to low velocities in the central region as compared with that in the region of area reduction. Particle concentration increases slightly in this zone as compared with that in the region of area reduction. The contour plots for the particle concentration in Fig. 7.7 show that the particles migrate out of high shear zones and concentrate in the low shear regions at the centreline and in a very narrow region near bottom and top trough of the wave. The bottom and top trough of the wavy channel corresponds to a region of low shear-rate, and consequently, a locally high concentration of particles is developed near this region closer to the wall. This is due to large changes in the viscosity and its gradients as a result of small changes in the particle concentration. The enriching of the particles at these locations strongly depends on the average bulk particle concentration. The flux which is responsible for the shear-induced migration has the components of the gradient in shear-rate and particle concentration (viscosity gradient). These two fluxes have the opposite effects and relative magnitude will decide the position of the particle. The shear-rate gradient leads the particles to migrate from high shear-rate regions to low shear-rate regions. On the other hand, the gradient in the viscosity leads to the movement of particles from high concentrated regions to low concentrated regions. For the low particle concentrations, the gradient in the shear-rate dominates over the gradient in the concentration. This effect can be understood from the Figs. 7.8 - 7.11. At location L_3, the concentration at the walls for suspension with $\phi_{avg} = 0.2$ is low when compared with suspension of $\phi_{avg} = 0.5$. As the suspension moves from the constricted portion (Location L_1) to the downstream locations of the channel, the velocity decreases and the shear-rate profile shows peak-valley-peak pattern across the channel. Thereby, the particles decelerate from center regions towards the bottom and top trough. The concentration at these locations is very high for suspension of ϕ_{avg} = 0.5 when compared with ϕ_{avg} = 0.2. The results show that the findings of the two models are almost similar.

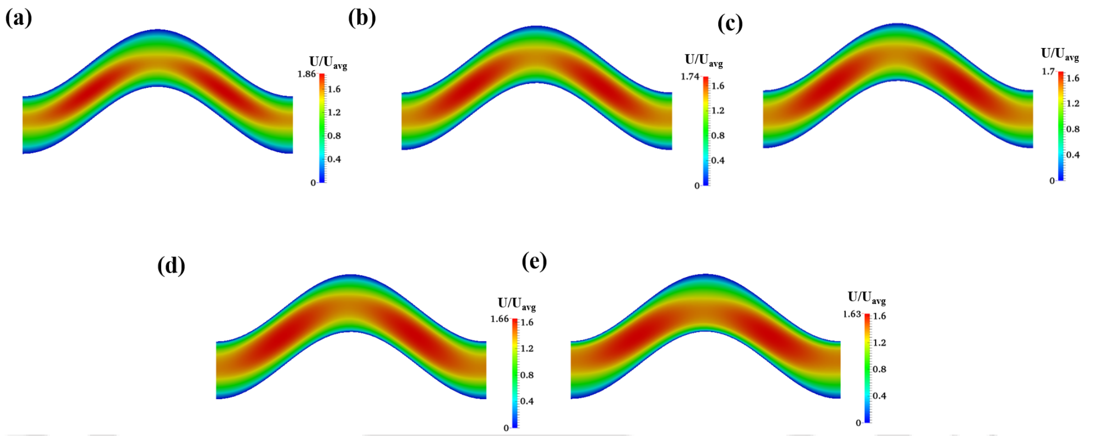

Figure 7.12: Velocity contour planes for (a) $\phi_{avg} = 0$, (b) $\phi_{avg} = 0.2$, (c) $\phi_{avg} = 0.3$, (d) $\phi_{avg} = 0.4$, and (e) $\phi_{avg} = 0.5$ in the type-2 wavy channel.

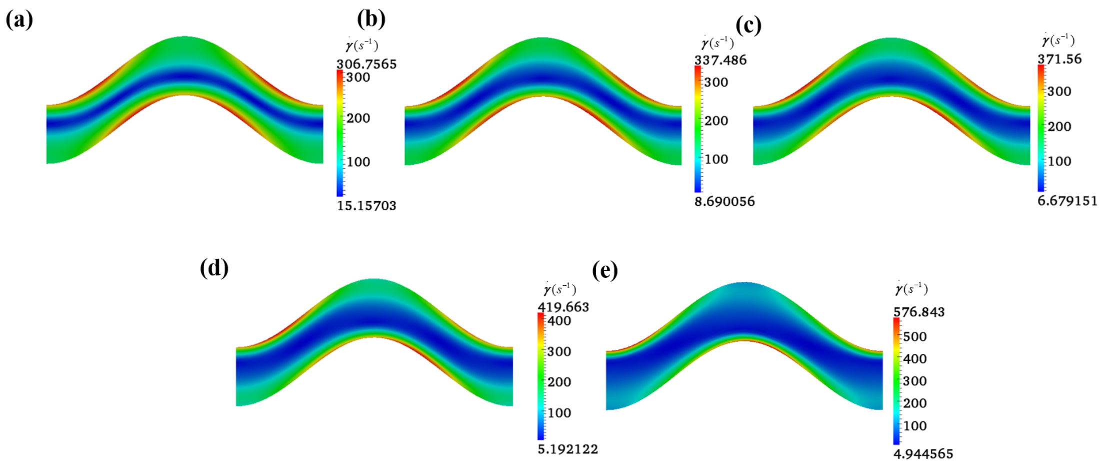

Figure 7.13: Shear-rate contour planes for (a) $\phi_{avg} = 0$, (b) $\phi_{avg} = 0.2$, (c) $\phi_{avg} = 0.3$, (d) $\phi_{avg} = 0.4$, and (e) $\phi_{avg} = 0.5$ in the type-2 wavy channel.

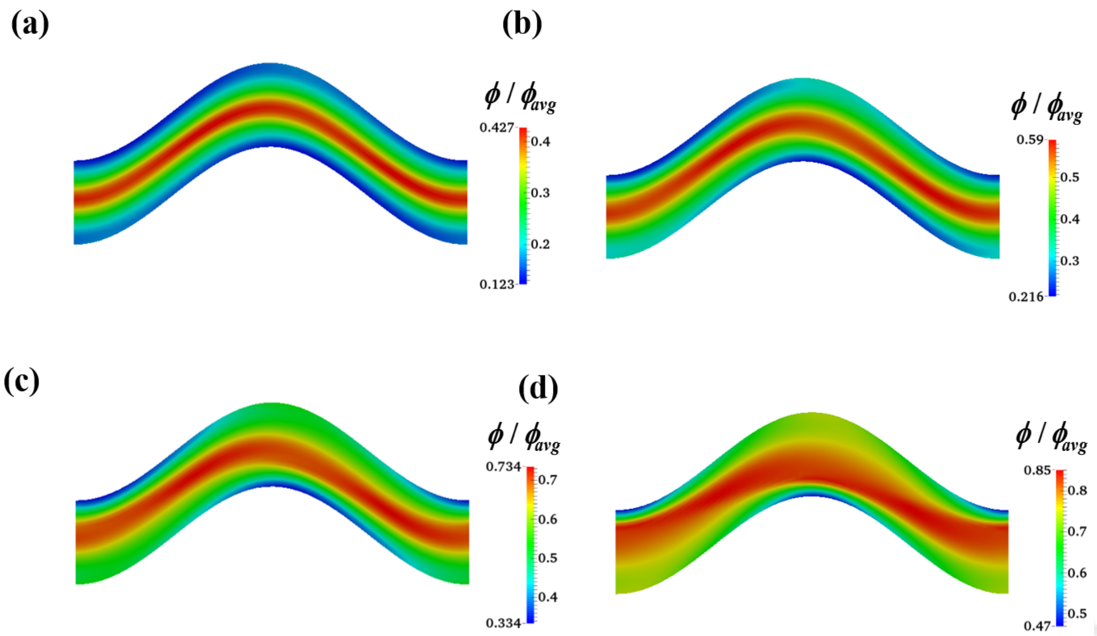

Figure 7.14: Particle concentration contour planes for (a) $\phi_{avg} = 0.2$, (b) $\phi_{avg} = 0.3$, (c) $\phi_{avg} = 0.4$, and (d) $\phi_{avg} = 0.5$ in the type-2 wavy channel.

7.2.2 Type-2 wavy channel

The comparison of velocity and shear-rate contours for the pure fluid and suspension in the type-2 wavy channel for different average inlet particle concentrations ($\phi_{avg} = 0.2$, 0.3, 0.4, and 0.5) are shown in Fig. 7.12 and 7.13 respectively. The suspension flow in channel shows blunted velocity profiles when compared with pure fluid. Moreover, the bluntness is observed to vary with the bulk particle volume fraction. The suspension with bulk particle volume fraction $\phi_{avg} = 0.5$, shows more bluntness in the velocity profiles. As the particle concentration increases, the shear-rate near the channel walls increases gradually and in turn, affects the distribution of the particles in the channel.

Fig. 7.14 show the contour planes of particle concentration in the channel for different average inlet particle concentrations ($\phi_{avg} = 0.2$, 0.3, 0.4, and 0.5). The flow of suspension in the inlet section causes the enrichment of the particles at the channel center. As the suspension enters into the wavy section, the effect of curvature in the

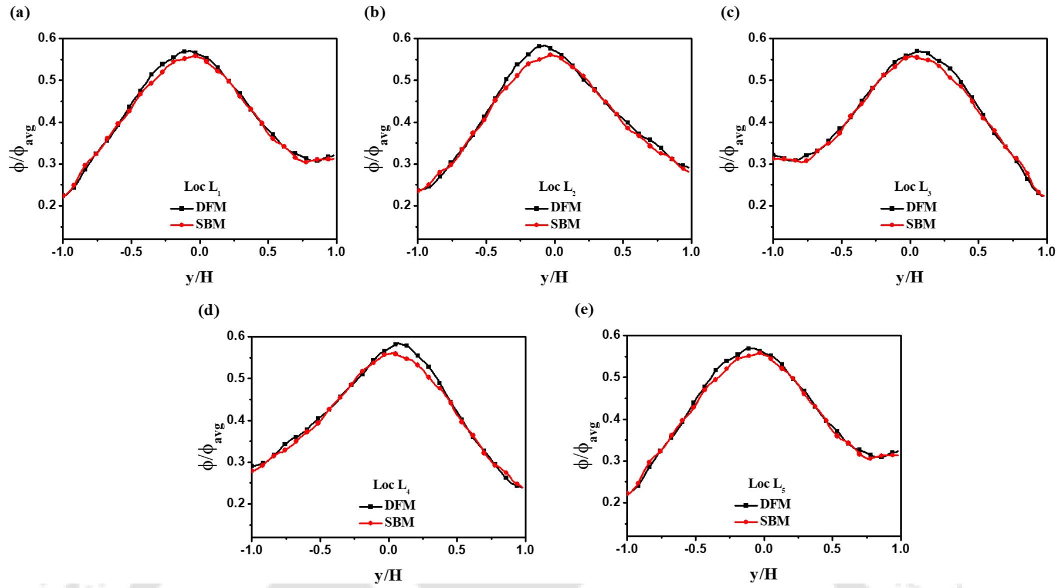

Figure 7.15: Particle concentration profiles at different locations in the type-1 wavy channel obtained from DFM and SBM for $\phi_{avg} = 0.3$. At (a) location L_1, (b) location L_2, (c) location L_3, (d) location L_4, and (e) location L_5.

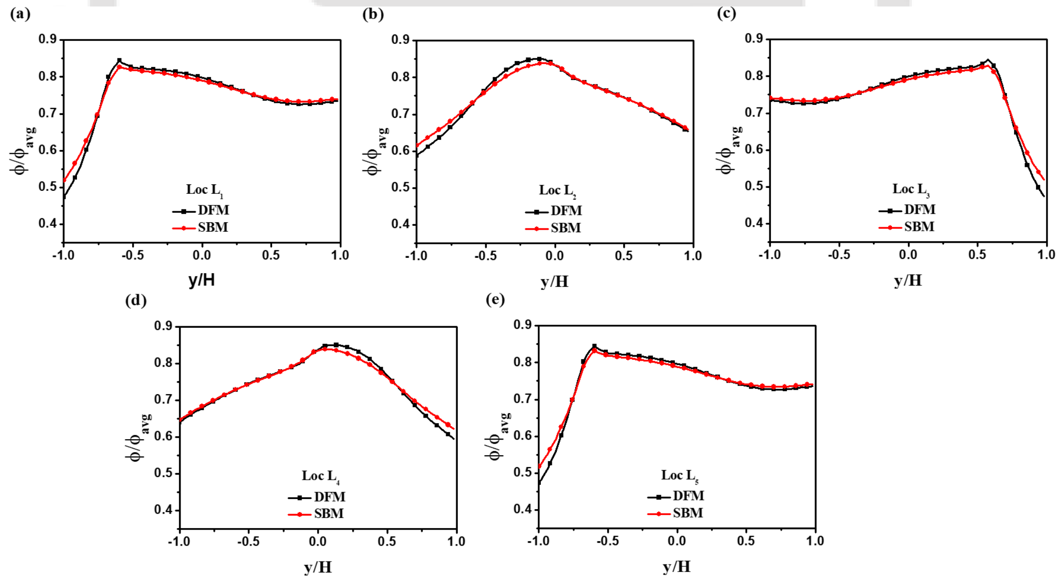

Figure 7.16: Particle concentration profiles at different locations in the type-2 wavy channel obtained from DFM and SBM for $\phi_{avg} = 0.5$. At (a) location L_1, (b) location L_2, (c) location L_3, (d) location L_4, and (e) location L_5.

streamlines begin on the particle distribution. Figs. 7.15 and 7.16 show the quantitative comparison of the concentration profiles at different locations in the channels for $\phi_{avg} =$

0.3 and 0.5 respectively. The symmetric profiles in the inlet section become asymmetric as the suspension flows in the wavy passage. Moreover, the asymmetry increases with particle volume fraction. As the suspension reaches the location L_3, a sudden turn in the flow causes the migration of particles toward the low curvature streamline region (i.e towards the upper wall of the channel). The results show that the findings of the SBM and DFM are very similar.

7.3 Closure

The particle migration in the flow of concentrated suspension in the spatially modulated channels has been investigated numerically by using DFM and SBM. The results demonstrate strong particle migration towards the center of the channel and an increasing blunting of velocity profiles with increase in average bulk particle concentration. In the case of the type-1 wavy channel, the accumulation of particle concentration in the recirculation zones gradually increases with bulk particle volume fraction. The results of SBM and DFM are consistent with each other.

Chapter 8

Conclusions and prospectives.

8.1 Conclusions

This thesis covers the flow physics of non-Brownian suspensions of mono and bidispersed rigid particles suspended in Newtonian and non-Newtonian carriers at very low Reynolds number. The central point is the phenomenon of shear-induced migration of particles and its predictions using continuum models. A detailed summary of this thesis can be achieved now by grouping all the closures of the chapters as the following:

- In the chapter 1, we have seen the different viscosity models available in the literature for the dilute and dense particulate suspension followed by the available experimental literature on the intriguing phenomenon shear-induced particle migration.

- The continuum models for mono and bidispersed rigid particles available in the literature has been described in chapter 2 in a simplified clear manner. However, a detailed description of these models can be found in the literature.

- In chapter 3, we explained the implementation of the mathematical models in the OpenFOAM® environment, and their validity with available experimental data.

- In the chapter 4, the simulations of monodispersed suspension flow in the 3D oblique bifurcating channel have been carried out. The particles considered was non-colloidal, mono-dispersed and neutrally buoyant in the Stokes regime suspended in a Newtonian carrier fluid. The velocity and particle concentration profiles were reported by using DFM and SBM. The effect of orientation of the geometry on fluid and particle partitioning was reported. The suspension fluid velocity profiles showed a marked difference over the pure carrier fluid profiles and greatly depends on the orientation of the geometry (bifurcation angle). After the bifurcation, the velocity and concentration profiles become asymmetric and the degree of asymmetry depends on the bifurcation angle. As the bifurcation angle increases, the dividing streamline shifts towards the side branch and suspension shows slightly different behavior over pure carrier fluid. The partitioning of the particles does not follow the fluid partitioning. The findings of DFM and SBM were very similar. The results which we have shown are useful in the microfluidics.

- In the chapter 5, the effect carrier fluid rheology on the shear-induced particle migration in an asymmetric T-shaped bifurcating channel had been reported. The DFM with modified diffusivity coefficients (K_c and K_η) was used to compute the velocity and concentration profiles for non-Newtonian carrier suspensions and the results for Newtonian, shear-thinning, and shear-thickening fluids were compared. Suspensions in non-Newtonian carrier fluid exhibited a marked difference in the velocity and concentration fields compared to those in Newtonian carriers. The power-law constitutive model results were compared with Bird-Carreau constitutive model of the carrier fluid and the findings of two models were in good agreement. The simulations were also carried out for carrier fluid without particle phase to investigate the effect of particle phase on the velocity profiles. The presence of the particles and the resulting shear-induced migration led to the blunted velocity profiles. Though the partitioning of the particles follows the same trend as that of fluid, we observed a significant quantitative difference between the two. Very less deviation in fluid-particle partitioning between the daughter branches was observed in the shear-thickening case. On the other hand, the highest deviation was observed in the case of shear-thinning. Therefore, shear-thinning fluid can be more useful for the separation/fractionation of the suspended particles from the bulk suspension in many microfluidic and industrial applications.

- Chapter 6, has presented the monodisperse and bidisperse suspension flow through 2D symmetric T-shaped bifurcating channel for diverging and converging flows. The extension of DFM which was proposed by Kanehl and Stark (2015) has been used to study the shear-induced migration and size segregation of the particles in bidisperse suspension. A thorough study of the effect of the individual particle size and concentration ratio on the size segregation of the particles in bidisperse suspension has been carried out. Irrespective of the size, the particles in monodisperse suspension enriched the channel center. However, this was not the case for bidisperse suspension. It was observed that the relative magnitude of the shear-induced migration and collective diffusion affects the fully-developed concentration profiles of species in the bidisperse suspension. For a suspension composed of an equal concentration of smaller and larger particles, it was observed that the concentration of larger particles enriched the center of the channel. Whereas, the position of concentration peak for the smaller particles depends on the relative size ratio of the particles. It was observed that the faster migration of the larger particles leads to the size segregation. On the other hand, for a suspension composed of an unequal concentration of the species, depending on the size ratio one or both species enrich the channel center. The particles in a bidisperse suspension behaved differently when compared with the particles in monodisperse suspension in the bifurcating channels. In the case of diverging flows, the symmetric concentration profiles in the inlet branch become asymmetric in the daughter branches. The locations of the concentration peak for the smaller particles after the bifurcation were found to strongly depend on the particle size ratio. In the case of converging flows, the two inlet streams merge in the outlet section and the concentration peaks of the individual particles corresponding to the fully-developed profiles from the inlet sections persist for some distance. The evolution of the profiles in the outlet branches was observed to be different for different particle size ratios for both diverging as well as converging flows.

- The final chapter 7 provides the flow of concentrated suspension in the wavy channels. The DFM and 2D frame-invariant SBM were employed for the suspension flow. Two types of wavy channels have been considered with a phase lag $\theta = 180^0$ and 0^0. The effect of particle concentration on the velocity profiles was studied.

8.2 Perspectives

The experiments need to be carried out for the concentrated bidisperse suspension in the complex bifurcations. None of the experimental studies in the literature reported the effect of viscoelastic carrier fluid rheology on the microstructure of the particles. It would be of interest to carry out the experiments in this regard.

It will be so interesting in the near future to continue the simulations for conjugate heat-transfer and shear-induced migration in concentrated suspension flows through bifurcations. The results that were presented in this thesis limited to the very low Reynolds number flows ($Re \ll 1$). One can add inertial effects to the continuum models. On the other hand, it would be of interest to carry out meso-scale simulations such as the Lattice-Boltzmann method (LBM) for the suspension flow at high Reynolds number through complex bifurcations.

Appendices

Appendix A

Implementation of general transport equation in OpenFOAM®

The general transport can be written as:

$$\frac{\partial \phi}{\partial t} + \boldsymbol{U}.\nabla\phi = \nabla.(\Gamma\nabla\phi) + S_\phi \tag{A.1}$$

In OpenFOAM® notation the above equation can be written as:

```
solve
(
    fvm::ddt(ϕ)
  + fvm::div(phi, ϕ)
  - fvm::laplacian(Γ, ϕ)
  ==
    fvc::Sp(S_ϕ)
);
```

Appendix B

Implementation of the SIMPLE algorithm in OpenFOAM®

The SIMPLE algorithm can be implemented in OpenFOAM® as follows (The complete implementation of the algorithm can be seen in the source code of the simpleFoam solver provided with OpenFOAM®):

- Store the pressure calculated at the previous iteration, because it is required to apply under-relaxation

  ```
  p.storePrevIter();
  ```

- Define the equation for U

  ```
  tmp<fvVectorMatrix> UEqn
  (
      fvm::div(phi, U) - fvm::laplacian(nu, U)
  );
  ```

  "tmp< > is used to reduce peak memory."

- Under-relax the equation for U

  ```
  UEqn.relax();
  ```

- Solve the momentum predictor

  ```
  solve (UEqn == -fvc::grad(p));
  ```

- Update the boundary conditions for p

  ```
  p.boundaryField().updateCoeffs();
  ```

- Calculate the a_p coefficient and calculate U

  ```
  volScalarField AU = UEqn().A();
  U = UEqn().H()/AU;
  UEqn.clear();
  ```

- Calculate the flux

  ```
  phi = fvc::interpolate(U) & mesh.Sf();
  adjustPhi(phi, U, p);
  ```

- Define and solve the pressure equation and repeat for the prescribed number of non-orthogonal corrector steps

  ```
  fvScalarMatrix pEqn
  (
      fvm::laplacian(1.0/AU, p) == fvc::div(phi)
  );
  pEqn.setReference(pRefCell, pRefValue);
  pEqn.solve();
  ```

- Correct the flux

  phi -= pEqn.flux();

- Calculate continuity errors

  # include "continuityErrs.H"

- Under-relax the pressure for the momentum corrector and apply the correction

  p.relax();

  U -= fvc::grad(p)/AU;

  U.correctBoundaryConditions();

- Check for convergence and repeat from the beginning until convergence criteria are satisfied.

  Note: In OpenFOAM 1.6. and 1.6.x the convergence check has been implemented in simpleFoam by defining

  eqnResidual: Initial residual of the equation

  maxResidual: Maximum residual of the equations after one solution step

  convergenceCriterion: Convergence criterion specified by the user

- The value of the initial residual can be obtained when solving the corresponding equation using the initialResidual() method. Two syntax are possible:

  eqnResidual = solve

  (

  UEqn() == -fvc::grad(p)

).initialResidual();

  or, equivalently, for the pressure equation, since it has been already defined,

  eqnResidual = pEqn.solve().initialResidual();

Appendix C

Schemes used in OpenFOAM® for the different simulation cases

The different discretization schemes, solvers and relaxation factors used in OpenFOAM® solver setting are described in the following sections.

C.1 The schemes used in OpenFOAM® in this work for different simulation cases

```
gradSchemes
{
    default Gauss linear;
}

divSchemes
{
    default Gauss linear;
}
```

```
laplacianSchemes
{
    default Gauss linear corrected;
}

interpolationSchames
{
    default linear;
}

snGradSchemes
{
    default corrected;
}
```

C.2 Solvers settings used in OpenFOAM® in this work for different simulation cases

```
solvers
{
    p
    {
      solver PCG;
      preconditioner DILU;
      tolerance 1e-10;
      relTol 0.05;
```

```
    }

    U
    {
        solver PCG;
        preconditioner DIC;
        tolerance 1e-09;
        relTol 0.1;
    }

    ϕ
    {
        solver PBiCG;
        preconditioner DILU;
        tolerance 1e-09;
        relTol 0.05;
    }
}

SIMPLE
{
    nCorrectors 2; // minimum 2
    nNonOrthogonalCorrectors 2;
    pRefCell 0;
    pRefValue 0;
}
```

```
relaxationFactors
{
    p 0.2;
    U 0.5;
    φ 0.5;
}
```

C.3 References

1. J. H. Ferziger, M. Peric, Computational Methods for Fluid Dynamics, Springer, 3rd Ed., 2001.

2. H. Jasak, Error Analysis and Estimation for the Finite Volume Method with Applications to Fluid Flows, Ph.D. Thesis, Imperial College, London, 1996.

Appendix D

Code implementation procedure inside the transientSimpleFoam

The following gives the brief description of the code implementation procedure inside the transientSimpleFoam solver:

```
int main(int argc, int *argv[])
{
    info <<"\nStarting time loop\n" << endl;
    for (runTime++; !runTime.end(); runTime++)
    {
        #include "readPISOControls.H"
        #include "CourantNo.H"
```

Calculating parameters: η_s, $\boldsymbol{E}$, $\dot{\gamma}$, $\boldsymbol{\Sigma}$, $\boldsymbol{N_t}$, etc...

```
        // Pressure-velocity SIMPLE corrector
        for (int corr=0; corr<nCorr; cor++)
        {
```

solve steady Stokes momentum: $\nabla.\boldsymbol{\Sigma} = 0$;

velocity-pressure correction to satisfy continuity $\nabla.\boldsymbol{U} = 0$.

}

At each time step solve transport equation

$\frac{\partial \phi}{\partial t} + \boldsymbol{U}.\nabla\phi = -\nabla.\boldsymbol{N_t}$ to get new ϕ

runTime.write();

}

}

Appendix E

Mesh generation in OpenFOAM®

This section describes the mesh generation utility, *blockMesh*, supplied with OpenFOAM®. The mesh is generated from a dictionary file names *blockMeshDict* located in *constant/polyMesh* directory of a case. *blockMesh* reads this dictionary, generates the mesh and writes out the mesh data to *points* and *faces*, *cells* and *boundary* files in the same directory. The principle behind *blockMesh* is to decompose the domain geometry into a set of 1 or more three dimensional, hexahedral blocks. Edges of the blocks can be straight lines, arcs or splines. The mesh is ostensibly specified as a number of cells in each direction of the block, sufficient information for blockMesh to generate the mesh data.44 Each block of the geometry is defined by 8 vertices, one at each corner of a hexahedron. The vertices are written in a list so that each vertex can be accessed using its label, remembering that OpenFOAM® always uses the C++ convention that the first element of the list has label '0'. An example block is shown in Fig. E.1 with each vertex numbered according to the list.

Each block has a local coordinate system (x, y, z) that must be right-handed. The local coordinate system is defined by the order in which the vertices are presented in the block definition according to:

- the axis origin is the first entry in the block definition, vertex 0 in our example;

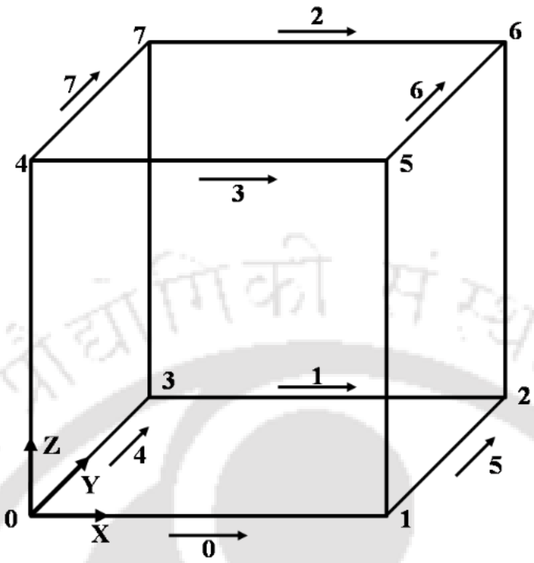

Figure E.1: A single block.

- the x direction is described by moving from vertex 0 to vertex 1;
- the y direction is described by moving from vertex 1 to vertex 2;
- vertices 0, 1, 2, 3 define the plane $z = 0$;
- vertex 4 is found by moving from vertex 0 in the direction;
- vertices 5, 6 and 7 are similarly found by moving in the z direction from vertices 1, 2 and 3 respectively.

Below is an example set of entries from the blockMeshDict dictionary required for the geometry creation.

```
convertToMeters 0.1;

vertices
(
    (0 0 0)
    (1 0 0)
```

```
        (1 1 0)
        (0 1 0)
        (0 0 0.1)
        (1 0 0.1)
        (1 1 0.1)
        (0 1 0.1)
);

blocks
(
        hex (0 1 2 3 4 5 6 7) (20 20 1) simpleGrading (1 1 1)
);

edges
(
);

boundary
(
        movingWall
        {
            type wall;
            faces
            (
                    (3 7 6 2)
            );
        }
```

```
    fixedWalls
    {
        type wall;
        faces
        (
            (0 4 7 3)
            (2 6 5 1)
            (1 5 4 0)
        );
    }
    frontAndBack
    {
        type empty;
        faces
        (
            (0 3 2 1)
            (4 5 6 7)
        );
    }
);

mergePatchPairs
(
);
```

Appendix F

The 2D frame-invariant modified suspension balance model

The formulation of the SBM presented in the Chapter 2 is applicable to cases of simple shear flows of non-Brownian suspensions. This limitation on the use of the model is due to its formulation in a coordinate system that requires its axes to be aligned with the flow, velocity gradient, and vorticity directions. If the model is to be used for two-phase suspensions in general geometries, where the flow is not necessarily of the simple shear type, it requires modifications. Following the efforts of Miller et al. (2009) and Dbouk et al. (2013) the process of developing a two-dimensional frame-invariant version of the modified SBM presented here.

F.1 Frame-invariant suspension kinematics

The suspension flow kinematics represents the local motion or behavior that a local zone of the suspension (fluid-particles) may undergo. It is the zone where the particles immersed in the fluid may be going away from each other, approaching each other, colliding, or even rolling over each other aligning in a preferred position by the flow between both the compression and the tension axes. Therefore, in the general flow of a suspension, the local kinematics can vary between pure extension and solid-body rotation, with simple shear representing an equal balance between them. Brady and Morris (1997) and Morris and Katyal (2002) related the appearance of shear-induced normal stresses in suspensions to the breaking of fore-aft symmetry of the pair-particle microstructure. Since this symmetry is expressed in terms of the driving flow, it is essential to relate the particle stress Σ^p to the local kinematics of the flow.

F.1.1 Kinematic ratio

The local kinematics of the suspension is characterized by the local material deformation rate ($\dot{\gamma}$) and the relative rotation (ω_{rel}) defined as:

$$\dot{\gamma}. = \sqrt{2\boldsymbol{E} : \boldsymbol{E}}, \tag{F.1}$$

$$\omega_{rel} = \frac{\omega}{2} - \boldsymbol{W}, \tag{F.2}$$

where $\boldsymbol{E}$ is the rate of strain tensor, ω the local vorticity ($\omega = \nabla \times \boldsymbol{U}$) and ($\frac{\omega}{2}$) the local angular velocity of a fluid element, and $\boldsymbol{W}$ the local rotation of the axes of the rate of strain given by

$$\boldsymbol{W} = e_i \times \frac{\partial e_i}{\partial t} + \boldsymbol{U}.\nabla e_i, \tag{F.3}$$

In Eq. (F.3) $\boldsymbol{e}_i$ is an eigenvector corresponding to an eigenvalue ($\wedge_i$) of $\boldsymbol{E}$ satisfying

$$(\boldsymbol{E} - \wedge_i).\boldsymbol{e}_i = 0, \tag{F.4}$$

Since both (ω_{rel}) and $\boldsymbol{W}$ are calculated using the same frame of reference, their difference (ω_{rel}) produces a frame invariant measure of rotation. Moreover, as the interest here is in quasi-stationary flows, the term ($\frac{\partial e_i}{\partial t}$)in Eq. (F.3) is neglected. Furthermore, these two local kinematic effects($\dot{\gamma}$ and ω_{rel}) are accounted for through a single kinematic ratio

($\hat{\rho_k}$), which, following Ryssel and Brunn (1999), is defined as

$$\hat{\rho_k} = \frac{2\omega_{rel}}{\dot{\gamma} + \omega_{rel}}, \tag{F.5}$$

Eq. (F.10) indicates that $\hat{\rho_k}$ varies between 0 and 2 according to the flow local kinematic state. For a flow in pure extension $\hat{\rho_k}$=0 (ω_{rel}=0), in simple shear $\hat{\rho_k}$=1 ($\omega_{rel} = \frac{\dot{\gamma}}{2}$), and in solid body rotation $\hat{\rho_k}$=2 ($\dot{\gamma} = 0$).

F.1.2 Compression-tension coordinates and transition matrix

To represent the stress in terms of local kinematics in two dimensional situations, the eigenvectors $\boldsymbol{e}_i$ are defined as the principal axes of the rate of the strain tensor $\boldsymbol{E}$, where the subscript i≡t stands for the tension axis corresponding to the positive eigenvalue of $\boldsymbol{E}$ ($\wedge_{i\equiv t}$>0), and i≡c for the compression axis corresponding to the negative eigenvalue of $\boldsymbol{E}$ ($\wedge_{i\equiv t}$<0). Consequently, the transformation relation that maps the general Cartesian system $(\boldsymbol{e}_x, \boldsymbol{e}_y, \boldsymbol{e}_z)$ to the local frame of reference $(\boldsymbol{e}_t, \boldsymbol{e}_c, \boldsymbol{e}_z)$ is given by the transition matrix $\boldsymbol{T}_m$ as

$$\boldsymbol{T}_m = \left[\boldsymbol{e}_t \begin{pmatrix} e_{t1} \\ e_{t2} \\ 0 \end{pmatrix} \middle| \boldsymbol{e}_c \begin{pmatrix} e_{c1} \\ e_{c2} \\ 0 \end{pmatrix} \middle| \boldsymbol{e}_z \begin{pmatrix} 0 \\ 0 \\ 1 \end{pmatrix} \right], \tag{F.6}$$

with the inverse matrix $\boldsymbol{T}_m^{-1}$, which is equal to its transpose $\boldsymbol{T}_m^T$ due to the symmetry of $\boldsymbol{E}$, mapping the local frame of reference $(\boldsymbol{e}_t, \boldsymbol{e}_c, \boldsymbol{e}_z)$ back to the Cartesian system $(\boldsymbol{e}_x, \boldsymbol{e}_y, \boldsymbol{e}_z)$.

F.1.3 Anisotropic Particle Stress($\sum^{p\prime}$) in the SBM

The $\sum^p_{nn}$ tensor of the SBM valid for simple shear flows only, is set up in a two-dimensional compression-tension coordinate system $(\boldsymbol{e}_t, \boldsymbol{e}_c, \boldsymbol{e}_z)$,and extended to a new anisotropic tensor $\sum^{p\prime}$ dependent on ($\hat{\rho_k}$) and valid for general flows. This extension pro-

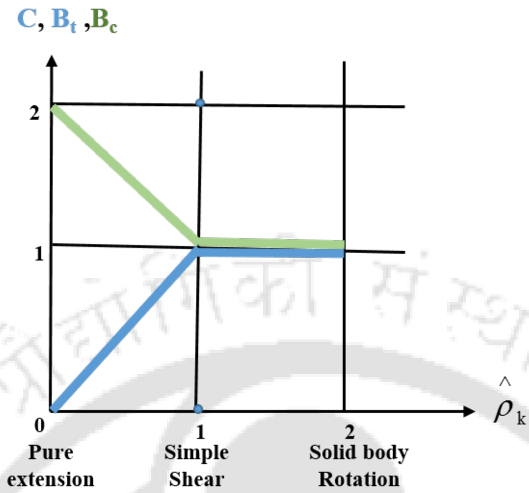

Figure F.1: Variation of C, B_t, and B_c with the kinematic ratio $\hat{\rho_k}$.

vides a frame of reference independent of the two-dimensional geometry of the flow, but strongly dependent on the local kinematic state of the suspension flow. The extension of $(\sum_{nn}^{p})$ to $(\sum^{p\prime})$ is done as follows:

$$\Sigma_{nn}^{p}(\boldsymbol{e}_x, \boldsymbol{e}_y, \boldsymbol{e}_z) = \begin{bmatrix} \Sigma_{11}^{p} & 0 & 0 \\ 0 & \Sigma_{22}^{p} & 0 \\ 0 & 0 & \Sigma_{33}^{p} \end{bmatrix} = \eta_0 \eta_N(\phi)\dot{\gamma} \begin{bmatrix} 1 & 0 & 0 \\ 0 & \lambda_2 & 0 \\ 0 & 0 & \lambda_3 \end{bmatrix} \tag{F.7}$$

$$\Sigma^{p}(\boldsymbol{e}_t, \boldsymbol{e}_c, \boldsymbol{e}_z) = \begin{bmatrix} \frac{\Sigma_{11}^{p}+\Sigma_{22}^{p}}{2} & \frac{N_1}{2} & 0 \\ \frac{N_1}{2} & \frac{\Sigma_{11}^{p}+\Sigma_{22}^{p}}{2} & 0 \\ 0 & 0 & \Sigma_{33}^{p} \end{bmatrix} \tag{F.8}$$

$$\Sigma^{p\prime}(\boldsymbol{e}_t, \boldsymbol{e}_c, \boldsymbol{e}_z) = \begin{bmatrix} \frac{\Sigma_{11}^{p}+\Sigma_{22}^{p}}{2}.B_t(\hat{\rho_k}) & \frac{N_1}{2}.C(\hat{\rho_k}) & 0 \\ \frac{N_1}{2}.C(\hat{\rho_k}) & \frac{\Sigma_{11}^{p}+\Sigma_{22}^{p}}{2}.B_t(\hat{\rho_k}) & 0 \\ 0 & 0 & \Sigma_{33}^{p} \end{bmatrix} \tag{F.9}$$

In Eq. (F.9), $B_t(\hat{\rho_k})$ and $B_c(\hat{\rho_k})$ are the functions that weight the particle normal stress in the tension and compression directions, respectively, with $(\sum_{33}^{p})$ being the stress component in the out-of-plane direction. Moreover, C($\hat{\rho_k}$) corresponds to the tangential stress weighting function. The values for $B_t(\hat{\rho_k})$, $B_c(\hat{\rho_k})$, and $C(\hat{\rho_k})$ adopted in this work are the ones suggested by Miller et al. (2009) and are summarized in Fig. F.1. The physical explanation behind the choice of the values for these weighting functions and their variation with $\hat{\rho_k}$ is as follows:

•**Simple shear flow:** In a simple shear flow situation, $\hat{\rho_k}$=1 and the values are set to $B_t = B_c = C = 1$ such that the tensor $\sum^{p\prime}$ after being transformed to the cartesian coordinate system goes back to be equal to $\sum_{nn}^{p}$.

•**Pure extension:** In this case B_t is set to zero since pure extension, the particles are far away from each other and the normal stress along the extensional axis is almost zero. Nonetheless C, which represents the tangential stress, should also be set to zero.

•**Rotation:** When $\hat{\rho_k}$>1, it is assumed that rotation plays no role and all weighting coefficients are set to 1 ($B_t = B_c = C = 1$).

•**Combination of shear and extension:** For $0 < \hat{\rho_k}$< 1, the weighing functions B_t, B_c, and C are linearly interpolated to account for the local kinematics between the compression and tension axes.

Finally, it should be noted that the tensor $\sum^{p\prime}$ is mapped back from the local coordinate system to the general Cartesian coordinate system using the transformation matrix T_m such that

$$\Sigma^{p\prime}(\boldsymbol{e}_x, \boldsymbol{e}_y, \boldsymbol{e}_z) =\leftarrow \boldsymbol{T}_m.\Sigma^{p\prime}(\boldsymbol{e}_t, \boldsymbol{e}_c, \boldsymbol{e}_z).\boldsymbol{T}_m^{-1} \tag{F.10}$$

List of Publications

International peer reviewed journals:

Published

1. **M.M. Reddy**, and A. Singh. (2019). Shear-induced particle migration and size segregation phenomenon in bidisperse suspension through symmetric T-shaped bifurcating channel. Phys. Fluids 31, pp 053305.
2. **M.M. Reddy**, P. Tiwari, and A. Singh. (2019). Effect of carrier fluid rheology on shear-induced particle migration in asymmetric T-shaped bifurcation channel. Int. J. Multiph. Flow, 111, pp 272–284.
3. **M.M. Reddy**, and A. Singh. (2014). Flow of concentrated suspension through oblique bifurcating channels. AIChE J. 60, pp 2692-2704.
4. M. Bhaskar, **M.M. Reddy**, and A. Singh. (2019). Particle migration of concentrated suspension flow in bifurcating channels. Adv. Powder Technol. 30, pp 1897-1909.
5. S. Yadav, **M.M. Reddy**, and A. Singh. (2016). Shear-induced migration of concentrated suspension through Y-shaped bifurcation channels. Int. Part. Sci. Technol., 34, pp 83–95.
6. S. Yadav, **M.M. Reddy**, and A. Singh. (2015). Shear-induced particle migration in three-dimensional bifurcation channel. Int. J. Multiph. Flow, 76, pp 1–12.

Under communication/preparation

1. **M.M. Reddy**, and A. Singh. (2019). Heat transfer enhancement and shear-induced particle migration in wavy micro-channels. (Under preparation)
2. M. Shadab, **M.M. Reddy**, and A. Singh. (2019). Role of secondary currents in radial and axial segregation of rotating suspensions. (Under preparation).

3. Md. Imaran, **M. M. Reddy**, and A. Singh (2019). Effect of inter-particle repulsive and frictional forces on the rheology of non-colloidal suspensions (Under preparation).

Conferences:

1. **M.M. Reddy**, P. Tiwari, and A. Singh. (2016). Shear-induced particle migration in suspension of particles in power-law fluids. IITG-KIT Joint Symposium, Kyoto Institute of Technology, Japan.

2. **M.M. Reddy**, P. Tiwari, and A. Singh. (2015). Numerical simulation of concentrated suspension flow in 3D asymmetric T-junction bifurcating channel. CHEMCON 2015, IIT Guwahati, India.

3. S. Yadav, **M.M. Reddy**, A. Kanaujiya, and A. Singh. (2015).Numerical simulation of dense suspension flow in symmetric T-shape 3D bifurcation channel. IUPAP, IIT Guwahati, India.

4. S. Yadav, **M.M. Reddy**, and A. Singh. (2014).Numerical simulation of particle migration in symmetric 3D bifurcation channel. CHEMCON 2015, Panjab University, India.

5. **M.M. Reddy**, and A. Singh. (2014). Numerical simulation of non-Newtonian suspension flow through asymmetric T-junction bifurcating channel. FMFP Conference, IIT Kanpur, India.

References

Aarts, P.A., van den Broek, S.A.J., Prins, G.J., Kuiken, G.D.C., Sixma, J.J., Heethaar, R.M., 1988. Blood platelets are concentrated near the wall and red blood cells, in the center in flowing blood. Arteriosclerosis 8 6, 819–24.

Abbott, J.R., Tetlow, N., Graham, A.L., Altobelli, S.A., Fukushima, E., Mondy, L.A., Stephens, T.S., 1991. Experimental observations of particle migration in concentrated suspensions: Couette flow. J. Rheol. 35, 773–795.

Ahmed, G.Y., Singh, A., 2011. Numerical simulation of particle migration in asymmetric bifurcation channel. J. Non-Newton Fluid. 166, 42 – 51.

Allende, M., Kalyon, D.M., 2000. Assessment of particle-migration effects in pressure-driven viscometric flows. J. of Rheol. 44, 79–90.

Altobelli, S.A., Givler, R.C., Fukushima, E., 1991. Velocity and concentration measurements of suspensions by nuclear magnetic resonance imaging. J. Rheol. 35, 721–734.

Anastasiou, A., Spyrogianni, A., Koskinas, K., Giannoglou, G., Paras, S., 2012. Experimental investigation of the flow of a blood analogue fluid in a replica of a bifurcated small artery. Med. Eng. Phys. 34, 211 – 218.

Ashcroft, N.W., Langreth, D.C., 1967. Structure of binary liquid mixtures. i. Phys. Rev. 156, 685–692.

Audet, D., Olbricht, W., 1987. The motion of model cells at capillary bifurcations. Microvasc. Res. 33, 377 – 396.

Averbakh, A., Shauly, A., Nir, A., Semiat, R., 1997. Slow viscous flows of highly concentrated suspensions–part i: Laser-doppler velocimetry in rectangular ducts. Int. J. Multiphas. Flow. 23, 409 – 424.

Balan, C.M., Balan, C., 2010. μpiv measurement and numerical computation of the velocity profiles in microchannels. U.P.B. Sci Bull, Series D 72, 121–128.

Ball, R.C., Richmond, P., 1980. Dynamics of colloidal dispersions. Phys. Chem. Liq. 9, 99–116.

Balogh, P., Bagchi, P., 2018. Analysis of red blood cell partitioning at bifurcations in simulated microvascular networks. Phys. Fluids. 30, 051902.

Barber, J.O., Alberding, J.P., Restrepo, J.M., Secomb, T.W., 2008. Simulated two-dimensional red blood cell motion, deformation, and partitioning in microvessel bifurcations. Ann. Biomed. Eng. 36, 1690–1698.

Batchelor, G.K., 1977. Effect of brownian-motion on bulk stress in a suspension of spherical-particles. J. Fluid Mech. 83, 97 – 117.

Batchelor, G.K., Green, J.T., 1972. The hydrodynamic interaction of two small freely-moving spheres in a linear flow field. J. Fluid Mech. 56, 375–400.

Boublík, T., 1975. Two-dimensional convex particle liquid. Mol. Phys. 29, 421–428.

Brady, J.F., Bossis, G., 1988. Stokesian dynamics. Annu. Rev. Fluid Mech. 20, 111–157.

Brady, J.F., Morris, J.F., 1997. Microstructure of strongly sheared suspensions and its impact on rheology and diffusion. J. Fluid Mech. 348, 103–139.

Chapman, B., 1990. Shear-induced Migration Phenomena in Concentrated Suspensions. University of Notre Dame.

Chen, S.B., 2013. Axisymmetric creeping motion of particles towards a circular orifice or disk. Phys. Fluids. 25, 043106.

Chhabra, R., Richardson, J., 1999. Non-Newtonian flow in the process industries: fundamentals and engineering applications. Butterworth-Heinemann, Oxford.

Chow, A.W., Iwayima, J.H., Sinton, S.W., Leighton, D.T., 1994a. Particle migration of non-brownian, concentrated suspensions in a truncated cone-and-plate. Society of Rheology Meeting, Sacramento, CA. .

Chow, A.W., Sinton, S.W., Iwamiya, J.H., Stephens, T.S., 1994b. Shear-induced particle migration in couette and parallel-plate viscometers: Nmr imaging and stress measurements. Phys. Fluids. 6, 2561–2576.

D'Avino, G.H., Martien, A., Maffettone, P.L., 2015. Separation of particles in non-newtonian fluids flowing in t-shaped microchannels. Adv. Mod. Simu. Eng. Sci. 2, 9.

Davis, R., Acrivos, A., 1985. Sedimentation of noncolloidal particles at low reynolds numbers. Ann. Rev. Fluid Mech. 17, 91–118.

Dbouk, T., Lemaire, E., Lobry, L., Moukalled, F., 2013. Shear-induced particle migration: Predictions from experimental evaluation of the particle stress tensor. J. Non-Newton. Fluid. 198, 78 – 95.

Ditchfield, W., Olbricht, W.L., 1996. Effects of particle concentration on the partitioning of suspensions at small divergent bifurcations. J. Biomech. Eng. 118, 287–294.

Eckstein, E.C., Bailey, D.G., Shapiro, A.H., 1977. Self-diffusion of particles in shear flow of a suspension. J. Fluid Mech. 79, 191–208.

Einstein, A., 1906. Investigation on the theory of Brownian movement. Dover publications.

Enden, G., Popel, A.S., 1994. A numerical study of plasma skimming in small vascular bifurcations. J. Biomech. Eng. 116, 79–88.

Faivre, M., Abkarian, M., Bickraj, K., A Stone, H., 2006. Geometrical focusing of cells in a microfluidic device: An approach to separate blood plasma. Biorheology 43, 147–59.

Fan, X.J., Phan-Thien, N., Zheng, R., 2000. Simulation of fibre suspension flow with shear-induced migration. J. Non-Newton Fluid. 90, 47 – 63.

Fang, Z., Mammoli, A.A., Brady, J.F., Ingber, M.S., Mondy, L.A., Graham, A.L., 2002. Flow-aligned tensor models for suspension flows. Int. J. Multiphas. Flow. 28, 137 – 166.

Fang, Z., Phan-Thien, N., 1999. A particle suspension model: an unstructured finite-volume implementation. J. Non-Newton Fluid. 80, 135 – 153.

Fridjonsson, E.O., Seymour, J.D., Cokelet, G.R., Codd, S.L., 2011. Dynamic nmr microscopy measurement of the dynamics and flow partitioning of colloidal particles in a bifurcation. Exp. Fluids. 50, 1335–1347.

Gadala-Maria, F., Acrivos, A., 1980. Shear-induced structure in a concentrated suspension of solid spheres. J. Rheol. 24, 799–814.

Gauthier, F., Goldsmith, H.L., Mason, S.G., 1971. Particle motions in non-newtonian media. ii. poiseuille flow. T. Soc. Rheol. 15, 297–330.

Gijsen, F., van de Vosse, F., Janssen, J., 1999. The influence of the non-newtonian properties of blood on the flow in large arteries: steady flow in a carotid bifurcation model. J. Biomec. 32, 601 – 608.

Hampton, R.E., Mammoli, A.A., Graham, A.L., Tetlow, N., Altobelli, S.A., 1997. Migration of particles undergoing pressure-driven flow in a circular conduit. J. Rheol. 41, 621–640.

Huang, P., Joseph, D., 2000. Effects of shear thinning on migration of neutrally buoyant particles in pressure driven flow of newtonian and viscoelastic fluids. J. Non-Newton Fluid. 90, 159 – 185.

Husband, D.M., Mondy, L.A., Ganani, E., Graham, A.L., 1994. Direct measurements of shear-induced particle migration in suspensions of bimodal spheres. Rheol. Acta 33, 185–192.

Ishikawa, T., Fujiwara, H., Matsuki, N., Yoshimoto, T., Imai, Y., Ueno, H., Yamaguchi, T., 2011. Asymmetry of blood flow and cancer cell adhesion in a microchannel with symmetric bifurcation and confluence. Biomed. Microdevices. 13, 159–167.

Jaggi, R.D., Sandoz, R., Effenhauser, C.S., 2007. Microfluidic depletion of red blood cells from whole blood in high-aspect-ratio microchannels. Microfluid. Nanofluid. 3, 47–53.

Kanaris, A., Anastasiou, A., Paras, S., 2012. Modeling the effect of blood viscosity on hemodynamic factors in a small bifurcated artery. Chem. Eng Sci. 71, 202 – 211.

Kanehl, P., Stark, H., 2015. Hydrodynamic segregation in a bidisperse colloidal suspension in microchannel flow: A theoretical study. J. Chem. Phys. 4, 214901–214914.

Karnis, A., Goldsmith, H., Mason, S., 1966. The kinetics of flowing dispersions: I. concentrated suspensions of rigid particles. J. Colloid Interf. Sci. 22, 531 – 553.

Karnis, A., Mason, S.G., 1966. Particle motions in sheared suspensions. xix. viscoelastic media. T. Soc. Rheol. 10, 571–592.

Kim, J.M., Lee, S.G., Kim, C., 2008. Numerical simulations of particle migration in suspension flows: Frame-invariant formulation of curvature-induced migration. J. Non-Newton Fluid. 150, 162 – 176.

Koh, C.J., Hookham, P., Leal, L.G., 1994. An experimental investigation of concentrated suspension flows in a rectangular channel. J. Fluid Mech. 266, 1–32.

Kowalewski, T., 1980. Velocity profiles of suspension flowing through a tube. Arch. Mech. 32, 857–865.

Krieger, I.M., Dougherty, T.J., 1959. A mechanism for non-newtonian flow in suspensions of rigid spheres. T. Soc. Rheol. 3, 137–152.

Krishnan, G.P., Beimfohr, S., Leighton, D.T., 1996. Shear-induced radial segregation in bidisperse suspensions. J. Fluid Mech. 321, 371 – 393.

Krogh, A., 1921. Studies on the physiology of capillaries. J. Physiol. 55, 412–422.

Kumar, A., Graham, M.D., 2012. Margination and segregation in confined flows of blood and other multicomponent suspensions. Soft Matter 8, 10536–10548.

Lagoela, M., Oliveira, B., Cidre, D., 2009. Computational vision and medical image processing: Vip-image. edited by J. M. R. S. Tavares .

Lam, Y., Chen, X., Tan, K., Chai, J., Yu, S., 2004. Numerical investigation of particle migration in poiseuille flow of composite system. Compos. Sci. Technol. 64, 1001 – 1010.

Lam, Y., Chen, X., Tan, K., Jan, M., Tam, K., Yu, M.C., 2002. Experimental measurements and simulation of particle migration in pressure-driven tube flow: Applications to flow in runners. J. Inj. Mol. Technol. 6, 45–57.

Leble, V., Lima, R., Dias, R., Fernandes, C., Ishikawa, T., Imai, Y., Yamaguchi, T., 2011. Asymmetry of red blood cell motions in a microchannel with diverging and converging bifurcation. Biomicrofluidics 5, 44120–4412015.

Leighton, D., Acrivos, A., 1986. Viscous resuspension. Chem. Eng. Sci. 41, 1377 – 1384.

Leighton, D., Acrivos, A., 1987a. Measurement of shear-induced self-diffusion in concentrated suspensions of spheres. J. Fluid Mech. 177, 109–131.

Leighton, D., Acrivos, A., 1987b. The shear-induced migration of particles in concentrated suspensions. J. Fluid Mech. 181, 415–439.

Leonard, E.F., West, A.C., Shapley, N.C., Larsen, M.U., 2004. Dialysis without membranes: How and why? Blood Purif. 22, 92–100.

Li, X., Popel, A.S., Karniadakis, G.E., 2012. Blood-plasma separation in y-shaped bifurcating microfluidic channels: a dissipative particle dynamics simulation study. Phys. Biol. 9, 026010.

Lyon, M.K., Leal, L.G., 1998a. An experimental study of the motion of concentrated suspensions in two-dimensional channel flow. part 1. monodisperse systems. J. Fluid Mech. 363, 25 – 56.

Lyon, M.K., Leal, L.G., 1998b. An experimental study of the motion of concentrated suspensions in two-dimensional channel flow. part 2. bidisperse systems. J. Fluid Mech. 363, 57 – 77.

Maron, S.H., Pierce, P.E., 1956. Application of ree-eyring generalized flow theory to suspensions of spherical particles. J. Colloid Sci. 11, 80 – 95.

Matos, H., Oliveira, P., 2013. Steady and unsteady non-newtonian inelastic flows in a planar t-junction. Int. J. Heat Fluid Fl. 39, 102 – 126.

Miller, R.M., Morris, J.F., 2006. Normal stress-driven migration and axial development in pressure-driven flow of concentrated suspensions. J. Non-Newton Fluid. 135, 149 – 165.

Miller, R.M., Singh, J.P., Morris, J.F., 2009. Suspension flow modeling for general geometries. Chem. Eng. Sci. 64, 4597 – 4610. Morton Denn Festschrift.

Morris, J., Katyal, B., 2002. Microstructure from simulated brownian suspension flows at large shear rate. Phys. Fluids 14, 1920–1937.

Morris, J.F., Boulay, F., 1999. Curvilinear flows of noncolloidal suspensions: The role of normal stresses. J. Rheol. 43, 1213–1237.

Nott, P.R., Brady, J.F., 1994. Pressure-driven flow of suspensions: simulation and theory. J. Fluid Mech. 275, 157–199.

Perkkiö, J.and Keskinen, R., 1983. Hematocrit reduction in bifurcations due to plasma skimming. B. Math. Biol. 45, 41–50.

Phan-Thien, N., 1995. Constitutive equation for concentrated suspensions in newtonian liquids. J. Rheol. 39, 679–695.

Phillips, R.J., Armstrong, R.C., Brown, R.A., Graham, A.L., Abbott, J.R., 1992. A constitutive equation for concentrated suspensions that accounts for shear-induced particle migration. Phys. Fluids A-Fluid. 4, 30–40.

Pries, A., Ley, K., Claassen, M., Gaehtgens, P., 1989. Red cell distribution at microvascular bifurcations. Microvasc. Res. 38, 81 – 101.

Probstein, R.F., Sengun, M.Z., Tseng, T.C., 1994. Bimodal model of concentrated suspension viscosity for distributed particle sizes. J. Rheol. 38, 811–829.

Rao, R.R., Mondy, L.A., Baer, T.A., Altobelli, S.A., Stephens, T.S., 2002. Nmr measurements and simulations of particle migration in non-newtonian fluids. Chem. Eng. Commun. 189, 1–22.

Reddy, M.M., Singh, A., 2014. Flow of concentrated suspension through oblique bifurcating channels. AIChE J. 60, 2692–2704.

Richardson, J., Zaki, W., 1997. Sedimentation and fluidisation: Part i. Chem. Eng. Res. Des. 75, S82 – S100.

Roberts, B.W., Olbricht, W.L., 2003. Flow-induced particulate separations. AIChE J. 49, 2842–2849.

Roberts, B.W., Olbricht, W.L., 2006. The distribution of freely suspended particles at microfluidic bifurcations. AIChE J. 52, 199–206.

Ryssel, E., Brunn, P., 1999. Comparison of a quasi-newtonian fluid with a viscoelastic fluid in planar contraction flow. J. Non-Newton. Fluid. 86, 309 – 335.

Schmid-Schcönbein, G., Skalak, R., Usami, S., Chien, S., 1980. Cell distribution in capillary networks. Microvasc. Res. 19, 18 – 44.

Semwogerere, D., Weeks, E.R., 2008. Shear-induced particle migration in binary colloidal suspensions. Phys. Fluids 20, 043306.

Shauly, A., Averbakh, A., Nir, A., Semiat, R., 1997. Slow viscous flows of highly concentrated suspensions-part ii: Particle migration, velocity and concentration profiles in rectangular ducts. Int. J. Multiphas. Flow. 23, 613 – 629.

Sierou, A., Brady, J.F., 2002. Rheology and microstructure in concentrated noncolloidal suspensions. J. Rheol. 46, 1031–1056.

Sinton, S.W., Chow, A.W., 1991. Nmr flow imaging of fluids and solid suspensions in poiseuille flow. J. Rheol. 35, 735–772.

Subia, S.R., Ingber, M.S., Mondy, L.A., Altobelli, S.A., Graham, A.L., 1998. Modelling of concentrated suspensions using a continuum constitutive equation. J. Fluid Mech. 373, 193–219.

Vollebregt, H.M., van der Sman, R.G.M., Boom, R.M., 2012. Model for particle migration in bidisperse suspensions by use of effective temperature. Faraday Discuss. 158, 89 – 103.

Wang, T., Xing, Z., 2010. Characterization of blood flow in capillaries by numerical simulation. J. Modern Phys. 1, 349 – 356.

Xi, C., Shapley, N.C., 2008. Flows of concentrated suspensions through an asymmetric bifurcation. J. Rheol. 52, 625–647.

Yadav, S., Reddy, M.M., Singh, A., 2015. Shear-induced particle migration in three-dimensional bifurcation channel. Int. J. Multiphas. Flow. 76, 1 – 12.

Yen, R.T., Fung, Y.C., 1978. Effect of velocity distribution on red cell distribution in capillary blood vessels. Am. J. Physiol. Heart Circ. Physiol. 235, H251–H257.

Zarraga, I.E., Hill, D.A., Leighton, D.T., 2000. The characterization of the total stress of concentrated suspensions of noncolloidal spheres in newtonian fluids. J. Rheol. 44, 185–220.

Zrehen, A., Ramachandran, A., 2013. Demonstration of secondary currents in the pressure-driven flow of a concentrated suspension through a square conduit. Phys. Rev. Lett. 110, 018306.